Microstructural and Lattice-Preferred Orientation Analyses of Ductile Shear Zones: Maggia Nappe, Switzerland

Senior Honors Thesis

William Barnhart
Jeffery Rahl, Advisor

Submitted May 2008

ABSTRACT

Microstructures of 24 samples and quartz lattice-preferred orientations (LPO) of 13 samples from the crystalline Maggia Nappe, Switzerland were measured in order to assess the deformation history, mechanisms, and conditions of ductile shear zones related to nappe formation. Microstructures suggest dislocation accommodated dynamic recrystallization as evidenced by grain size reduction and grain boundary area reduction (GBAR). However, weak LPOs suggest diffusion processes that destroyed previously developed LPOs. Large grain size (~100-300m) suggests a major component of diffusion creep-accommodated grain-boundary sliding (GBS) followed by grain size growth. Undulatory extinction in grains implies grain growth was not entirely post deformational. Assuming stain rates of 10-13s-1, the deformation history of the Maggia Nappe at P/T conditions of 450°-650° C and 3-10 kbar is constrained as 1) development of a lineated magmatic fabric, 2) development of ductile shear zones and strong LPO through dislocation creep, 3) onset of diffusion creep-accommodated GBS after sufficient grain size reduction, 4) destruction of LPOs, and 5) syn- and post- deformational grain growth.

TABLE OF CONTENTS

LIST OF FIGURES AND TABLES

INTRODUCTION

Microstructures and crystallographic fabrics are a useful tool in identifying deformation mechanisms and deformation conditions in polycrystalline rocks (e.g., Law 1990, Fliervoet et al. 1997, Hirth & Tullis 1992, Bestmann & Prior 2003, Wightman et al. 2006). Lattice-preferred orientations (LPO) for a mono- or poly-crystalline rock can be used to identify active slip systems and shear sense while the strength of a sample's LPO along with microstructure analysis can aid in identifying deformation mechanisms (Law 1990, Hirth & Tullis 1992). Strong LPOs are often observed in rocks deformed through dislocation creep-accommodated dynamic recrystallization of grains while the absence of an LPO in significantly deformed samples ($\gamma \geq 4$) may suggest diffusion creep mechanisms (Law 1990). Diffusion creep, a process in which crystal vacancies migrate through or along grain boundaries, is a highly grain size sensitive mechanism that may be initiated by grain size reduction during dislocation creep-accommodated dynamic recrystallization (Passchier & Trouw 2005). Diffusion creep and grain-boundary sliding (GBS) cause grain rotations unconstrained by crystallographic orientations, effectively weakening previously well-developed LPOs (Law 1990). GBS has been proposed as an accommodation mechanism for diffusion creep, allowing it to occur with larger grain sizes (>10 μm) and faster strain rates. During diffusion creep, GBS has been shown to destroy LPO fabrics; however, lack of LPO is not diagnostic of GBS because GBS accommodation during dislocation creep retains strong LPOs (Law 1990).

In a tectonic context, microstructures can provide important information about the deformation history and conditions of large-scale structures (e.g., Wightman et al. 2006). Because only the final stage of ductile deformation is recorded in crystallographic

fabrics, microstructural observations are necessary to further constrain the complete deformation history of a rock (e.g. Bestmann & Prior 2003). This paper investigates samples from non-coaxial shear zones of the Lower Penninic Maggia Nappe in the Central Swiss Alps. Microstructural observations from 24 samples and quartz LPO data, by means of electron backscatter diffraction (EBSD), from 13 samples representing cross-sections across various shear zones is presented with the purpose of defining the history of the active deformation mechanisms and deformation conditions during the four identified deformation phases in the Maggia Nappe.

BACKGROUND

Tectonic Setting

The European Alps are the result of late Cretaceous and Tertiary collision between the Adriatic microplate and the subducting European plate. The origins of Alpine rocks are attributed to three regions related to middle Mesozoic rifting of Pangea: the European margin, the Penninic zone, and African margin rocks (Figure 1) (e.g., Favre and Stampfli, 1992, Manatschal & Bernoulli, 1998). European margin rocks constitute the pro-wedge and include the Jura Mountains, the Molasse, and the Helvetic and Ultrahelvetic realms (Figure 2). The Jura Mountains are the most outboard, NE extent of the accretionary prism and represent an allochthonous thin-skin thrust sheet with Triassic evaporate decollment (Stamplfi et al. 2002). The Molasse represent an Oligocene-filled foreland basin formed during late-Cretaceous to Oligocene uplift (Stampfli et al. 2002). The Helvetic and Ultrahelvetic realms represent the southern shelf and distal portion of the European continent along the Alpine Tethys Ocean and include

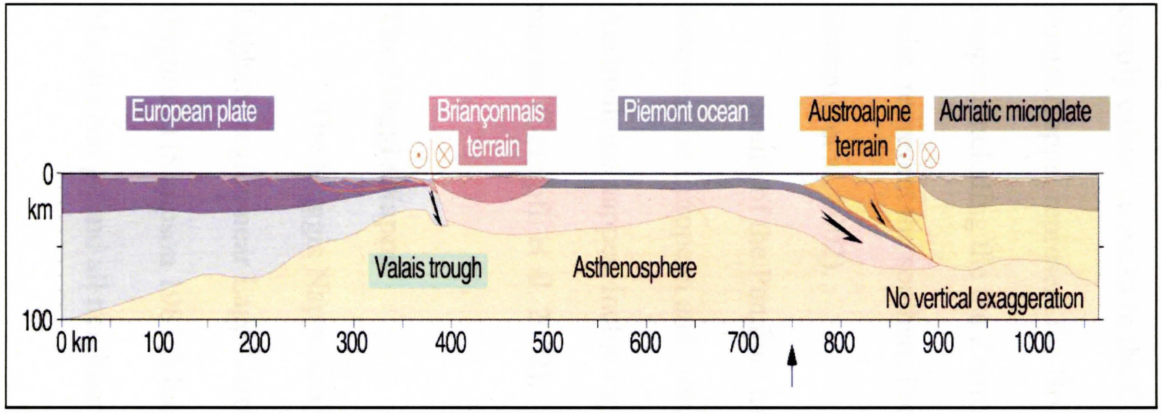

Figure 1: Late Cretaceous cross section of the Alpine Tethys Ocean demonstrating principle domains of Alpine rocks. Modified from Stampfli et al. 2002.

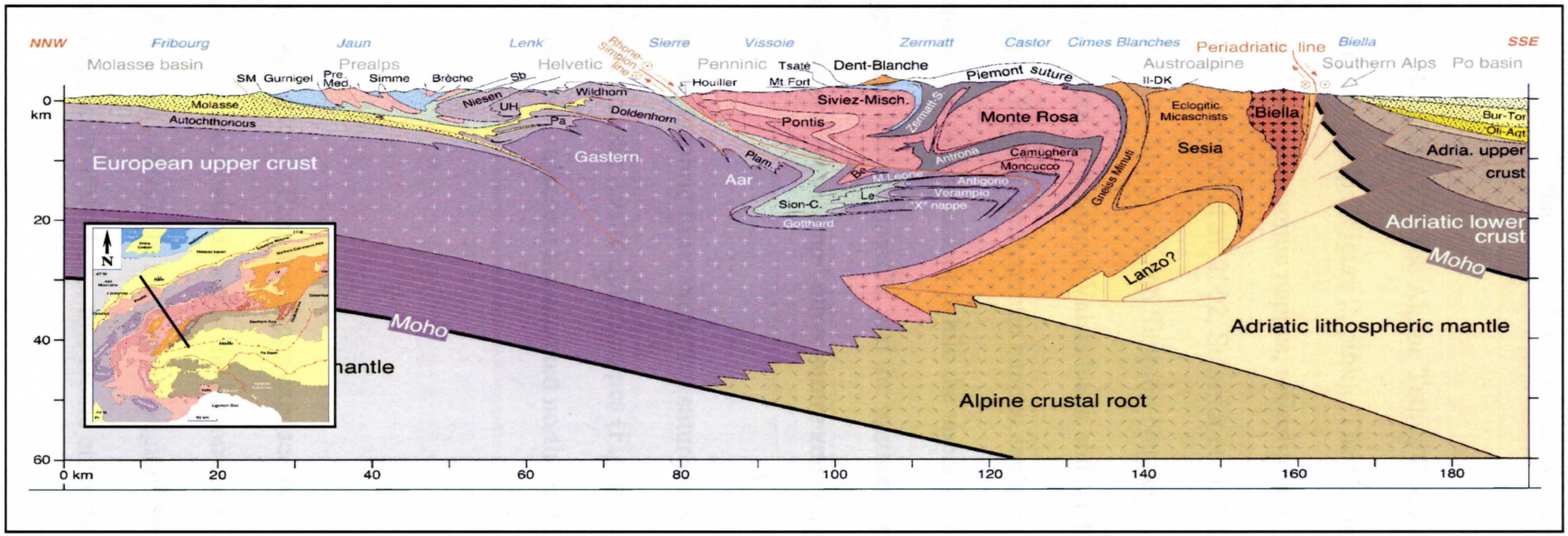

Figure 2: Present day cross section of the Alps. Modified from Stampfli et al. 2002.

the Morcles and Diablerets Nappes and the Aar, Gothard, and Mont Blanc massifs (Stampfli et al. 2002).

Penninic Zone rocks represent the substratum of the Alpine Tethys Ocean and are found in the retro-wedge exposed in the Central Alps (Figure 2, pink). The Penninic Zone is divided into the upper, middle, and lower Penninic nappes, reflecting the different regions of the Alpine Tethys (e.g. Stampfli et al. 2002, Schmidt et al. 2004). Lower Penninic nappes, including the Maggia, Antigorio, and Simplon Nappes (Stampfli et al. 2002, Galli et al. 2007), are derived from the northern Valais basin and are the most deeply exhumed rocks in the Central Alps. The middle Penninic nappes, including the Pontis Nappe, represent the Brianconnais carbonate platform while the upper Penninic nappes, including the the Zermatt Nappe, the internal massifs, and the southern ophiolite belts, represent the southern Piemont basin and the Alpine Tethys suture zone (e.g. Stampfli et al. 2002).

South of the Penninic nappes lies the Insubric Line, the active suture zone between the European and Adriatic plates, and the Austroalpine nappes (Figure 2). The Austroalpine nappes, including the Sesia Zone, represent the accreted northern African margin (Stampfli et al. 2002).

The Maggia Nappe

The Maggia Nappe is a south verging lower Penninic nappe exposed best in the Laghetti region near Lago Naret, north of Ticino, Switzerland in the Lepontine Dome (Figure 3) (Simpson 1983; Mohanty & Ramsay 1994). In the Laghetti region, the Maggia Nappe and all neighboring tectonic units of the Lepontine Dome enter the

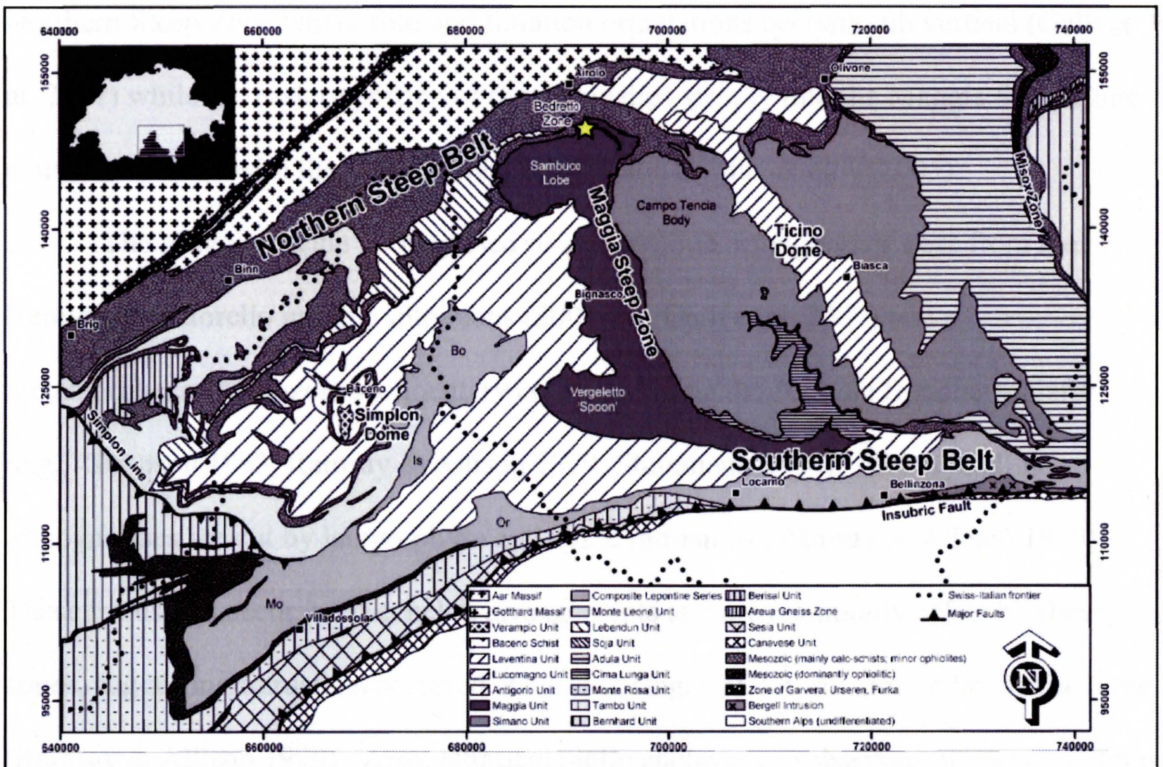

Figure 3: Structural Map of Central Alps. Field location marked by yellow star. Modified from Maxelon & Macnktelow (2005). Map coordinates are SwissGrid (meters).

Northern Steep Zone where fold and foliation orientations become sub vertical (Galli et al. 2007) while the eastern portion of the nappe dips steeply into the Maggia Steep Zone along the contact with the Simano Nappe (Maxelon & Mancktelow 2005).

The Maggia Nappe is composed of a crystalline orthogneissic core from the Hercynian Matorello granitic intrusions (300 Ma) (Galli et al. 2007) and a metamorphosed Mesozoic sedimentary cover including the Jurassic Bundnerschiefer (e.g., Simpson 1983, Ramsay & Allison 1979, Steinmann 1994). The crystalline orthogneisses are cut by lamprophyre and aplite intrusions (Ramsay & Allison 1979). These intrusions occur in en-echelon arrangements and are commonly offset by shear zones, suggesting intrusions occurred at varying stages of deformation in brittle fractures (Ramsay & Allison 1979). Also, elliptical mafic enclaves are observed in many locations near Lake Naret and demonstrate varying degrees of deformation.

Previous research indicates four separate deformation phases recorded in the Maggia Nappe (Galli et al. 2007, Mancktelow 1996, Ramsay & Allison 1979, Simpson 1983) near the Laghetti region. D1 phase deformation is characterized by the initial formation and stacking of crystalline cored isoclinal nappes and the formation of a penetrative foliation and ductile shear zones of Alpine age with peak temperatures $\leq 570^{\circ}$ (Galli et al. 2007, Simpson 1982). The D2 phase involved the refolding of the D1 nappe stack and foliation at 610°-640°C (Grujic & Mancktelow 1996, Maxelon & Mancktelow 2005, Galli et al. 2007). D2 also developed a strong lineation of quartz and biotite minerals that is generally sub parallel to fold axes formed by the D2 phase and plunges to the NNE (Galli et al. 2007). The D3 phase (550°-610° C) is marked by the formation of open, upright folds oblique to the overall trend of the Alps and the formation of a

crenulation cleavage accompanied by biotite growth in the hinges of these folds (Galli et al. 2007). The D4 ($\geq$550°C) phase forms disharmonic folds similar to D3, but at oblique orientations (Galli et al. 2007). This deformation phase is also responsible for the creation of the Northern Steep Zone (Milnes 1974).

Field Area

The field area has been extensively described and mapped (Figure 4) by Ramsay and Allison (1979), while Simpson has conducted quartz C-axis work on two samples (1980) and described microstructures and mineralogy across shear zone boundaries (1983). The outcrop is approximately 70x40 meters and is composed of mostly plagioclase-rich Matorello leucocratic granite bound by quartz-diorite country rock (Ramsay & Allison 1979, Simpson 1980, Galli et al. 2007). Throughout the granite, oblate, biotite-chlorite rich mafic enclaves (Figure 5a, b) are present along with a series of aplite and lampophyre dikes (Figure 5c, d). Cross-cutting relationships suggest the order of intrusion to be: diorite, granite, lampophyre dikes, aplite dikes, and pegmatite dikes (Gallie et al. 2007). Ramsay & Allison (1979) and Galli and others (2007) suggest the mafic enclaves (referred to as mafic xenoliths by Ramsay and Allison), are part of the Matorello primary intrusion during late Hercynian uplift and are related to intrusion of lampophyric dikes, as evidenced by swarming of mafic enclaves near lampophyre dikes. The shapes of undeformed enclaves are a result of magmatic intermingling between mafic lampophyre and the cooler felsic granite (Galli et al. 2007). Sharp boundaries between all intrusions suggest they are primary intrusions while each intrusion

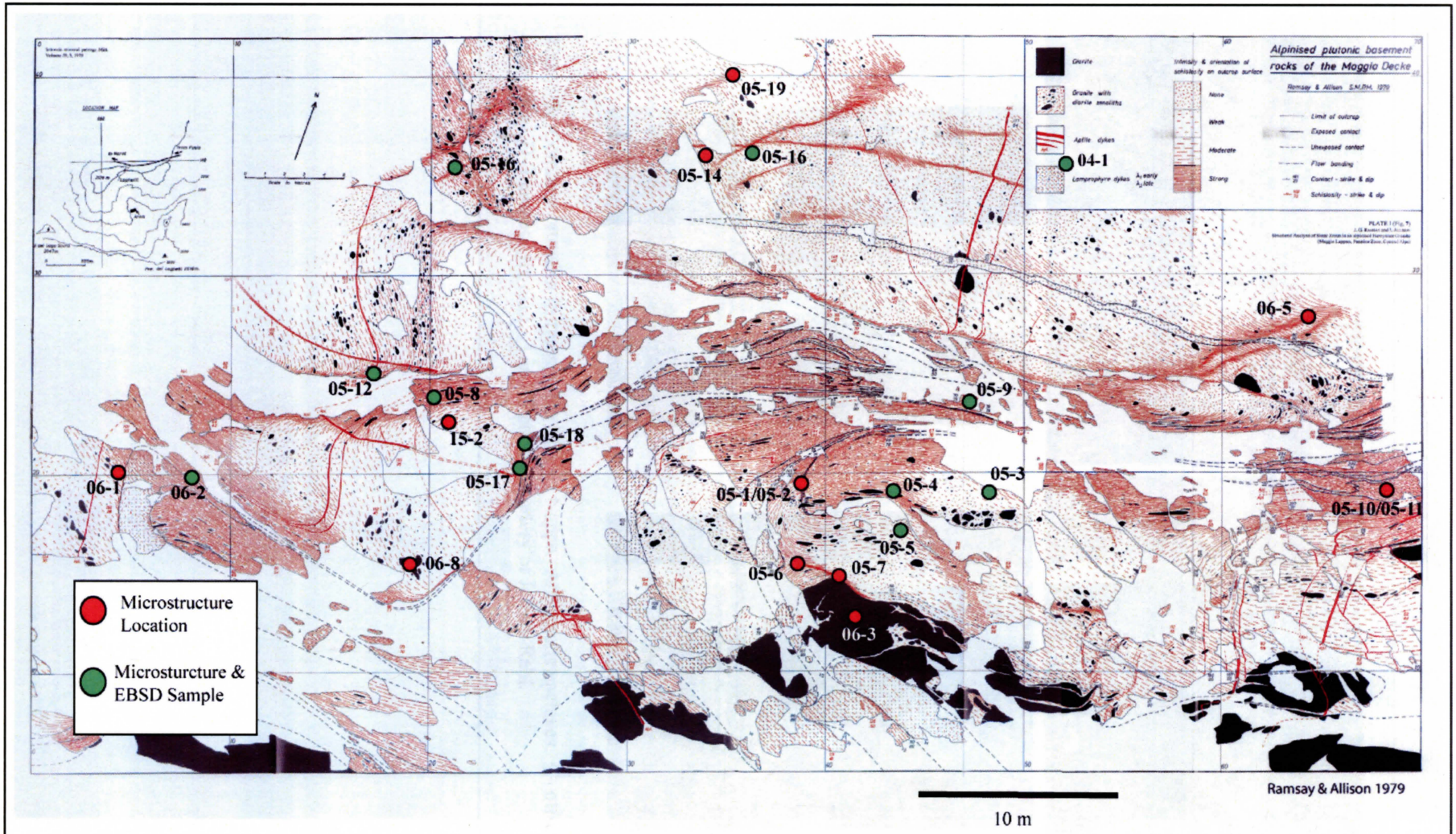

Figure 4: Maggia Nappe field area. Sample 15-1 located south of map extent. 0708 prefix removed from all locations. Modified from Ramsay & Allison (1979). Red points are sample locations, green points are sample and EBSD locations.

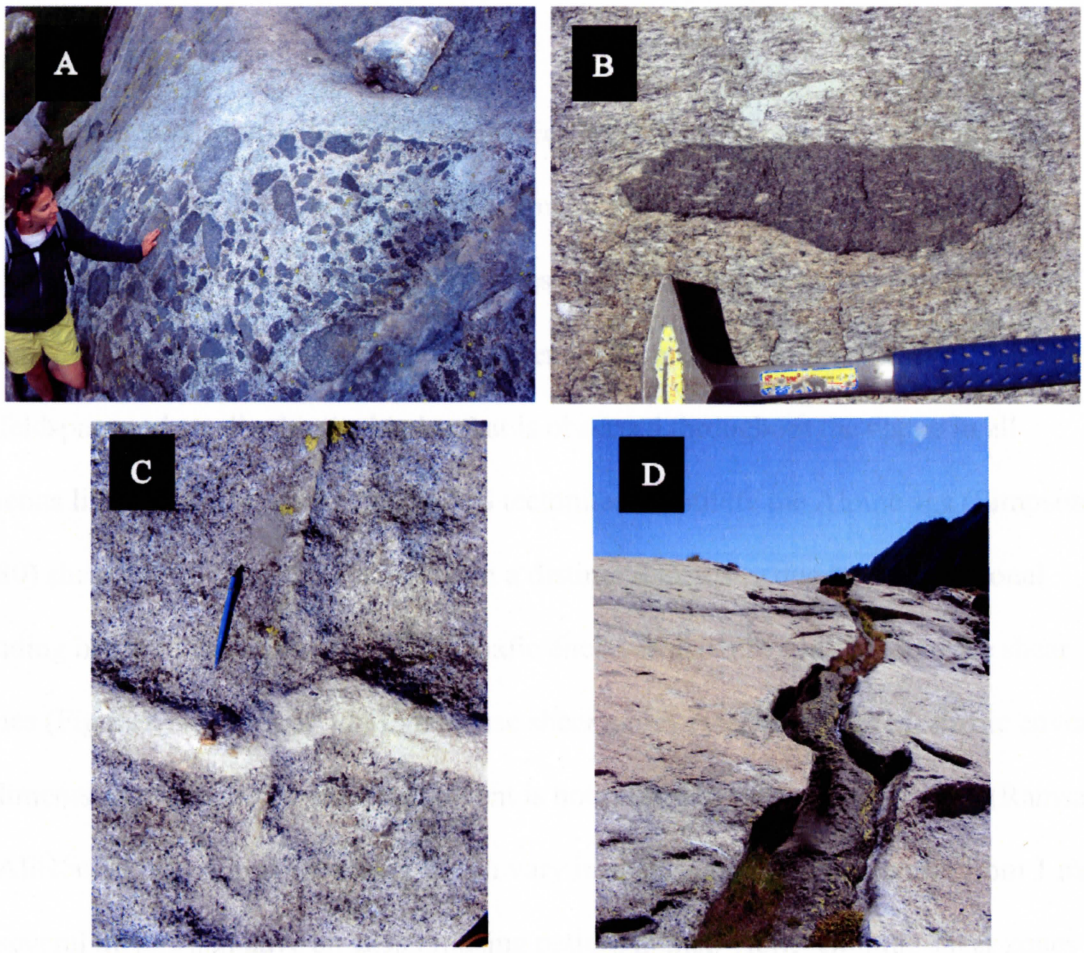

Figure 5: Common intrusive features of the Maggia Nappe. A/B- mafic enclaves. C- offset aplite dike. D- Lampophyre dike. A and B photos courtesy of Jeffrey Rahl.

demonstrates mineralogical homogeneity across the nappe regardless of deformation (Ramsay & Allison 1979, Galli et al. 2007).

Shear zones are an obvious deformation feature in the outcrop and divide the granite into two deformation fabrics: L tectonites and L-S tectonites. L tectonites are commonly referred to as undeformed granites and constitute the bounding wall rock of shear zones. They are identified by the presence of a subtle, pervasive mineral lineation of feldspars and smaller biotite blades that is observed throughout the nappe in all igneous lithologies (Simpson 1983). L-S tectonites constitute the Alpine age (Simpson 1980) shear zones. The shear zones form a distinct schistosity due to compositional banding between the felsic granite and mafic enclaves that are "pulled" into the shear zones (Figure 6) (Simpson 1983). Because shear zones extend into the Mesozoic cover sediments, it is assumed their development is not related to magmatic intrusion (Ramsay & Allison 1979). The shear zones, which vary in shear sense, range in width from 1 mm to several meters and have an anastomosing pattern in map view. Oblique shear zones with the same shear sense converge and diverge, forming a "lozenge" shape pattern (Ramsay & Allison 1979, Simpson 1983). Shear sense indicators are pervasive where dikes are offset and enclaves are pulled into long, tear shapes as they enter shear zones.

Lattice-Preferred Orientation and Deformation Mechanisms

Lattice-preferred Orientation (LPO) is the preferential alignment of crystallographic axes of constituent crystals dependent on critical resolved shear stress and active slip systems (Passchier & Trouw 2005). LPOs are easily identified in platy minerals such as micas that also demonstrate a strong shape preferred orientation (SPO)

Figure 6: Common mafic enclaves in the Laghetti region deformed at shear zone boundaries into long ribbons. Photos courtesy of Jeffrey Rahl.

that often constitutes a foliation. In minerals such as quartz or feldspars, other methods must be used to identify their LPO. LPO patterns are formed by rotation of crystals and internal deformation of crystalline lattices and are controlled by specific conditions outlined by Schmid (1994):

1. Active slip systems
2. Coaxiality of strain
3. Finite strain
4. Dynamic recrystallization processes (explained below)
5. In-situ grain growth

LPO data is presented on stereonets where pole diagrams are used to represent the orientations of a single crystallographic axis. Traditionally, the X-axis (S_1, E-W axis) represents the principle shortening direction, the Z-axis (S_3, N-S axis) represents the principle elongation direction, and the Y-axis (S_2)is vertical and orthogonal to X and Z. Preferred groupings of pole orientations form shapes in stereonets when an LPO is present. Girdles may form in opposing hemispheres and are connected through the center to create Type I or Type II crossed girdles. Type I girdles represent plane strain while Type II girdles represent constrictional strain (Figure 7) (Passchier & Trouw 2005). Cleft girdles, which appear as small circles, form on the edges of the stereonet and represent flattening strain (Figure 7) (Passchier & Trouw 2005).

During deformation of all scales, multiple processes act at the grain and atomic scale to produce permanent spatial and volume changes. In order to permanently deform a crystal, the positions of atoms in the crystal lattice must be rearranged by the movement of defects by means of specific deformation mechanisms described below. The

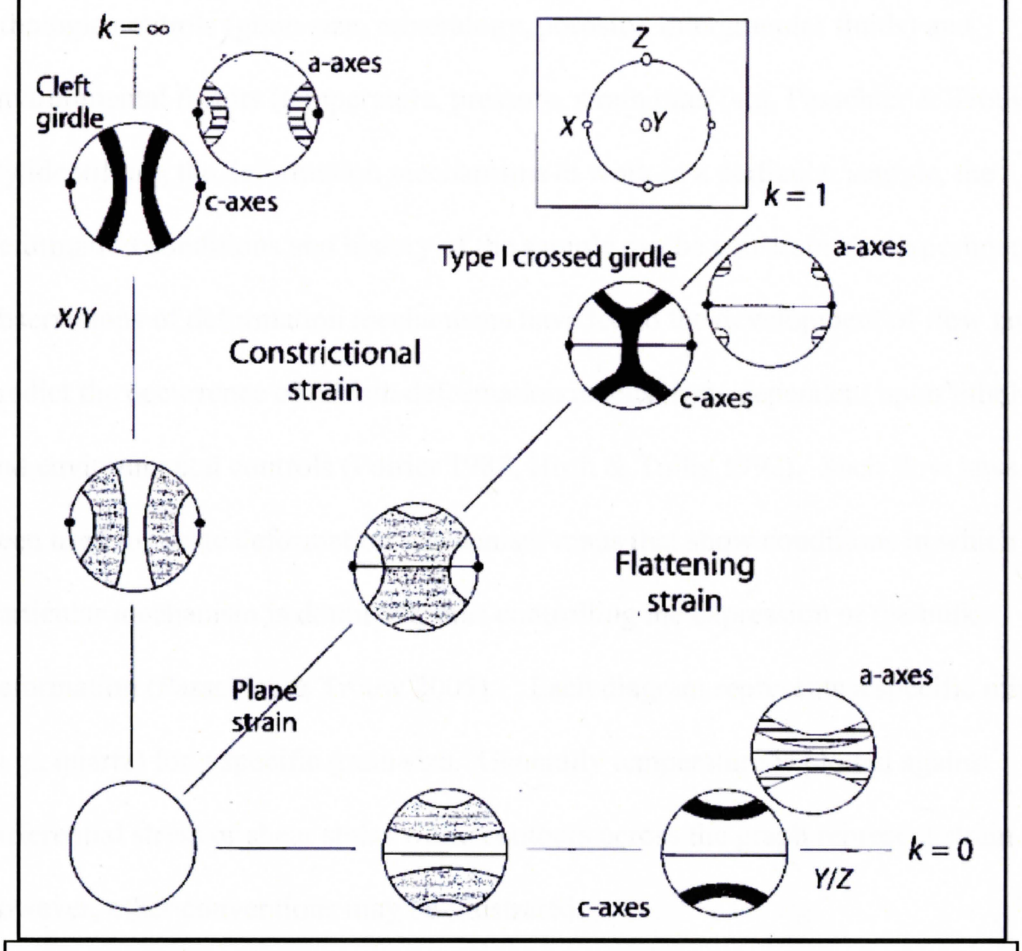

Figure 7: Flynn Plot demonstrating common LPO patterns related to different strain characteristics. Modified from Passchiear and Trouw 2005.

dominance and speed of these processes are dependent on a number of factors, including lithologic controls (grain size, mineralogy, porosity, intergranular fluids) and environmental factors (temperature, pressure, strain rate) (e.g. Passchier & Trouw 2005). By identifying the deformation mechanisms at work in a particular sample, the deformation conditions and history of the sample can be constrained. Experimental observations of deformation mechanisms have led to the development of flow laws to predict the occurrence of certain deformation mechanisms dependent upon lithological and environmental controls (Poirier 1985, Hirth & Tullis 1992). Such flow laws have been used to create deformation mechanism maps that show conditions in which a particular mechanism is dominant, thus controlling the expression of the bulk deformation (Passchier & Trouw 2005). Each diagram represents a specific mineralogy (e.g., quartz) for a specific grain size. Generally temperature is plotted against differential stress or shear stress while contours across the graph represent strain rates; however, other conventions may be illustrated.

Plastic deformation of crystals and grains is accommodated by defects in the crystalline structure. Point defects are vacancies, impurities, or interstitial atoms in a lattice that create points of strength inconsistency which migrate through the crystal when a differential stress is imposed, causing internal deformation of the crystal. Vacancies allow deformation to occur easily while impurities and interstitial atoms act to obstruct deformation by making the crystal harder.

In addition to point defects, line and planar defects occur. Linear defects, or dislocations, obstruct the movement of lattice planes (Davis & Reynolds 1996). Dislocations form at the end of an extra "half plane" in a crystal lattice, called an edge

dislocation. In some cases, the dislocation may be displaced over two lattice planes, causing a rotation and forming a screw dislocation (Passchier & Trouw 2005). Planar defects are similar to dislocations except that they constitute an entire plane instead of a plane edge.

Below, four principal deformation mechanisms present in quartz aggregates are described.

Pressure Solution

Also known as dissolution creep, pressure solution deformation requires pore fluids. Material from one grain is selectively removed from sites of high stress, transported through a fluid medium, then reprecipitated along another grain boundary. Pressure solution is most effective where grains meet at high angles, creating a point where high compressive forces can easily dissolve grain boundaries. Dissolved material then moves through enriched pore fluids and reprecipitates along grain boundaries in regions of low compressive stress. In microstructures, pressure solution is best identified by the presence of strain shadows and overgrowths. Fibers of reprecipitated material form fibers in veins or strain shadows that grow orthogonal to σ_1 (Davis & Reynolds 1996). Pressure solution occurs at a wide range of temperatures but at low differential stress, preventing experimental observations and the development of a flow law.

Diffusion Creep

Diffusion creep processes occur at high temperatures relative to material melting point and are characterized by deformation by the migration of lattice vacancies from

regions of low stress to high stress (Rutter 1983). Diffusion creep is divided into two mechanisms: Volume-diffusion creep and grain-boundary diffusion creep. Volume-diffusion creep, more commonly known as Nabarro-Herring creep, occurs when a differential stress forces vacancies to diffuse toward lattice surfaces and atomic planes under high compressive stress (Twiss & Moores 1992). Here, the vacancies are destroyed while atoms migrate at an equal rate in the opposite direction to fill the voids left by the vacancies (Twiss & Moores 1992). The net movement of atoms from surfaces of high compressive stress to surfaces of low compressive stress results in the deformation of the crystal lattice. Nabarro-Herring creep occurs at very low differential stress and temperatures close to the grain's melting temperature when flow of atoms is easiest (Davis & Reynolds 1996). The flow law for Nabarro-Herring creep is:

$$\dot{\varepsilon} = A_{NH}\mu VD_L / RTd^2 \cdot (\sigma / \mu) \cdot e^{(-H_L / RT)} \text{ (Table 1)}$$

Grain-boundary diffusion creep, or Cobble creep, is characterized by the diffusion of vacancies along grain boundaries from surfaces of low compressive stress to high compressive stress (Davis & Reynolds 1996). For example, when two grains are compressed, material at the interface between the two grains will migrate and redistrbute itself on the edges of the grains where the boundaries do not touch or are experiencing the lowest stress. Like Nabarro-Herring creep, atoms move at an equal rate in the opposite direction of the vacancies towards lower compressive stress. Because Cobble creep occurs at grain boundaries, transportation of material is much faster than in Nabarro-Herring creep, allowing Cobble creep to occur at lower temperatures and at quicker rates. The flow law for Cobble creep is:

$$\dot{\varepsilon} = A_C\mu VD_G W / RTd^3 \cdot (\sigma / \mu) \cdot e^{(-H_G / RT)} \text{ (Table 1)}$$

Table 1: Flow law variables

Symbol	Explanation
e	exponential
$\dot{\varepsilon}$	shear strain rate
σ	shear stress
T	temperature
b	Burgers vector
Ac	Cobble creep numerical factor
Anh	Nabarro-Herring creep numerical factor
H	molar activation enthalpy
D	diffusion constant
R	gas constant
k	Boltzmann constant
μ	shear modulus
d	grain size
W	grain boundary thickness
V	molar volume
σ/μ	normalised shear stress

Rutter and others (1994) have demonstrated during laboratory deformation of calcite grains that during conditions where grain size sensitive deformation mechanisms, such as diffusion creep, are dominant, poor LPO fabrics develop. This is attributed to crystallographically unconstrained rotation (Etheridge & Wilkie 1979). Fliervoet and others (1999) demonstrated similar findings with olivine in which highly strained rocks under conditions conducive to diffusion creep developed very poor LPOs attributed to increased grain boundary sliding.

Grain-Boundary Sliding

Grain-boundary sliding (GBS) is a process in which grains slide past each other along common boundaries or zones (Langdon & Vastava 1982). GBS occurs coincidentally with diffusion processes to prevent large gaps in the crystal lattice from opening. GBS also determines the strain rate of most deformation due to its rapid rate of activity (Langdon 1995). GBS favors diffusion creep because of the small grain sizes involved (Passchier & Trouw 2005). Diffusion paths are short and the formation of equal sized, round to polygonal grains act as low energy pathways for slip. Similar to diffusion creep, GBS acts to destroy crystallographic fabrics due to grain rotations unconstrained by crystallographic axes.

Dislocation Creep

Dislocation creep is described by the following flow law:

$$\dot{\varepsilon} = \mu b D_L / kT \cdot (\sigma / \mu)^3 \cdot e^{(-H_L / RT)}$$ (Table 1)

During dislocation creep, an edge dislocation causes a small portion of a crystalline slip plane to activate. Differential stress induces shearing of the crystal lattice where the dislocation occurs, causing a short amount of slip along the active slip plane. Migration of the dislocation across the slip plane allows the crystal to systematically slip and deform without forcing all bonds within the slip plane to break at once (Passchier & Trouw 2005). Dislocation creep is coincidental with the process of dynamic recrystallization: recrystallization of rocks during progressive deformation. Dynamic recrystallization is an important component of many deformation mechanisms because the process effectively reduces energy differences between grains caused by varying concentrations of dislocations (Hirth & Tullis 1992). Bulging, subgrain rotation, and grain boundary migration are three recrystallisation processes active during dislocation creep and dependent on temperature and differential stress. Hirth and Tullis (1992) divide dislocation creep recrystallisation processes into three distinct regimes derived in laboratory deformations consistent with field observations.

Bulging Recrystallization (BLG)

BLG occurs at low temperatures and results in the "bulging" of one grain boundary into another grain boundary where there is a high concentration of dislocations and corresponds to Regime 1 of Hirth and Tullis (1992). BLG operates at the lowest temperatures in which dislocation creep can occur (Hirth & Tullis 1992). Bulges may become a new grain through the formation of subgrains or though migration of grain boundaries (Stipp et al. 2002). Microstructurally, core-and-mantle structures may form in which an old grain is surrounded by a halo of smaller recrystallized grains (Gifkins

1976). The core grains may also exhibit irregular patchy extinction and heterogenous flattening (Hirth & Tullis 1992).

Subgrain Rotation Recrystallisation (SGR)

SGR corresponds to Regime 2 of Hirth and Tullis (1992) and is initiated by the continuous addition of dislocations to subgrain boundaries (Passchier & Trouw 2005). Progressive accumulation of dislocations causes the lattices of subgrains to rotate and misorient until they can no longer be considered the same grain. Newly formed grains are slightly elongated while core-and-mantle structures of BLG deform into alternating sheets of old grains and new grains/ subgrains.

Grain Boundary Migration (GBM)

GBM corresponds to Regime 3 of Hirth and Tullis (1992) and occurs at high temperatures when grain boundaries can remove all dislocations by sweeping through a crystal lattice. Subgrains continue to form but they are highly mobile, forming lobate grain boundaries (Passchier & Trouw 2005). Deformed grains generally show little evidence of strain, such as undulose extinction, and are larger than surrounding subgrains (Passchier & Trouw 2005). The lack of strain indicators distinguishes GBM from core grains formed during BLG (Passchier & Trouw 2005).

The microstructures most indicative of dislocation creep-accommodated dynamic recrystallization include rounded, lobate, equigranular grains and grain aggregates, bulging grain boundaries, and a progressive sense of grain boundary area reduction (GBAR). Likewise, strong LPOs develop when shear strain values exceed 4-5 during

dislocation creep, as observed in both the laboratory and field (Knipe 1989, Fliervoet et al. 1999). Recovery microstructures are also strong indications of dislocation creep. As a rock is strained and deformed through dislocation creep, sweeping undulose extinction develops as dislocations begin to migrate. As they become concentrated, deformation bands form followed by subgrain boundaries during dynamic recrystallization.

Quartz

Quartz is the second most abundant mineral in the crust, yet its deformation behavior is not fully understood because of the role water plays while enclosed in the crystal lattice (Passchier & Trouw 2005). Quartz is a rhombohedral silicate composed of a hexagonal prism terminated by six-sided rhombs on either end of the prism. Four axes define crystal orientations: the c-axis and three a-axes (Figure 8). The c-axis is oriented longitudinally through the center of the hexagonal prism such that it emerges through the vertices of the two rhombs. The a-axes are oriented orthogonal to the c-axes and separated by 120°.

Depending on temperature, quartz will deform via four slip systems: basal slip, rhomb slip, prism slip, and c-slip, forming different LPO patterns (Figure 9). At temperatures less than 300°C, brittle failure and pressure solution dominate deformation (Dunlap et al. 1997). Microstructurally, fractured grains, undulose extinction, and pressure solution recrystallization are present (Nishikawa & Takeshita 1999). Between 300° and 400°C, basal slips occurs as the quartz grains glides parallel to the plain of the a-axes. Slip is accommodated by dislocation creep and glide, resulting in patchy extinction, deformation lamellae, and BLG recrystallization (Stipp et al. 2002). In pole

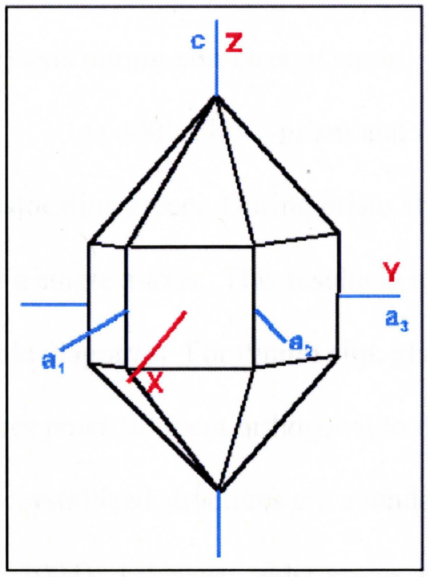

Figure 8: Quartz axes orientations. Modified from Passchier & Trouw (2005).

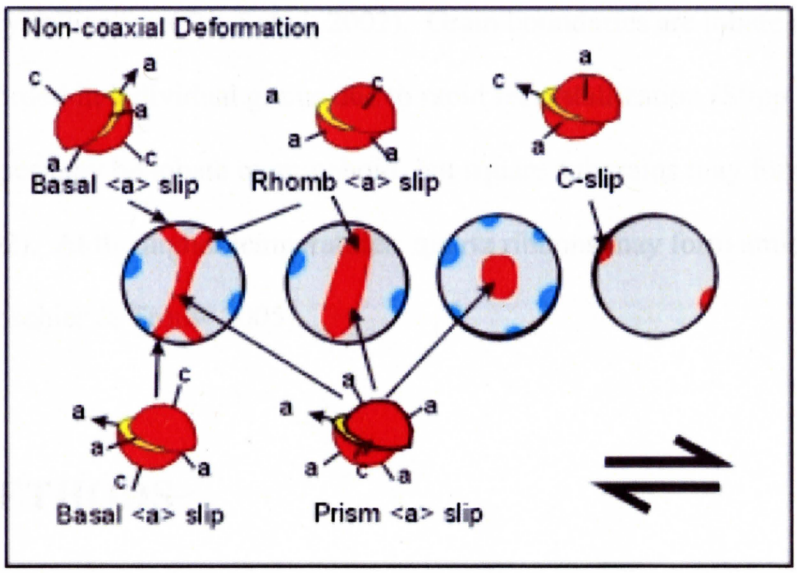

Figure 9: Stereonet patterns for quartz slip systems in non-coaxial strain. Modified from Passchier & Trouw (2005).

diagrams, the c-axes form a Type 1 crossed girdle oriented subparallel to the shortening (z) axis during non-coaxial strain.

At 400°-500°C, prism and rhomb slip are dominant and accommodated by dislocation creep. During prism slip, gliding occurs at the base of rhombs in the direction of a single a-axis. This results in alignment of c-axes along the Y-axis at the center of pole diagrams. For rhomb slip, glide occurs on the faces of the end rhombs, causing c-axes poles to orient orthogonal to the extension (x) direction. At these temperatures, recrystallized structures are abundant due to dominance of SGR recrystallization (Stipp et al. 2002). Likewise, older grains are highly flattened (Passchier & Trouw 2005).

At 500°-700°C, prism slip is dominant, progressing into c-slip. During c-slip, gliding occurs parallel to the c-axis, forming cleft girdles that migrate towards the extension (x) axis. Dislocation creep is still dominant and accommodated by GBM recrystallization (Stipp et al. 2002). Grain boundaries are lobate and little strain is recorded in individual grains due to rapid recrystallization (Stipp et al. 2002). Grain shapes may be lobate or amoeboid, but square subgrains may form as well (Stipp et al. 2002). At the higher temperatures, quartz ribbons may form amidst finer grains (Passchier & Trouw 2005).

METHODS

Field

26 oriented samples were collected from the Ramsay and Allison (1979) research area in the Lago del Naret region. 24 samples were collected from undeformed and deformed granites and 2 were collected from granodiorite country rock (Table 2).

Table 2: Field Sample Information

ID	Slide ID	Field Orientation	Composition	Deformation
070804-1*	1, 2	111/18 S	Granite	Undeformed
070805-1	3, 4	039/ 23 E	Granite	Moderate
070805-2	5, 6	025/ 43 E	Lampophyre	Moderate
070805-3*	7, 8	090/ 20 E	Granite	Moderate
070805-4*	9, 10	084/ 36 S	Granite	Moderate
070805-5*	11, 12	073/54S	Granite	Moderate
070805-6	13, 14	117/ 18 S	Granite	Moderate
070805-7	15, 16	245/ 19 NW	Granite	Well
070805-8*	17, 18	234/ 63 NW	Granite	Well
070805-9*	19, 20	245/ 10 N	Granite	Well
070805-10	21, 22, 23, 24	046/ 17S	Granite/ Enclave	Well
070805-11	25, 26	001/ 34 E	Enclave	Well
070805-12*	27, 28, 29,30	122/ 35 S	Granite/ Aplite	Moderate
070805-13**	-	-	-	-
070805-14*	31, 32	168/ 16 W	Granite	Undeformed
070805-15*	33, 34	101/ 11 SW	Granite	Undeformed
070805-16*	35, 36	025/ 41 E	Granite	Moderate
070805-17*	37, 38	111/ 28 S	Granite	Moderate
070805-18	-	008/ 69 E	Granite	Moderate
070805-19	39, 40	035/ 47 E	Granite	Moderate
070806-1	41, 42	142/ 20 W	Granite	Moderate
070806-2*	43, 44	151/ 22 W	Granite	Well
070806-3	45, 46	113/ 30 SW	Granite	Moderate
070806-4	47, 48	285/ 23 N	Diorite	Undeformed
070806-5*	49, 50	068/ 24 S	Granite	Moderate
070806-6	-	095/ 35 S	Granite/ Enclave	Undeformed
070815-1	51, 52	236/72 N	Enclave	Undeformed
070815-2	53, 54	251/ 46 NW	Granite	Moderate

* EBSD
Sample
** Sample lost, replaced by 070815-2

The rock samples were cut into 3x4 cm rock chips to be further cut into thin sections. Two orthogonal thin sections were cut from each sample such that the x, y, and z axes of each thin section are parallel to field x (maximum extension, S_1), y (S_2), and z (maximum shortening, S_3) orientations (Figure 10a). One slide was cut in the xy-plane, the other in the xz-plane. In cases where only a lineation existed and the z and y axes could not be determined, chips with xa and xb planes were cut orthogonal to each other (Figure 10b). Thin sections were cut to a standard thickness of 20 μm and then doubly polished for EBSD analysis. Original rock samples were re-oriented to their field orientation using a sandbox. The orientations of the newly cut xy or xa planes were then measured along with the rake of the x-axis from the strike of the cut face. Using the program *CONAXES* (Brandon 1996), Euler angles (α=cut strike, β= cut dip, γ= rake of x axis with respect to cut strike) of the cut face were calculated to acquire the field orientations of x-, y-/a-, and z-/b- axes for each thin section (Table 3).

Microstructures

Microstructures were analyzed from all thin sections. Careful attention was paid to extinction characteristics, grain aggregate characteristics, grain size distributions, grain boundary shapes, and grain boundary relationships.

EBSD

Electron backscatter diffraction (EBSD) is a technique that is increasingly used to measure the orientations of crystallographic axes and identifying deformation fabrics

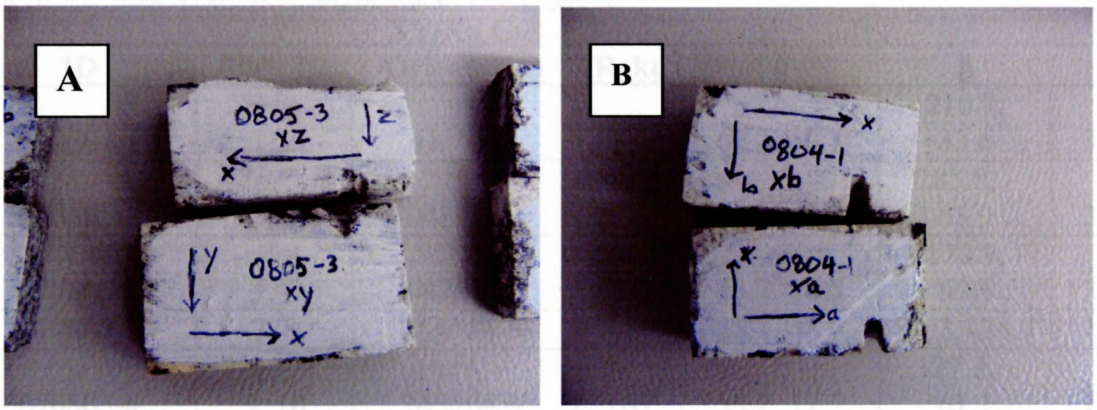

Figure 10: Examples of thin section chips cut from field samples. A- Foliated sample with x, y, and z axes (05-3). B- Undeformed sample with x, a, and b axes (04-1). Chips are approximately 3x4 cm.

Table 3: Thin section orientations (Euler angles)

ID	Slide ID	XY/Xa Cut Orientation	Rake	α	β	γ
070804-1	1, 2	41/ 75 E	55	61.3, 52.3	210.7, 33.6	311, 15
070805-1	3, 4	041/ 68E	170	217.2, 9.3	285.8, -65.9	311, 22
070805-2	5, 6	042/ 76E	15	45.7, 14.5	179.9, 69.6	312, 14
070805-3	7, 8	254/ 61 N	121	35.1, 48.6	90.2, -26.8	164, 29
070805-4	9, 10	245/ 64W	167	59.2, 11.7	127.2, -61.1	155, 26
070805-5	11, 12	269/ 62W	132	61.5, 41	111.9, -36.2	179, 28
070805-6	13, 14	242/ 70W	150	50.8, 28	92.6, -54.5	152.2, 20
070805-7	15, 16	239/ 62N	145	40.8, 30.4	92.8, -46.3	149, 28
070805-8	17, 18	230/ 70W	166	45.1, 13.1	103.9, -65.8	140, 20
070805-9	19, 20	057/ 82S	25	60.7, 24.7	220.4, 63.8	327, 8
070805-10a	21, 22	232/ 79 W	153	46.4, 26.5	72.5, -61.0	142, 11
070805-10b	23, 24	216/ 76W	160	31, 19.4	69.6, -65.8	126, 14
070805-11	25, 26	222/72W	150	31.9, 28.4	70.2, -55.5	132, 18
070805-12a	27, 28	052/ 89E	148	231.4, 32	233.6, -58	322, 1
070805-12b	29, 30	-	-	-	-	-
070805-13**	-	-	-	-	-	-
070805-14	31, 32	000/ 54E	68	55.5, 48.6	166.6, 17.6	270, 36
070805-15	33, 34	024/ 27E	55	75.8, 21.8	172, 15.1	294, 63
070805-16	35, 36	333/ 44W	119	100.6, 37.4	174.7, -19.7	243, 46
070805-17	37, 38	126/ 48N	91	217.5, 48	306.7, -0.7	36, 42
070805-18	-	-	-	-	-	-
070805-19	39, 40	285/ 80S	159	101.2, 20.7	129.3, -66.8	195, 10.
070806-1	41, 42	133/ 33W	89	221.8, 33	312.2, 0.5	43, 57
070806-2	43, 44	295/ 39N	116	57.1, 34.4	135.8, -16	205, 51
070806-3	45, 46	299/ 39N	155	40.8, 30.4	92.8, -46.3	149, 28
070806-4	47, 48	275/ 31N	87	1.5, 31	92.4, 1.5	185, 59
070806-5	49, 50	068/ 65S	31	82.2, 27.8	212.9, 51	338, 25
070806-6	-	-	-	-	-	-
070815-1	51, 52	072/ 62S	36	87.4, 20.2	243.0, 50	298, 23
070815-2	53, 54	122/ 32W	82	220.0, 42	306.1, 1.2	37, 60

Thin sections were not cut for samples with a (-) next to them

** Sample lost, replaced by 070815-2

(e.g., Prior et al. 1999, Prior & Wheeler 1999, Ji et al. 2000, Bestmann & Prior 2003). For a detailed description of the EBSD method, see Prior et al. 1999.

Thin sections for EBSD work were selected to provide transects across major shear zones (Figure 4) and include varying degrees of strain as they appear in hand sample. In addition to an initial double polish, EBSD samples were further polished for up to 14 hours. Good polishing is necessary so the electron source beam interacts with a flat surface, reducing noise from diffraction angles (Prior et al. 1999). A 4.0-4.5 nm thick conductive carbon layer along with a painted conductive carbon boundary grounded to the machine were added to each thin section to reduce electrical charges that limit EBSD precision. Thin sections were analyzed with a working distance of 19.9 mm, an SEM beam of 20.0 kV, and an analysis beam of 10.0 kV. Each section was mapped automatically over a 25x25 grid with a step size of 400 μm. In order to reduce focusing distortion, half of each section was mapped. The SEM was then refocused and the second half of the slide was mapped, allowing for 1250 possible indices of each section. *Flamenco* software was used for data acquisition, data plotting, and calculation of misorientation angles. The poles of quartz and feldspar axes orientations were plotted in stereonets and contoured to distinguish LPO fabrics. Feldspar was indexed as albite because of its similarity to other feldspar crystalline structures (Prior et al. 1999)

Misorientation Index

The misorientation index (m-index) is a numerical technique used to quantitatively assess the strength of crystallographic fabrics based on the frequency of misorientation angles between adjacent grains. Skemer and others (2005) developed the

m-index as an alternative to the less practical J-index. Using the program *m-index*, (Skemer 2005), the frequency of misorientation angles in a given sample are graphed in a histogram with a curve representing the theoretical distribution of random misorientation angles in an undeformed rock. The m-index value *m* is calculated as the standard deviation of the observed misorientation angle distribution from the theoretical random distribution. M-index values of m= 0 are completely random in orientation and m= 1 represents infinitely developed fabrics (Skemer et al. 2005). It is important to point out that the m-index only represent that strength of fabrics; intensity of deformation may be inferred from the m-index only if the deformation mechanisms are well constrained.

Analytically, misorientation distributions that fit the shape of the theoretical curve and have a low m-index value exhibit a weal fabric. As the strength of fabrics increases, the frequency of low (<60º) misorientation angles increases. Graphically, this results in a net movement of data to the left towards lower misorientation angles. Different crystal symmetries (e.g. cubic, rhombohedral, etc.) have different theoretical random misorientation distributions.

RESULTS

Mineralogy

Granitic samples are quartzo-feldspathic with feldspar (~40-45%) dominating quartz (~30-35%) in composition. Twinning and zoning of plagioclase minerals are scarce and myremekite accounts for less than 1% of all feldspars, making identification of plagioclase grains difficult without destructive staining. Micas are common with biotite (~10-15%) more consistent throughout the outcrop than muscovite (~0-5%).

Accessory minerals chlorite and epidote are common in most samples, accounting for 1-2% of total composition. In some instances, chlorite appears as an alteration to biotite grains, while in others it occurs isolated from mica grains. Other accessory minerals include zircon and apatite.

Mafic enclaves are rich in chlorite (30-35%) and micas, particularly biotite (~50%). Spaces between biotite grains are filled with roughly evenly mixed quarto-feldspathic aggregates. Throughout the outcrop, there are no compositional changes between deformed and undeformed samples of granitic wall rock, mafic enclaves, or granodiorite country rock, consistent with observations by Simpson (1983) and Galli and others (2007) in other portions of the Maggia Nappe.

Outcrop

Outcrop descriptions are based on the detailed sketch by Ramsay and Allison (Figure 11) (1979). A weak, pervasive lineation defined by quartzo-feldspathic aggregates and biotite blades is oriented 068 30 E to 080 36E. Shear zones in the outcrop are identified by developments of distinct lineation and foliations, typically of biotite crystals. Shear zones are generally deeply dipping (60°-70°) striking NE-SW and boundaries with wall rock are sharply defined. The outcrop is divided ENE by a single, right lateral shear zone, SZ1, up to 11m wide. Towards the western extent, the shear zone is folded into an ESE trending orientation. A similar trend is observed in the center of the outcrop. At the eastern extent of the map, SZ1 is narrower, about 6m wide. In this portion of the map, SZ1 branches into two narrower (~1 m each) shear zones, SZ1a and SZ1b, which offset the major east trending lamprophyre dike, L1. In the northern portion

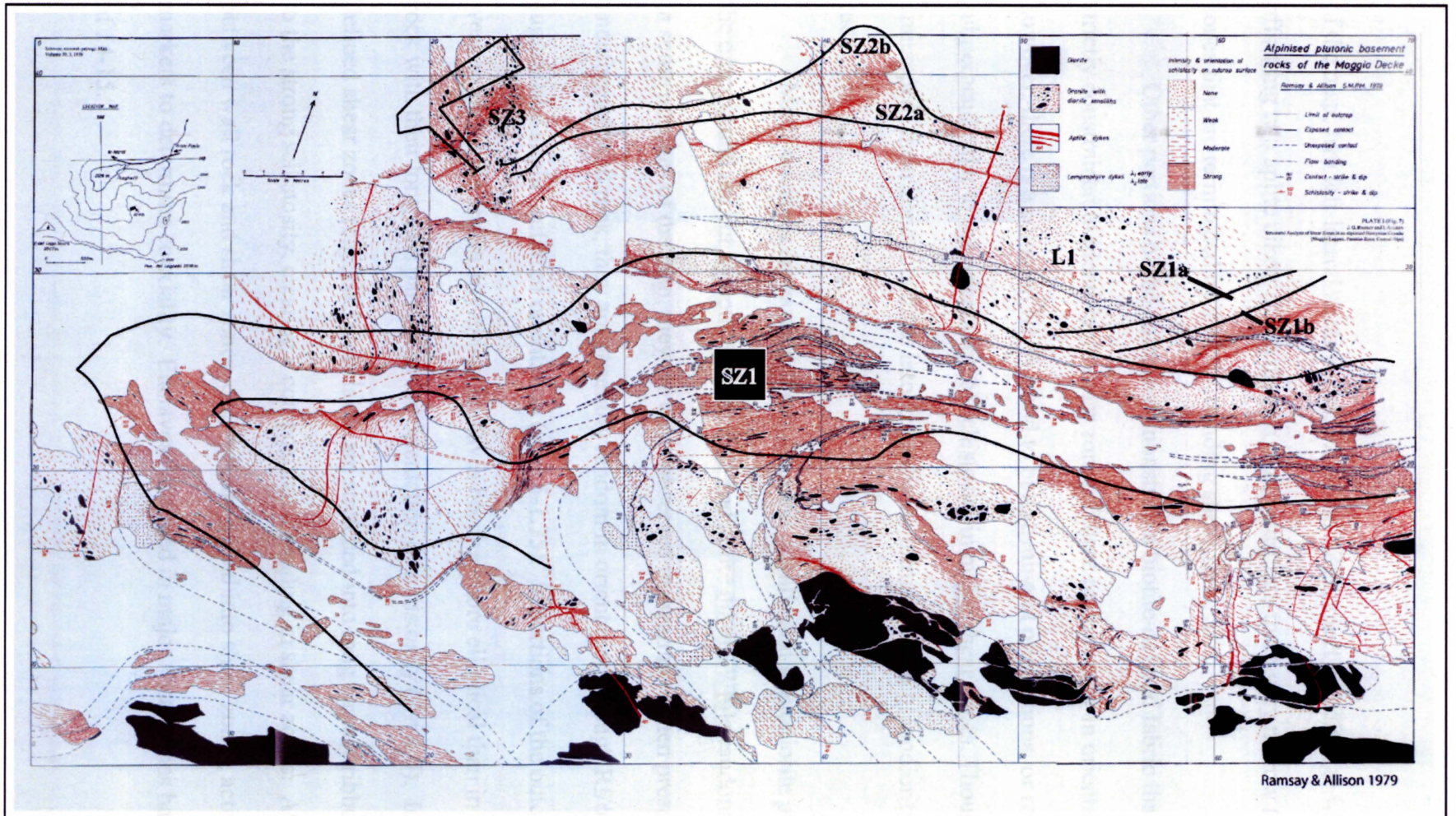

Figure 11: Detailed field map with annotated shear zones (SZ1-SZ3) and major lampophyre dike L1. Modified from Ramsay & Allison (1979).

of the map, two left-lateral shear zones, SZ2a and SZ2b, meet and diverge while offsetting two aplite dikes. SZ2a divides in the west into three very narrow (~1 cm) shear zones that are terminated by a NNW trending shear zone, SZ3.

Other portions of the outcrop demonstrate a biotite-defined fabric that is not strictly constrained to identifiable shear zones. These regions vary in orientation; however, there is a common NNW trend to biotite mineral orientations, or roughly subperpendicular to the orientation of schistosity in major shear zones. Though unmapped, shear zones continue into granodiorite intrusions and granodiorite country rock.

Mafic enclaves are present throughout the granitic and granodiorite portions of the outcrop and are cut by both lamprophyre and aplite dikes. While randomly scattered in some portions of the map, they are often observed in swarms. When present in undeformed wall rock, they are generally random in orientation, though Rf/ϕ analysis has suggested a slight preferred orientation (γ= 1.5-1.75). In portions of the outcrop where a weak to moderate schistosity exists, enclaves become more elliptical than in undeformed rock with their long axis parallel to the orientation of schistosity (γ = 4-5). In well-defined shear zones (e.g., SZ1), enclaves are stretched into long narrow ribbons parallel to the strong schistosity, creating a compositional banding in shear zones. At boundaries between wall rock and shear zones, enclaves are pulled into shear zones, acting as strain markers to determine coaxiality. Enclaves deformed in major shear zones have γ values of 14-15.

Microstructures

Thin sections are described below in three categories based on hand sample characteristics: undeformed/poorly deformed, moderately deformed, and well deformed. Undeformed/poorly deformed samples (Fig. 12 a) demonstrate only a weak lineation where biotite and feldspar porphyries retain their original shape. Moderately deformed samples (Fig. 12 b) display a strong lineation or weak to moderate foliation and are located either in deformed portions of the rock unconstrained by defined shear zones or along major shear zone boundaries where grain deflection is not sufficient to define a strong foliation. Well-deformed samples (Fig. 12 c) display characteristics of highly deformed rocks, including gneissic or mylonitic textures. All samples are described according to grain and aggregate characteristics established by Moore (1970, figure 13). All photomicrographs referenced below are found in Appendix A.

Undeformed/Poorly Deformed Samples

04-1, 05-14, 05-15

Poorly deformed samples are separated into two grain size aggregates: very coarse grain (VCG, 0.8-1+ mm) quartzo-feldspathic and biotite grain aggregates, and another of coarse-medium grain (100-500 μm) quartz, feldspar, and muscovite grain aggregates. Very coarse epidote grains and medium grain chlorite grains are evenly distributed amidst VCG and coarse-medium grain aggregates.

VCG Aggregates Characteristics

VCG aggregates (App. A.1) contain a nearly equal concentration of quartz and feldspar grains that display no preference towards formation of larger or smaller grains

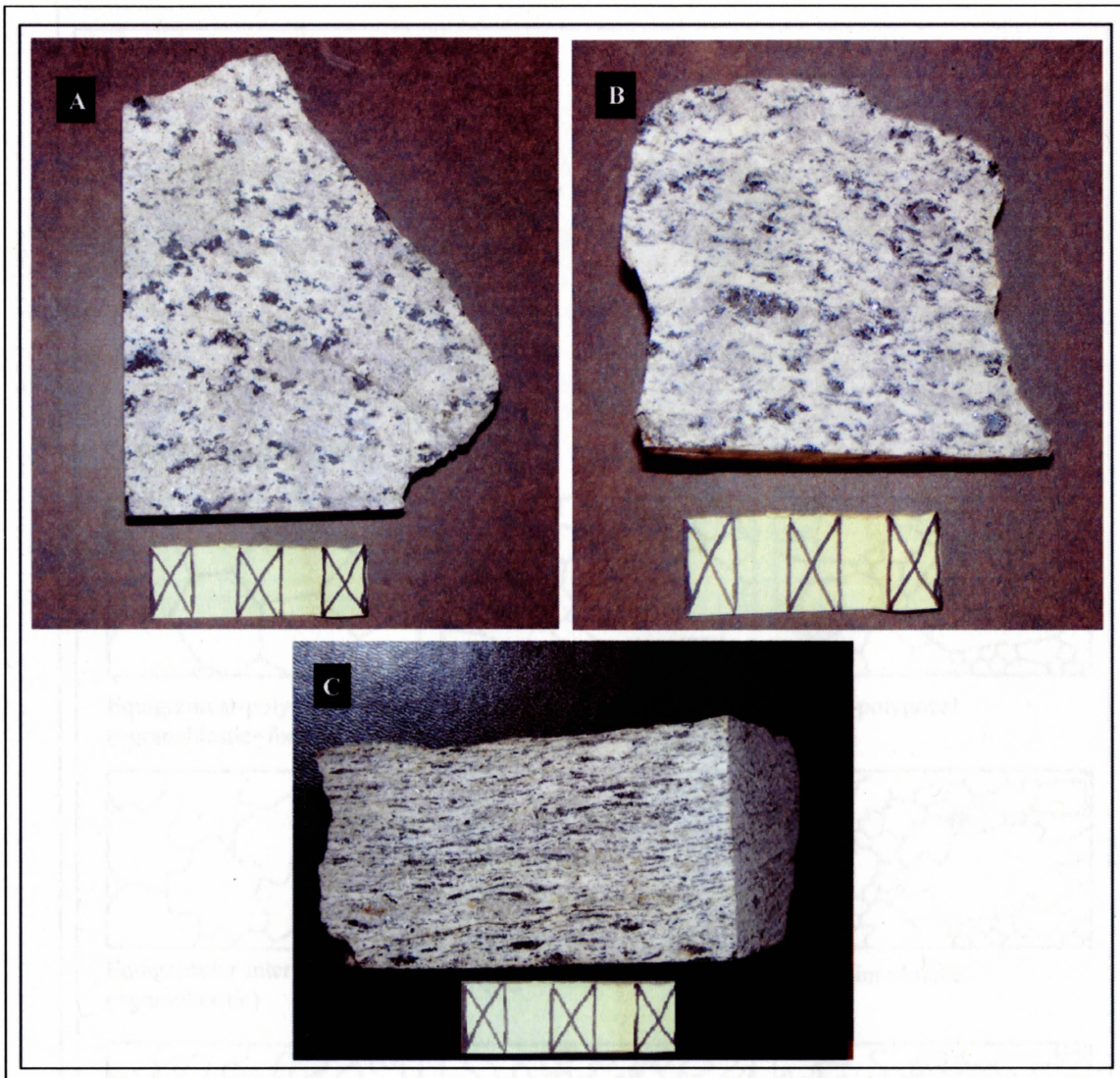

Figure 12: Common deformation fabrics. A- Undeformed (04-1). B- Moderately deformed (05-12) C- Well deformed (05-9). Scale bar = 5 cm.

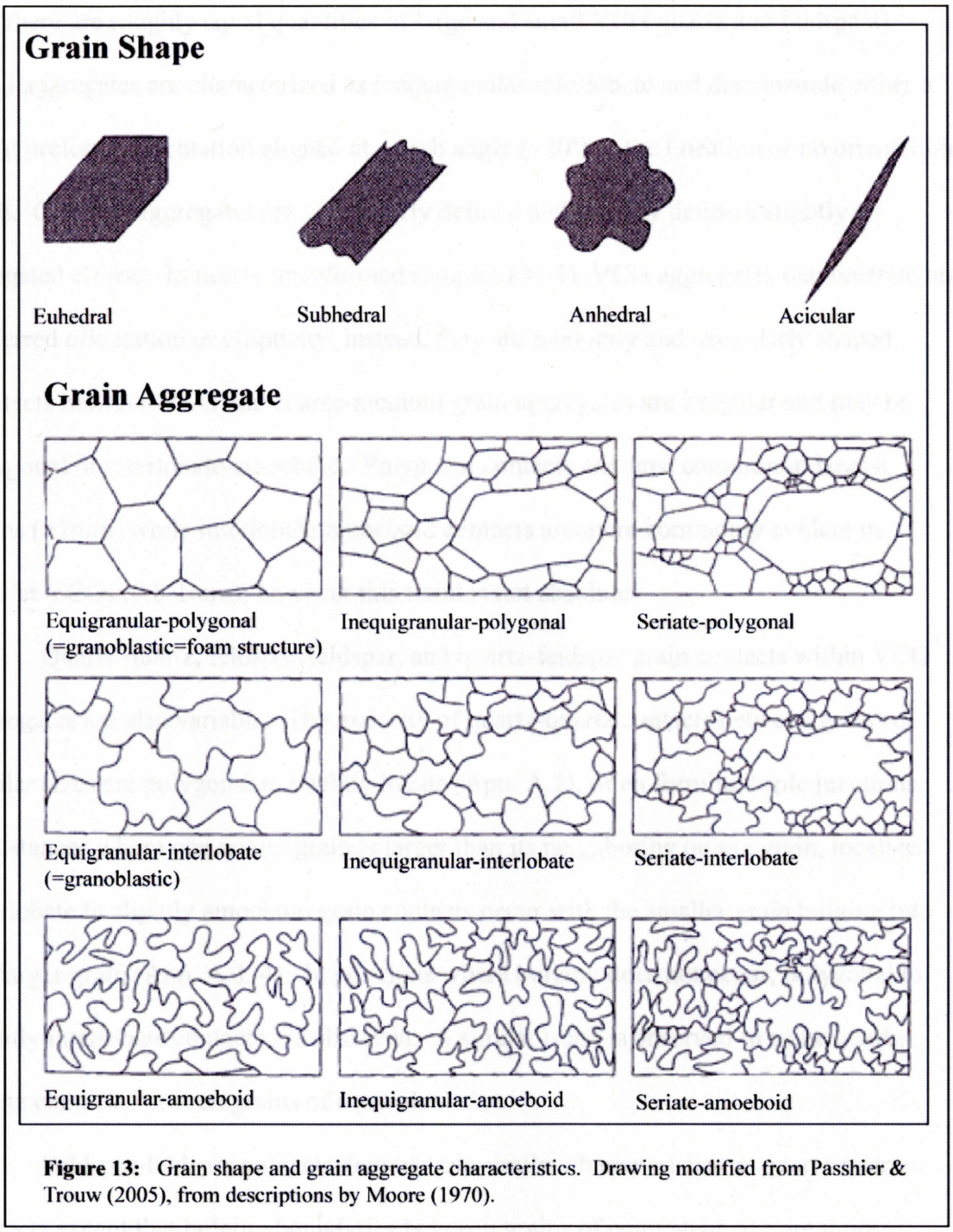

Figure 13: Grain shape and grain aggregate characteristics. Drawing modified from Passhier & Trouw (2005), from descriptions by Moore (1970).

(ie., there are roughly equal quantities of large and small VCG quartz and feldspars). VCG aggregates are characterized as inequiganular-interlobate and demonstrate either a slight preferred orientation aligned at a high angle (~20°) to the lineation or no orientation at all. Oriented aggregates are very poorly defined and roughly define a slightly elongated ellipse. In nearly undeformed samples (04-1), VCG aggregates demonstrate no preferred orientation or ellipticity; instead, they are randomly and irregularly shaped. Contacts between VCG and coarse-medium grain aggregates are irregular and may be polygonal or interlobate-amoeboid. Polygonal contacts are most common in largest grains (>1mm) while interlobate-amoeboid contacts are more commonly evident in smaller VCGs (0.8-1mm); however this trend is not absolute.

Quartz-quartz, feldspar-feldspar, and quartz-feldspar grain contacts within VCG aggregates are also variable. The majority of quartz-quartz contacts between grains of similar sizes are polygonal to slightly lobate (App. A.2), often forming triple junctions. In instances where one quartz grain is larger than its neighboring quartz grain, localized interlobate to slightly amoeboid grain contacts occur with the smaller grain bulging into the larger grain (App. A.3, 4). In positions where bulging does not occur, polygonal to slightly interlobate contacts are observed. A similar trend is observed in some quartz-quartz contacts between grains of equivalent size.

Feldspar-feldspar contacts demonstrate similar characteristics as quartz-quartz contacts except that bulging boundaries between grains of equivalent size are more common than in quartz-quartz contacts.

Quartz-feldspar contact characteristics are variable (App. A.5). At contacts between similar sized grains, polygonal contacts form along straightened sides of grains.

Localized, small scale bulging occurs along these long contacts in which feldspar bulges into quartz grains. In some instances, straight contacts are curved with the feldspar convexly bulging into the quartz grains. At contacts near corners or points of grains, contacts are highly interlobate to amoeboid with feldspar bulging into quartz grains. When quartz grains surround a feldspar grain, contacts are strongly interlobate to amoeboid, though it is difficult to determine which grain boundaries bulge.

VCG biotites accumulate into aggregates that have a preferred orientation subparallel to the x-axis in poorly deformed samples in both xy- and xz-sections. Aggregates have very distinct, straight contacts with both VCG and coarse-medium grain quartzo-feldspathic aggregates. Individual VCGs within aggregates, however, exhibit little preferred orientations and are almost entirely subhedral to euhedral in shape. Grains are normally too thick to exhibit extinction characteristics, let alone interference colors.

VCG Individual Grain Characteristics

Individual VCG quartz displays varying extinction characteristics, but a lack of undulatory extinction is common. Generally, there is only very subtle sweeping undulatory extinction. Some grains display distinct tapered deformation bands while fewer others demonstrate a strong sweeping undulatory extinction. Deformation bands are particularly pervasive along irregularly shaped grain boundaries and where portions of larger grains appear to be nearly pinched off (App. A.6). ~70% of VCG quartz is anhedral, ~30% is subhedral, and <1% is euhedral.

VCG feldspars demonstrate deformation bands and sweeping undulatory extinction (App. A.7), though complete extinction is most common. Sweeping

undulatory extinction is more pronounced than in quartz grains and tends to radiate from point contacts or bulges in adjacent grains. Deformation bands are uncommon in VCG feldspars.

Large (1-2mm) plagioclase poikiloblasts with fine to very fine quartz and muscovite grains are common (App. A.8). Muscovite grains demonstrate no preferred orientation and quartz grains are well-rounded and exhibit undulatory extinction radiating outward from the center of grains.

Coarse-Medium Grain Aggregate Characteristics

Coarse-medium grain aggregates (App. A.9) are highly variable in distribution of minerals. Depending on sample, aggregates are roughly evenly distributed among quartz and feldspar grain counts while other portions are dominated by either feldspar, quartz, or muscovite with feldspar the most common single-mineral aggregate. Transitions between single mineralogy-dominated regions are sudden with no apparent tapering or relationship to VCG aggregates. No feldspar aggregates are located directly adjacent to quartz aggregates, but muscovite aggregates form contacts throughout all coarse-medium grain aggregates. Aggregates are inequigranular-interlobate and account for 70-80% of all grains. Single VCGs, especially plagioclase poikiloblasts, are present randomly throughout these aggregates. Contacts between poikiloblasts and finer quartzo-feldspathic aggregates are highly interlobate.

Feldspar-feldspar contacts in coarse grains are variably polygonal and lobate/ anhedral with distinct, small scale bulges. Contacts between coarse and medium feldspars are generally polygonal, forming triple junctions with other coarse and medium

feldspar grains. Where a medium grain is a daughter grain of an older, coarser parent grain, grain contacts are lobate. Contacts between medium feldspar grains range from strongly polygonal to interlobate with some having lobate grain boundaries. Bulging between grains of equal size is common and on a larger scale than in VCG aggregates. Grain contact characteristics are randomly dispersed throughout the samples, i.e. there are no areas that display only polygonal or lobate grain boundary characteristics.

Quartz-quartz contacts are generally lobate to slightly interlobate, forming poorly defined grain shapes. Bulging boundaries occur, normally between grains of different sizes. Subhedral to nearly euhedral grains are often located in close proximity to highly anhedral grains that appear as though they have been pulled and stretched apart. The orientations of these stretched grains are random with respect to lineations.

Quartz-feldspar contacts in coarse-medium grain aggregates are similar to those in VCG aggregates, though boundaries are more lobate than polygonal and straight. Bulging relationships are common with feldspar grains bulging into quartz grains when grains are of unequal size. Contacts between grains of similar size demonstrate little bulging relationships.

Muscovite aggregates are common in feldspar and feldspar-quartz coarse-medium grain aggregates. In undeformed samples (04-1), muscovites are randomly oriented while in poorly deformed samples, muscovites have a distinct shape preferred orientation; however the orientation of individual grains and grain aggregates are independent of lineation orientations.

Individual Coarse-Medium Grain Characteristics

Quartz grains are inconsistently shaped. They range in shape from highly polygonal to highly anhedral (App. A.10, 11). Coarser grains tend to be highly anhedral and poorly defined. Medium grains range in shape from anhedral to subhedral, with the smaller range of quartz grains constituting the largest population of subhedral and nearly euhedral grains, though the majority is anhedral-subhedral. Deformation-related extinction patterns are not pervasive in quartz, but extinction patterns that are present are correlated to grain shapes. Where present, undulatory extinction is observed in highly anhedral, irregularly shaped grains where a subgrain is present. In some cases, sweeping undulatory extinction radiates outward through the parent grain from its contact point with the subgrain or with a non-quartz inclusion. In other cases, a bulged portion of a quartz grain demonstrates uniform extinction at a different angle from the rest of the grain without undulatory extinction. Undulatory extinction is very uncommon in medium, subhedral to anhedral grains and seldom observed in anhedral medium grains. Deformation bands are extremely rare and where present, they are subtle and only found in coarse grains usually near subgrains.

Feldspars demonstrate similar shape characteristics as quartz. Coarse grains are anhedral to subhedral and are often pulled apart. A much higher percentage of medium grains though are well-defined subhedral to euhedral than quartz, though the majority is anhedral. Undulatory extinction is pervasive throughout feldspars. Sweeping undulatory extinction is most common, especially in coarse grains where subgrains are present. Like quartz, sweeping undulatory extinction radiates outward from inclusions or through the parent grain from the point of contact with the subgrain. In medium grains where no subgrain is observed, sweeping undulatory extinction radiates outward from discrete

contact points with neighboring feldspar grains. Where subgrains are adjacent to medium parent grains, the two grains demonstrate uniform extinction at different angles. Deformation bands are present in coarse grains but are uncommon.

Coarse-medium grain biotite blades are acicular and isolated from other biotite grains in coarse-medium aggregates (App. A.12). Acicular blades in undeformed/poorly-deformed samples are aligned with long axis subparallel to the x-axis.

Moderately deformed samples

05-1, 05-2, 05-3, 05-4, 05-5, 05-6, 05-12, 05-16, 05-18, 05-19, 06-1, 06-3, 06-5, 15-2

Moderately deformed samples represent a wide range of possible shear strains ($\gamma \sim$ 2-5) transitioning from undeformed samples to the highly deformed foliated gneisses of shear zones.

VCG Aggregate Characteristics

VCG aggregates in moderately deformed samples are partitioned into two phases: thick (>5 grains) and narrow (<5 grain) aggregates. Elongated VCG aggregates become better defined and identified with increasing strain. Thick VCG aggregates are present in all moderately deformed samples but are most common in samples located furthest from shear zone boundaries (05-3, 05-5, 05-16, 15-2). The shapes of thick aggregates are difficult to constrain because they are often truncated by thin section slide boundaries; however, they appear to form a poorly defined ellipse of low ellipticity. The long axis of these aggregates is subparallel to to the x-axis. Thick VCG aggregates are often narrowly cut by medium grain quartzo-feldspathic or muscovite aggregates whose trend is parallel

to the x-axis (App. A.13). Where thick VCG aggregates are not cut by medium grain aggregates, they are often bound by coarse grain biotite aggregates in which biotite grains align with their long axis parallel to their contact with the VCG aggregate (App. A. 14). Where thick aggregates are bound by biotite grains, outer grain contacts are polygonal, reflecting the shape of subhedral biotite grains (App. A.14). Contacts with quartzo-feldspathic coarse-medium grain aggregates are interlobate to polygonal with the presence of coarse subgrains common. In more well deformed samples (e.g., 05-12, 05-4, 05-19), a seriate-interlobate texture develops in which grain size grades downward from VCG to coarse to medium grains.

Quartz-quartz contacts in thick VCG aggregates are mostly lobate and interlobate; however, in some samples, contacts are highly polygonal. While not common, portions of a single quartz grain bulges substantially into a neighboring quartz grain of equal size. Where quartz grains of differing size contact, the smaller grains appear to bulge into the larger grain.

Feldspar-feldspar contacts are lobate and less interlobate than quartz-quartz contacts. Small bulges are common in portions of contacts between grains of equal size.

As VCG aggregates become thinner (1-5 grains) they are clearer to identify and align subparallel to the x-axis. Narrow VCG aggregates in the xz-plane of some samples constitute ribbons of only 1 or 2 grain thickness (App. A.15). Ribbon boundaries are more straight and polygonal than thick VCG aggregates; however, they still exhibit overall interlobate contacts with surrounding medium grain aggregates. Ribbon shapes become straighter with progressive deformation and are sinusoidal at lower deformation (i.e. further from shear zone center). Contacts with coarse grain biotite aggregates are

highly polygonal, especially where biotite grains demonstrate a shape-preferred orientation. Along the long sides of ribbons, VCGs directly contact medium grain quartzo-feldspathic aggregates with no seriate graded texture. At the tips of each ribbon, though, the ribbon grades down to medium grains through a region of erratically shaped and fractured grains, making identification of the ends of ribbons difficult. The rest of the ribbon retains a well-defined consistent shape and thickness. These ribbons are not observed in the xy-plane of samples. Instead, VCG aggregates develop into broad, randomly shaped regions with no shape-preferred orientation.

Grain contacts between grains in narrow VCG aggregates/ribbons are highly polygonal, particularly between larger grains of equal size. Smaller grains demonstrate more lobate boundaries; however, interlobate contacts are uncommon. Some bulging boundaries occur between large quartz grains and rounded coarse quartz subgrains are found both inside and along the edges of ribbons. Generally, small-scale bulging and subgrain relationships are not observed as they are in thick VCG aggregates. Ribbons are partitioned into alternating portions dominated by either quartz or feldspar grains with no sense of graded transition (App. A.16). The fractured, poorly defined ribbon ends are dominated by feldspar grains with some isolated quartz grains.

VCG biotite aggregates define a moderately to well defined lineation parallel to subparallel to the x-axis. Grains that constitute aggregates demonstrate a variable shape-preferred orientation relative to their aggregate. Where aggregates form along VCG quartzo-feldspathic aggregates, grains have a shape-preferred orientation with long sides parallel to the contact with quartzo-feldspathic aggregate. Individual grains in thick biotite aggregates have a poorly defined shaped-preferred orientation with grains roughly

subparallel to the x-axis. Thinner biotite aggregates consist of smaller VCG grains than thick aggregates. These grains demonstrate a more defined shape-preferred orientation oriented subparallel to the x-axis. Smaller grains in thick biotite aggregates are also aligned subparallel to the x-axis.

VCG Individual Grain Characteristics

VCG feldspar grains are similar in shape to those in undeformed/poorly-deformed samples. Larger grains are subhedral to anhedral. Large feldspar grains are squeezed into spaces between quartz and other feldspar grains, forming highly irregular, anhedral portions of a single grain. Feldspar subgrains nucleated from VCG feldspars are rounded with slightly anhedral grain boundaries. Most very coarse feldspar grains display undulatory extinction. Where a subgrain is present, a sweeping undulatory extinction radiates outward though the parent grain from the contact point with the daughter subgrain. Sweeping undulatory extinction exists in some grains without a subgrain. Zoned extinction is more common in these grains with deformation bands developing in some. Many grains demonstrate differential uniform extinction angles about discrete lines that divide a single grain into two or more regions. Often, different extinction angles will meet at a triple junction at the center of a feldspar grain.

Very coarse quartz grains are variable in shape depending on aggregate size. Quartz grains in thick VCG aggregates are anhedral and inconsistently shaped and sized. They demonstrate two subtle undulatory extinction characteristics. Sweeping undulatory extinction radiates through the grain from cuspate contacts with other grains or from contacts with subgrains. Deformation bands are more common in smaller, more

rounded/elliptical grains. Many grains exhibit similar extinction characteristics as VCG feldspars in which a single grain is divided into two or more independent zones of uniform extinction.

Quartz and feldspar poikiloblasts demonstrate two shape characteristics. When located in the vicinity of VCG aggregates that do not demonstrate elongation, poikiloblasts appear generally undeformed as well, retaining their original sense of sphericity. Subhedral muscovite inclusions do not demonstrate any shape-preferred orientation either. Poikiloblasts isolated in medium grain aggregates or located near elongated VCG aggregates demonstrate elongation characteristics with a long axis subparallel to the x-axis (App. A.17, 18). Muscovite inclusions also demonstrate a sense of rotation orientation subparallel to the x-axis. Feldspar poikiloblasts exhibit a greater tendency than quartz to deform into an orientation parallel to the x-axis of a sample.

Coarse-Medium Grain Aggregate Characteristics

Coarse-medium grain aggregates represent a more consistent medium grain size than in poorly deformed samples. Coarse grains are most common in graded regions between VCG aggregates and coarse-medium grain aggregates. Some isolated coarse grains, both quartz and feldspar, are scattered throughout medium grain aggregates. At lower deformation, coarse grains are more common and sometimes form into small (3-10 grains) aggregates, particularly of feldspar grains, but these aggregates disappear with progressive deformation.

Medium grain aggregates are divided into three groups by mineralogy: feldspar-only aggregates, quartz-feldspar aggregates, and quartz dominant aggregates. Unlike

undeformed/poorly-deformed samples, no quartz-only aggregates exist. Feldspar-only aggregates are equigranular to inequigranular-polygonal. Interlobate contacts with subtle bulges develop between larger grains. Some feldspar aggregates are inundated with medium grain muscovite swarms where individual grains have a defined shape preferred orientation subparallel to the x-axis. Large muscovite swarms have no defined shape or preferred orientation though. These swarms also appear to have no effect on felspar aggregate characteristics, instead appearing more like an overprinting fabric. In some samples, very fine-grained muscovite swarms migrate into narrow (~25-50 μm) ribbons aligned subparallel to the x-axis. Individual grains in these ribbons are rounded through and do not have the common shape attributed to mica minerals. Muscovite swarms are often found in close proximity to coarse epidote grains or VCG biotite aggregates. The presence of muscovite swarms varies between samples.

Feldspar aggregates grade into quartz-feldspar aggregates and grain contacts become less polygonal and more interlobate for feldspar-feldspar, quartz-feldspar, and quartz-contacts. Grain contacts in quartz-feldspar aggregates are poorly defined; though, visible contacts are highly lobate and aggregates are inequigranular. Bulging relationships are observed with feldspar grains bulging into quartz grains. This is most common where quartz grains are larger than adjacent feldspar grains. Finer portions of medium grain aggregates result in rounded, lobate grain boundaries between feldspar and quartz grains.

Quartz dominated aggregates are smaller in area compared to feldspar-only aggregates. Grain contacts are very difficult to discern and are highly irregular. Complicated interlobate are amoeboid relationships develop between quartz grains and

subgrains of low misorientation angles (as determined by extinction angles) are present. Muscovite swarms in quartz dominant aggregates contain grains that are variable in orientation. In more deformed samples, muscovite grains demonstrate a preferred orientation subparallel to the x-axis; however, this trend is quickly lost with less deformation as grains become randomly oriented.

Coarse-Medium Grain Individual Grain Characteristics

Feldspar grains that constitute feldspar-only aggregates are euhedral to subhedral with more lobate grain boundaries in coarser grains. Some medium grain feldspar grains have a euhedral square shape that aligns with long edges subparallel to the x-axis. These grains are most common at boundaries between narrow VCG ribbons and coarse-medium grain aggregates. Almost all coarse feldspar grains have a very distinct undulatory sweeping extinction that radiates outward from a highly convex grain boundary or subgrain contact. Other grain that do not have such contacts exhibit sweeping undulatory extinction radiating outward from the center of the grain. Undulatory extinction is common in medium feldspar grains as well. Sweeping undulatory extinction is most common and radiate outward from discrete, indistinct points. Deformation bands and uniformed zoned extinction are very uncommon in feldspar grains while a small percentage (~15%) demonstrates no undulatory extinction at all.

Coarse quartz grains are generally anhedral to subhedral and are irregularly shaped. Undulatory extinction is not as pervasive as in feldspars, but where it is present, sweeping undulatory extinction radiates outward from the center of coarse grains. Very few coarse grains demonstrate deformation bands or differential zones of uniform

extinction. Medium quartz grains have a more homogenous shape: subhedral and rounded. Undulatory extinction is very uncommon in medium quartz grains, especially in smaller grains that almost fine grained. Undulatory extinction is most prevalent in quartz grains that are surrounded by feldspars that exhibit a high degree of undulatory extinction.

Well-deformed Samples

(05-7, 05-8, 05-9, 05-10, 05-11, 06-2)

Well-deformed samples are taken from the center of shear zones where biotite-foliation is strongest. Each sample is unique in its degree of strain with some demonstrating a strong foliation while others demonstrate mylonitic characteristics. The extent of strain in well-deformed rocks is classified according to the degree with which biotite clots are elongated and thinned, with very narrow (50-100 μm), straight clots representing the most deformed samples. For the purpose of description and discusson, well-deformed samples in order of increasing deformation grade are: 05-10, 05-11, 05-7, 05-8, 05-9, and 06-2. Again, samples are divided between VCG aggregates and coarse-medium grain aggregates.

VCG Aggregate Characteristics

All VCG aggregates are deformed into elongated ribbons parallel to the x-axis as observed in the xz-plane (App. A.19). These ribbons vary in width with deformation grade from >1 mm (05-10) to <250 μm (all samples) though there is a tendency toward thinning with more intense deformation as thick (5+ grain) ribbons are not observed in

the most deformed samples (05-8, 06-2). Thick aggregates in the least deformed samples (05-7, 05-10) develop 2-3 narrow ribbons parallel to the x-axis along their boundary. In less-deformed samples (05-10 through 05-7), some ribbons, particularly more narrow ribbons (1 grain), are sinusoidal in shape. This characteristic is lost with stronger deformation and never observed in thicker (>1 grain) ribbons of any of the well-deformed samples. While VCG ribbons vary in length, some are continuous over the extent of an entire thin section. Quartz grains generally dominate quartzo-feldspathic VCG aggregates. Ribbon contacts with coarse-medium grain aggregates are not polygonal; however, they do not demonstrate the interlobate, interfingering characteristics observed in samples not related to the center of shear zones. VCG boundaries at the edges of ribbons are irregular with sharp, unrounded corners, appearing as though they have been superimposed on top of coarse-medium grain aggregates (App. A.20). Like moderately deformed samples, biotite grains often bound VCG ribbons, forming polygonal contacts that morph to the subhedral/euhedral shape of biotite grains. In the most deformed sample, 06-2, ribbon contacts are polygonal where VCG quartz juxtaposes smaller feldspar grains, slightly irregular and sharp edged where VCG feldspar juxtaposes smaller quartz and feldspar grains, and gently interlobate where VCG quartz juxtaposes smaller quartz grains.

In less deformed samples (05-10 - 05-7) the ends of ribbons terminate abruptly, often with a swarm of coarse fractured quartz grains. The ends of more deformed ribbons (05-9, 06-2) are dominated by feldspar grains that grade down in size from VCG to the grain size of the surrounding aggregate. These bounding feldspar grains do not exhibit a

fractured appearance as they do in moderately deformed samples. Sample 05-8 demonstrates a transition between the two different types of ribbon termination.

In xy-plane thin sections, VCG ribbons are not developed. Instead, VCG aggregates are broad and irregularly shaped. At times, they may have a subtle ellipticity with long axis aligned parallel to the x-axis. VCG aggregates vary greatly in size and may be may contain 20+ grains. These aggregates demonstrate the same contacts (described above) and internal grain characteristics (described below) as VCG ribbons in the xz-plane.

Quartz-quartz contacts in VCG aggregates (in both xy and xz sections) are generally polygonal with some sharp, cuspate boundaries, particularly among the largest grains. Smaller quartz grains form subtly bulging, broadly lobate contacts with larger quartz grains. This is especially evident in poorly developed VCG ribbons. Larger quartz grains also tend to develop more lobate or polygonal interlocking contacts in poorly developed ribbons of less deformed samples.

Feldspar-feldspar contacts are more irregular than quartz-quartz contacts. Contacts range in character from polygonal and sharply cuspate to interlobate. Interlobate grain boundaries may be highly interlocking with small-scale bulges or broadly lobate as in quartz-quartz contacts. Small, round bulges between feldspar grains are common. Because quartz grains dominate VCG ribbons, feldspar-feldspar contacts are uncommon.

Quartz-feldspar contacts are similar in morphology to feldspar-feldspar contacts, though polygonal and sharply cuspate contacts are rare. Interlobate contacts are more common with large, rounded bulges into quartz grains.

In xz-plane thin sections, VCG biotite aggregates thin and become straighter with stronger deformation. Biotite aggregates are parallel to subparallel to the x-axis. Individual grains are rotated such that their long axis (<010> and <221> planes) oriented subparallel to the x-axis. In the xy-plane, biotite aggregates are elongated parallel to the x-axis; however, this direction is not defined as clearly as in xz-sections because the <001> plane of individual biotite grains are oriented parallel to the xy-plane, effectively defining the foliation. Individual grains with <001> face skew to the xy-plane demonstrate a shape-preferred orientation parallel to the x-axis. VCG biotite aggregates are not present in the most deformed sample (06-2).

Individual VCG Characteristics

Very coarse feldspar grains in thick VCG ribbons are subhedral to anhedral, depending on adjacent mineralogy. Larger feldspar grains are more irregularly shaped, appearing as though they have been squeezed between neighboring grains and spread out into an anhedral shape. Elongated anhedral feldspar grains have no shape-preferred orientation in either xy or xz sections. Smaller VCG feldspars, including subgrains and large bulges, are more rounded with curved, less erratic boundaries. Undulatory extinction is rare in all VCG feldspar grains. Sweeping undulatory extinction is least evident (1-2% of grains) and is most commonly observed in highly rounded subgrains. Extinction radiates outward through the grain from sharp contacts with adjacent grains. Sweeping undulatory extinction is not observed in the most deformed samples (06-2). Deformation bands are observed in large, highly anhedral and erratically shaped feldspar grains. Seldom, block, subhedral feldspar grains exhibit wide, parallel deformation

bands. Like sweeping extinction, deformation bands are not evident in the most highly deformed samples (05-9, 06-2).

In less deformed samples (05-10, 05-7), very coarse quartz grains are subhedral to anhedral in thick and ribbon aggregates. In high deformation samples (05-9, 06-2), quartz grains are subhedral to slightly euhedral and have a blocky, sharp cornered appearance. Undulatory extinction is very rare, but when present, deformation bands develop in subhedral grains in less deformed samples.

Quartz and feldspar poikiloblasts are anhedral and not associated with VCG aggregates. In both xy and xz planes, poikiloblasts are elongated with their long axis and muscovite inclusions oriented parallel to the x-axis, though muscovite inclusions disappear with increasing deformation grade. Quartz inclusions are rounded with no shape preferred orientation. Poikiloblasts are not observed in the most deformed (06-2) sample. In addition to strained poikiloblasts, VCG epidote porphyroblasts are strained into an elliptical shape with long axis oriented subparallel to the x-axis in both xy and xz planes.

Fine-Medium-Coarse Grain Aggregate Characteristics

Characteristics of medium-coarse grain quartzo-feldspathic aggregates vary greatly with increasing deformation, so their description is divided between lower and higher grades. Also, an appreciable quantity of fine grains (<100 μm) are present and compose 15-20% of non-VCG aggregates.

<u>Samples 05-10, 05-11, 05-7</u>

Coarse grains are spread throughout medium grain dominated aggregates and rarely cluster adjacent to other coarse grains. Coarse grains are anhedral to subhedral with bulging contacts with adjacent grains. At times, fine grain, acicular biotite grains bound independent coarse grains, giving them polygonal or gently lobate grain boundaries.

Medium-fine grain aggregates are messy and a wide distribution of grain shapes and are inequigranular-interlobate to inequigranular-polygonal with a random distribution of medium and fine grains. Medium and fine grain contacts are lobate and polygonal with no interfingering relationships. Medium-medium grain contacts range in shape from highly anhedral to polygonal, with contact relationships not restricted to particular mineral combinations.

Samples 05-8, 05-9, 06-2

With increasing deformation grade, all grain sizes are divided into single-grain size aggregates. Coarse grains arrange into narrow (1 grain wide) equigranular-polgonal (granoblastic) ribbons that align parallel to the x-direction (App. A.21). Medium and fine grain quartz and feldspar are arranged into equigranular-interlobate (granoblastic) aggregates with fine grains decreasing in occurrence in the highest-grade sample (5-10% in 06-2). Grain size grades between fine and medium grain aggregates, creating intermediate inequigranular-interlobate aggregates with no apparent shape-preferred orientation. Again, there are feldspar-only, feldspar-quartz mixed, and quartz-dominant aggregates with a grading of mineralogies in between. Feldspar-feldspar contacts are polygonal with sharp corners and some small-scale cuspate bulges. Feldspar-quartz and

quartz-quartz contacts are interlobate and rounded. Some small-scale bulges develop, particularly where quartz bulges into adjacent feldspar grains. Medium grains with a lobate shape orient subparallel to the x-axis.

Individual Fine-Medium-Coarse Grain Characteristics

Coarse grain feldspars in the most deformed samples are strongly subhedral to euhedral, particularly when they are found in narrow ribbons. Sweeping undulatory extinction is common in coarse grains in which extinction radiates outward from the center of the grain. In lobate grains, deformation bands are commonly observed oriented perpendicular to the long axis of the grain. Medium and fine grain feldspars are more rounded and anhedral, demonstrating a reduced grain boundary area compared to less-deformed samples. Sweeping undulatory extinction is common, radiating outward through the grain from either the center of the grain or from point-contacts with adjacent grains.

Coarse quartz grains range in shape depending on adjacent grain shape. When contacting other coarse quartz grains, individual grains are subhedral. Coarse quartz grains develop an anhedral shape when isolated in a medium-fine grain matrix. Medium and fine grain quartz are rounded and subhedral to euhedral, again demonstrating a reduction of grain boundary area. Undulatory extinction is very uncommon in quartz grains. When present, there is an equal distribution between grains that demonstrate sweeping undulatory extinction and deformation bands.

Medium grain biotite is acicular and ungrouped with other biotite grains in the most deformed samples. They align with their long axis parallel to the x-axis.

LPO Results

QuartzLPO

Quartz LPO data was collected from 13. There are four stereonet diagrams for each sample representing the four different quartz crystallographic axes. <0001> represents c-axis orientations, while upper and lower <11-20> hemispheres represent two a-axes orientations and <10-10> represents the third a-axis orientation.

Undeformed Samples (Figure 14)

(04-1, 05-14, 05-15)

Sample 04-1 demonstrates a slightly higher concentration of points in the NE hemisphere; however, this is only 2-2.5x expected concentration. A-axes plots demonstrate no regions of high orientation. In sample 05-14, the majority of c-axis orientations are concentrated in the northern hemisphere with a localized concentration (3-4x expected concentration) in the NW hemisphere above the x-axis. These points are very close together and appear to overlap. A curved region void of orientations stretches from the lower SSW hemisphere into the NE hemisphere. Regions of neither high nor low a-axis orientations are present. Sample 05-15 c-axis orientations are absent in two portions of the stereonet located directly across from each other at the edges of the stereonet: the WNW and ESE regions. Another smaller pointless region develops on the NNW edge of the steronet. In the SW quadrant, points are clustered into a maximum of 3x expected concentration. A slight high also develops at the center of the stereonet with ~2x expected concentration of points. High a-axes orientation concentrations develop

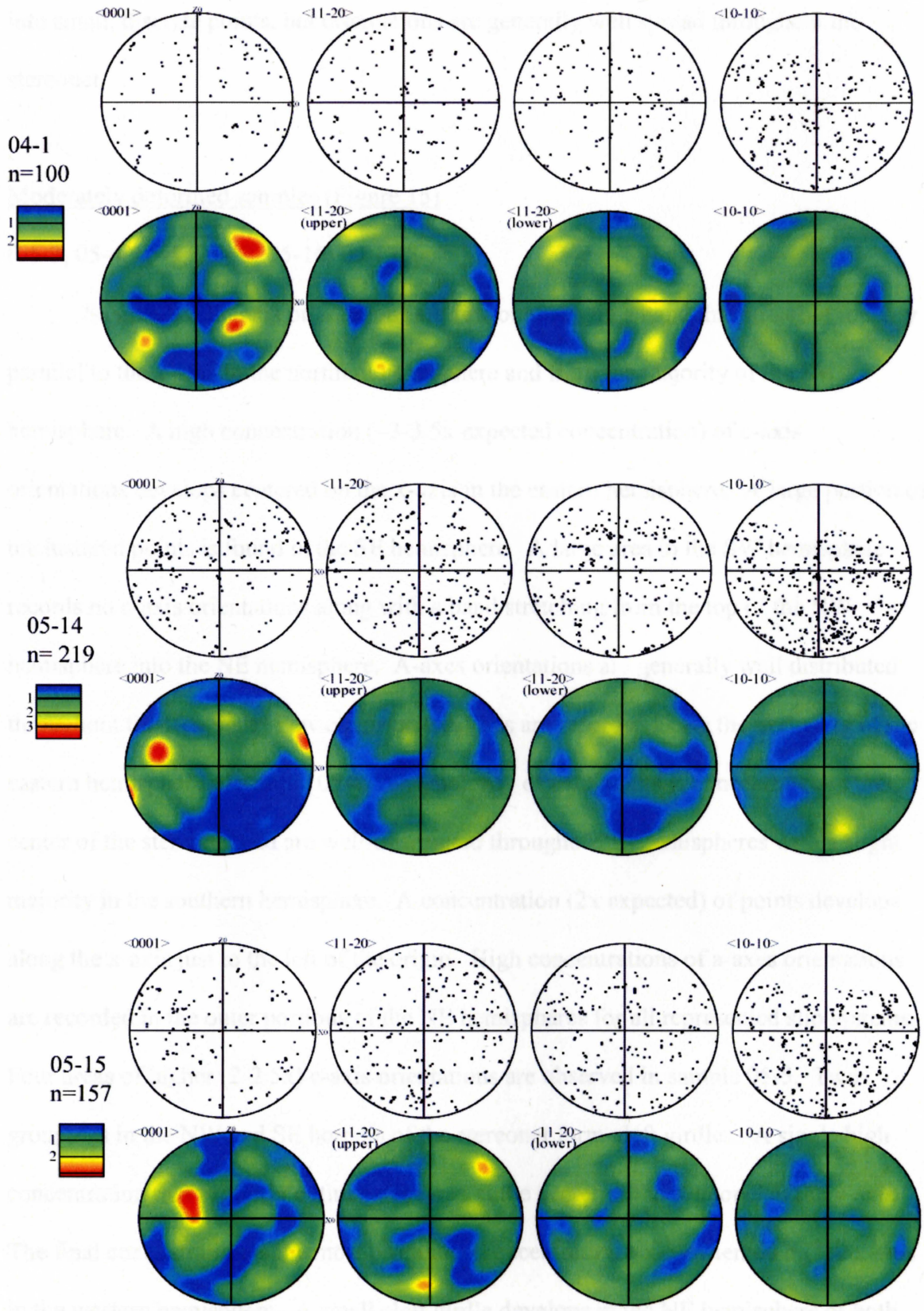

Figure 14: Undeformed/ Poorly deformed quartz LPO data. Contour on the right, n= number of data pts.

into small, discrete points, but orientations are generally well spread throughout the stereonet.

Moderately deformed samples (Figure 15)

(05-3, 05-4, 05-5, 05-12, 05-16, 05-17, 06-5)

Sample 05-3 c-axis orientations are few or absent in a band that stretches roughly parallel to the x-axis in the northern hemisphere and from the majority of the SW hemisphere. A high concentration (~3-3.5x expected concentration) of c-axis orientations develops centered on the x-axis in the eastern hemisphere. A large portion of unclustered points is found in the SE hemisphere. A large area in the SW hemisphere records no c-axis orientations along with a band stretching from the top of the NW hemisphere into the NE hemisphere. A-axes orientations are generally well distributed throughout the stereonet. Few c-axis orientations are recorded along the perimeter of the eastern hemisphere of sample 05-4. The majority of data points is concentrated in the center of the stereonet and are well-distributed throughout all hemispheres with a slight majority in the southern hemisphere. A concentration (2x expected) of points develops along the x-axis just to the left of the origin. High concentrations of a-axes orientations are recorded in the outer portions of the NE hemispheres for all represented slip systems. Four areas of higher (2-2.5x) c-axis orientations are observed in sample 05-5. Two groupings in the NW and SE borders of the stereonet form cleft girdles. A single high concentration that is poorly defined develops at the center of the stereonet at the y-axis. The final concentration is the most prominent concentration and is oriented on the x-axis in the western hemisphere. A small cleft girdle develops in the NE hemisphere of both

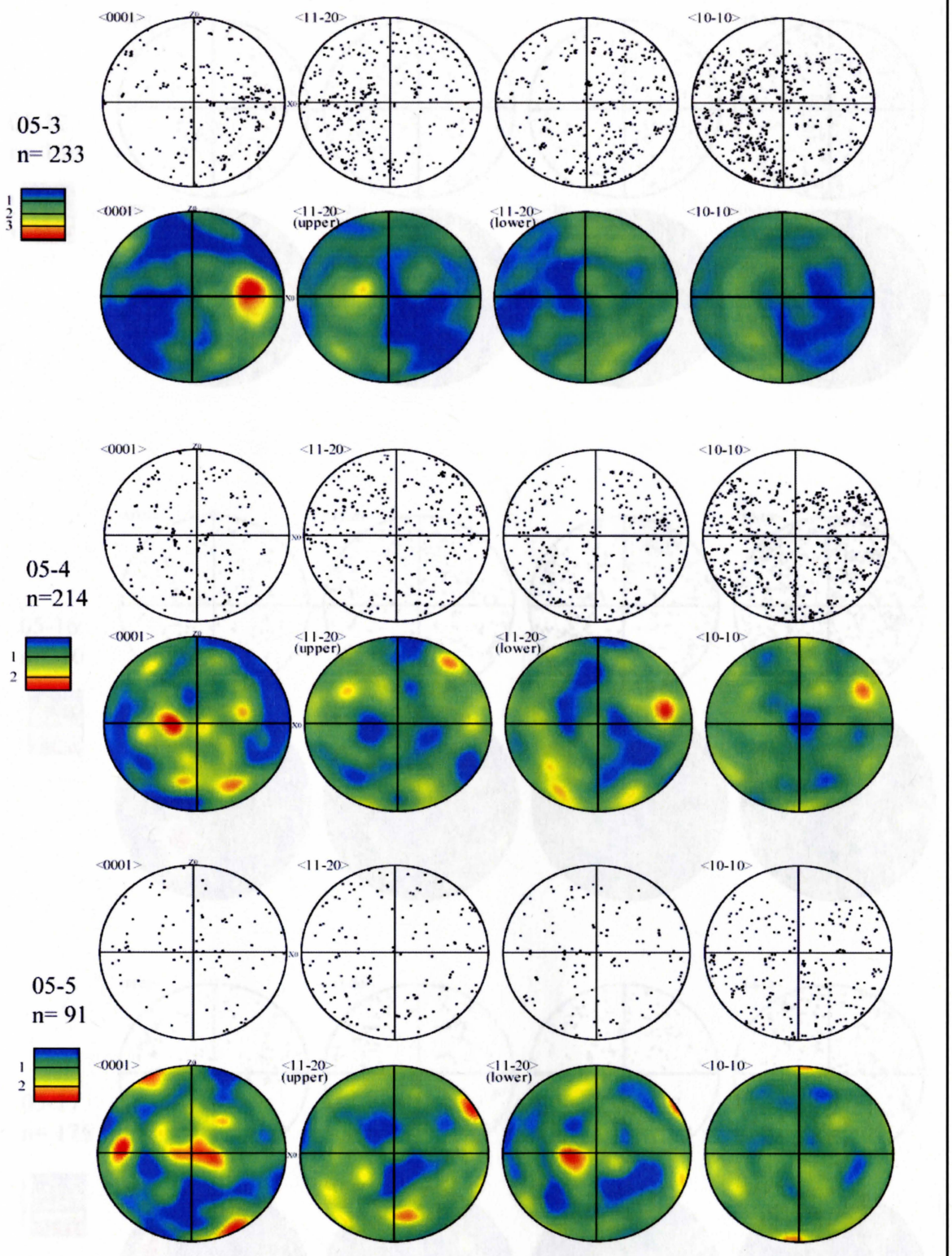

Figure continued

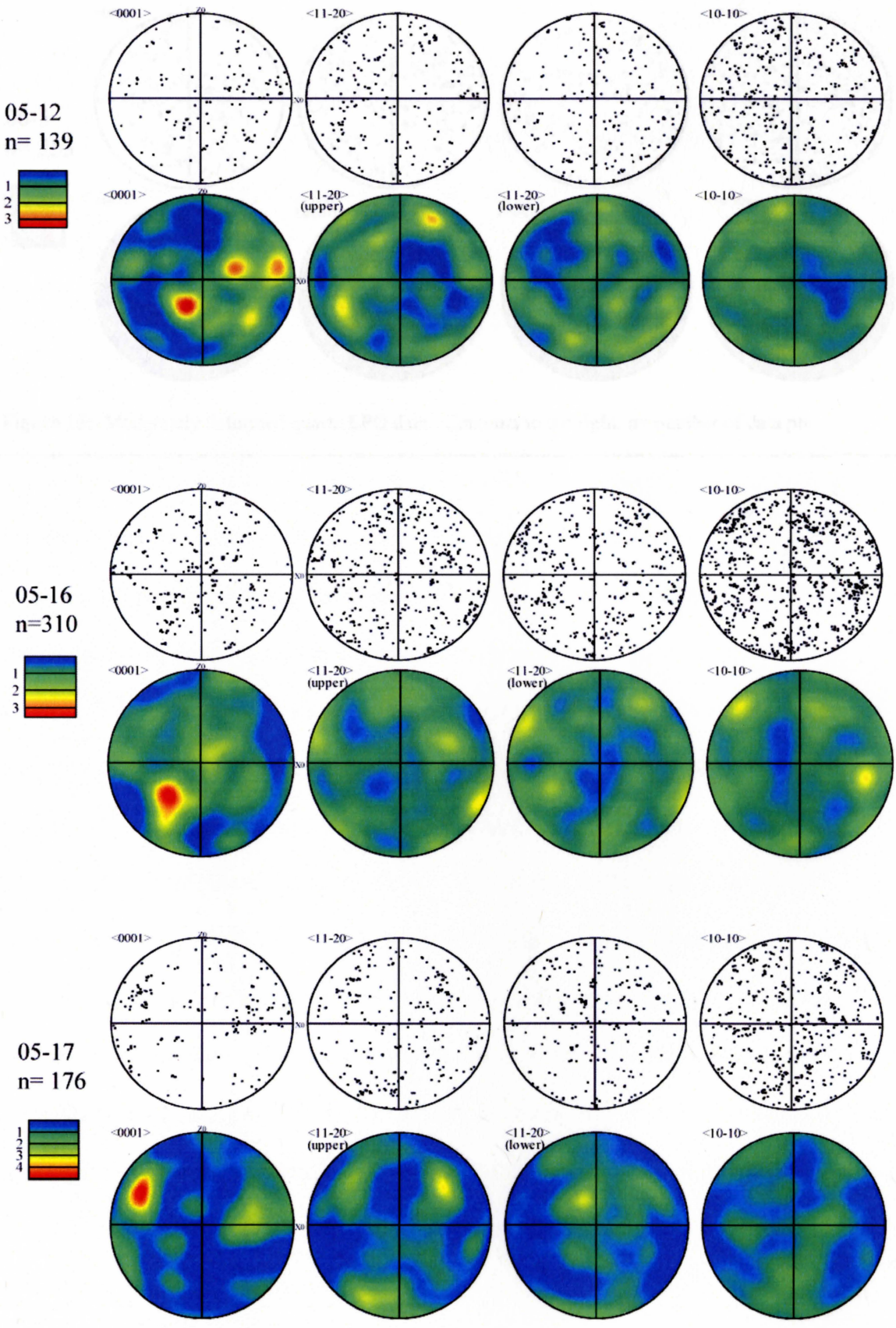

Figure continued

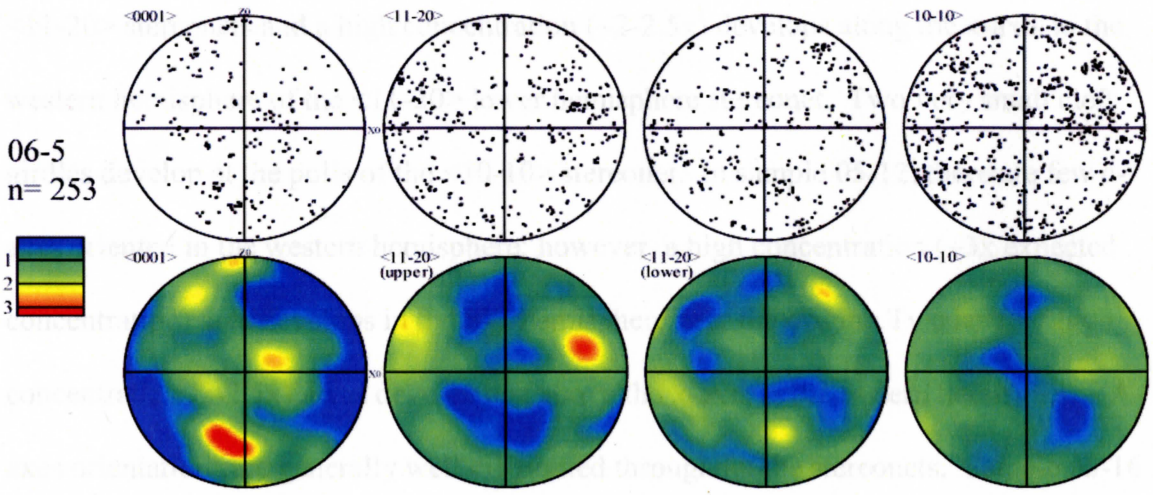

Figure 15: Moderately deformed quartz LPO data. Contours to the right, n= number of data pts.

<11-20> stereonets and a high concentration (~2-2.5x) develops along the x-axis in the western hemisphere of the <11-20> lower hemisphere stereonet. Two very small cleft girdles develop at the polls of the <10-10> stereonet. In sample 05-12, there are few c-axes oriented in the western hemisphere; however, a high concentration (~3x expected concentration) area develops in the SW hemisphere near the origin. Two smaller high concentration (2-2.5x) areas develop just above the x-axis in the eastern hemisphere. A-axes orientations are generally well distributed throughout the stereonets. Sample 05-16 c-axis orientations are evenly distributed throughout the stereonet with a high concentration region (~2.5-3x expected concentration) in the western hemisphere oriented along the x-axis. A-axes orientations are well distributed throughout the stereonets; however, two small high concentration (~2x) develop in the outer NE hemisphere and along the z-axis in the southern hemisphere. A distinct high concentration region (4-4.5x expected concentration) of quartz c-axis orientations develops in the NW hemisphere of sample 05-17. A second poorly defined high concentratrion region develops along the x-axis in the eastern hemisphere and grades downward in point concentration to the NE. The region between these two concentration-highs is below (<1x) expected concentration of random grain orientations. Although there are no distinct regions of high concentrations of a-axes, they are not evenly distributed throughout the stereonets, forming randomly spaced regions of low concentration. In sample 06-5, a concentration high (3x) of c-axis orientations develops along the z-axis in the southern hemisphere and a large proportion of grains are clustered in the NW hemisphere. A-axes concentrations are poorly concentrated along the outer boundaries of the stereonet along the x-axis.

Well-deformed samples (Figure 16)

(05-7, 05-8, 05-9, 06-2)

Sample 05-8 scatter plots indicate an arc-shaped region of high concentration stretching from the x-axis in the western hemisphere, up through the NW and NE hemisphere, and terminating on the stereonet boundary in the SE hemisphere. Very few c-axis orientations are located outside this arc in the SE and SW hemispheres. Contoured diagrams indicate two cleft girdles (2.5-3x expected concentration) in the NW and SE hemispheres. A second high concentration of c-axis orientations develops in the NE quadrant just above the x-axis. A third, smaller high develops in the SE quadrant just below the x-axis, but these points are very closely grouped, almost overlapping. A-axes diagrams reflect a relatively random distribution of orientations except for a line of higher concentration along the z-axis in upper hemisphere <11-20> and in the outer NE hemisphere of lower hemisphere <11-20>. In sample 05-8, a distinct c-axis concentration high (~4x expected concentration) develops on the z-axis in the northern hemisphere. Orientations are randomly scattered throughout the rest of the stereonet with almost no orientations recorded where the cleft girdles of sample 05-8 develop. A-axes orientations develop into no distinct high concentration area, though there are portions that have very low concentrations. Sample 06-2 develops a distinct high concentration (2-2.5x expected concentration) region of quartz c-axis orientations at the center of the stereonet along the y-axis. The remainder of grain orientations are evenly distributed throughout the stereonet with the exception of bands of low concentration in the centers of the NE, SE, and SW hemispheres, all in similar positions with respect to their individual hemisphere. A-axes data reflects a even distribution of orientations throughout

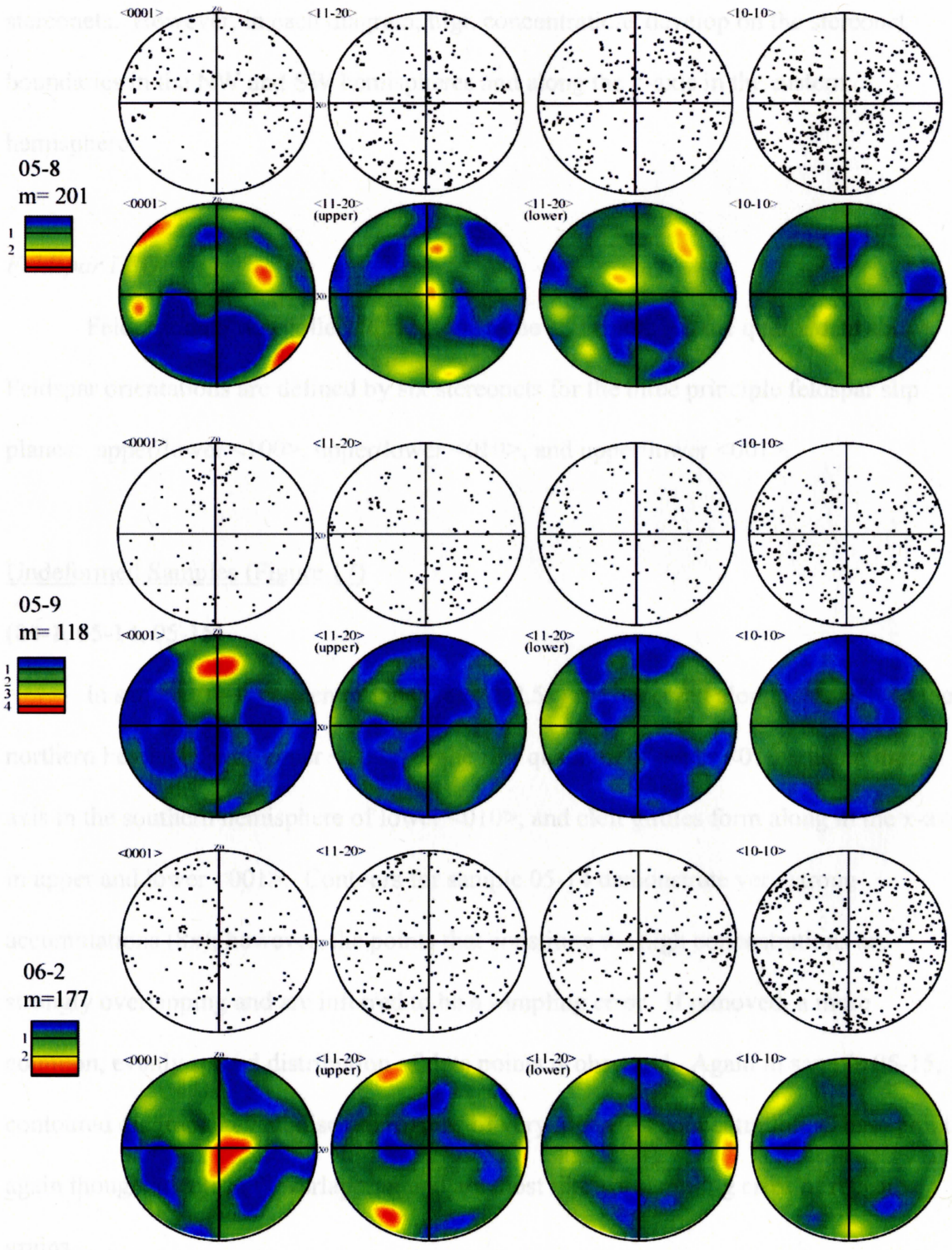

Figure 16: Well deformed quartz LPO data. Contours to the right, n= number of data pts.the center of

stereonets. However, in each diagram, high concentrations develop on the stereonet boundaries in the NW and SW hemispheres and along the x-axis in the eastern hemisphere.

Feldspar LPO

Feldspar data was collected from the same 13 samples as the quartz data above. Feldspar orientations are defined by six stereonets for the three principle feldspar slip planes: upper/lower <100>, upper/lower <010>, and upper/lower <001>.

Undeformed Samples (Figure 17)

(04-1, 05-14, 05-15)

In sample 04-1, concentrations highs(2-2.5x) are observed along the z-axis in the northern hemisphere of upper <100>, in the SW quadrant of upper <010>, along the z-axis in the southern hemisphere of lower <010>, and cleft girdles form along in the x-axis in upper and lower <001>. Contours for sample 05-14 demonstrate very strong accumulations (8x); however, the points that constitute the high concentrations are strongly overlapping and are inferred to be a sampling error. If removed, a more common, evenly spread distribution of data points is observed. Again in sample 05-15, contoured diagrams reveal discrete regions of very high (6x) concentration. These points again though are closely overlapping and are most likely a sampling error of repeated grains.

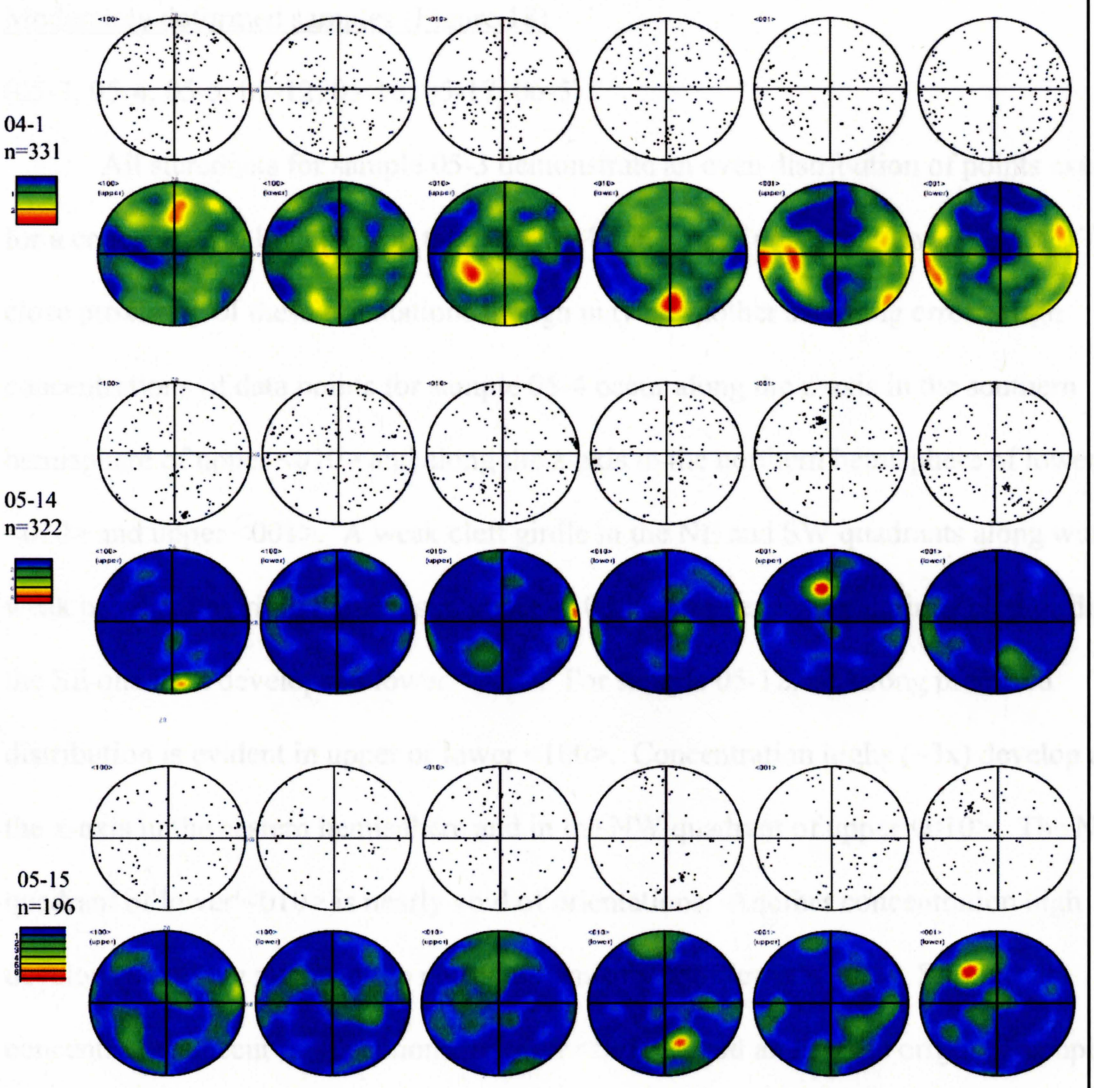

Figure 17: Undeformed feldspar LPO data. Contours to the right, n= number of data pts.

Moderately deformed samples (Figure 18)

(05-3, 05-4, 05-5, 05-12, 05-16, 05-17, 06-5)

All stereonets for sample 05-3 demonstrate an even distribution of points except for a concentration high (4x) on the outer SE boundary of upper and lower <010>. The close proximity of these orientations though may be another sampling error. High concentrations of data points for sample 05-4 occur along the z-axis in the southern hemisphere of upper <010> and along the z-axis in the northern hemisphere of lower <010> and upper <001>. A weak cleft girdle in the NE and SW quadrants along with a weak peak at the origin develops in upper <100>. Another poorly defined cleft girdle in the SE quadrant develops in lower <100>. For sample 05-12, no strong preferred distribution is evident in upper or lower <100>. Concentration highs (~3x) develop along the x-axis in the eastern hemisphere and in the NW quadrant of upper <010>. The NE quadrant of lower <010> is nearly void of orientations. Another concentration high develops along the z-axis in the northern hemisphere of lower <001>. Strongest concentrations occur in 4 locations in lower <001> at and around the origin of sample 05-16. Lower <010> has few orientations in the NE hemisphere while upper <010> has few orientations in the NE and SE hemisphere. Orientations in upper <001> are divided between the upper and lower hemisphere and distributed around the z-axis. Sample 05-17 develops concentration highs (2.5x) along the x-axis in the eastern hemisphere of lower <100>, along the x-axis in the western hemisphere of lower upper <010> and <001>, at the origin and in the NE quadrant of lower <010>, and along the z-axis in the souther hemisphere of lower <001>. A low concentration area surround the origin of lower <010>. Orientations are roughly evenly distributed throughout upper <100>. 06-5

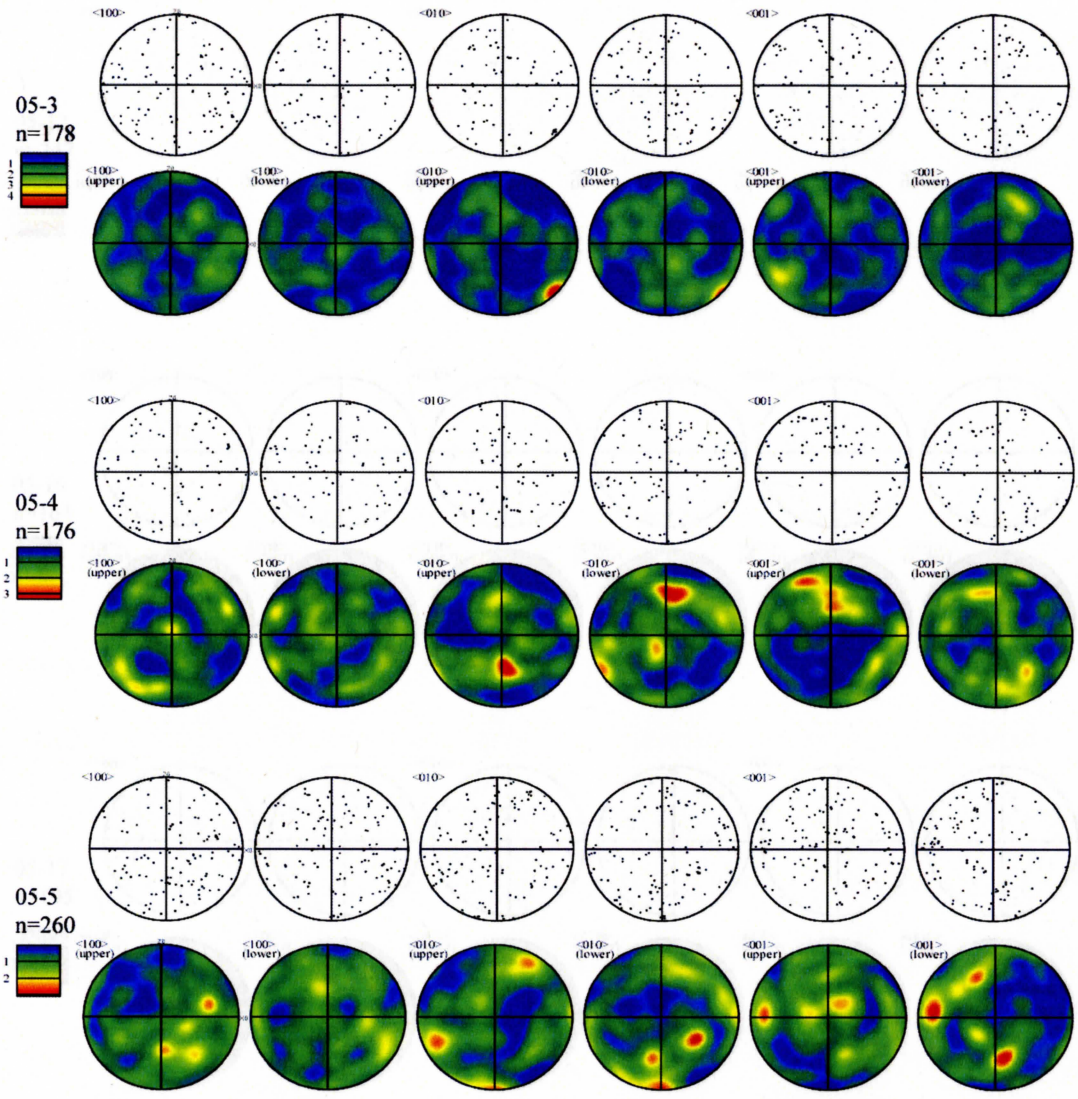

Figure continued

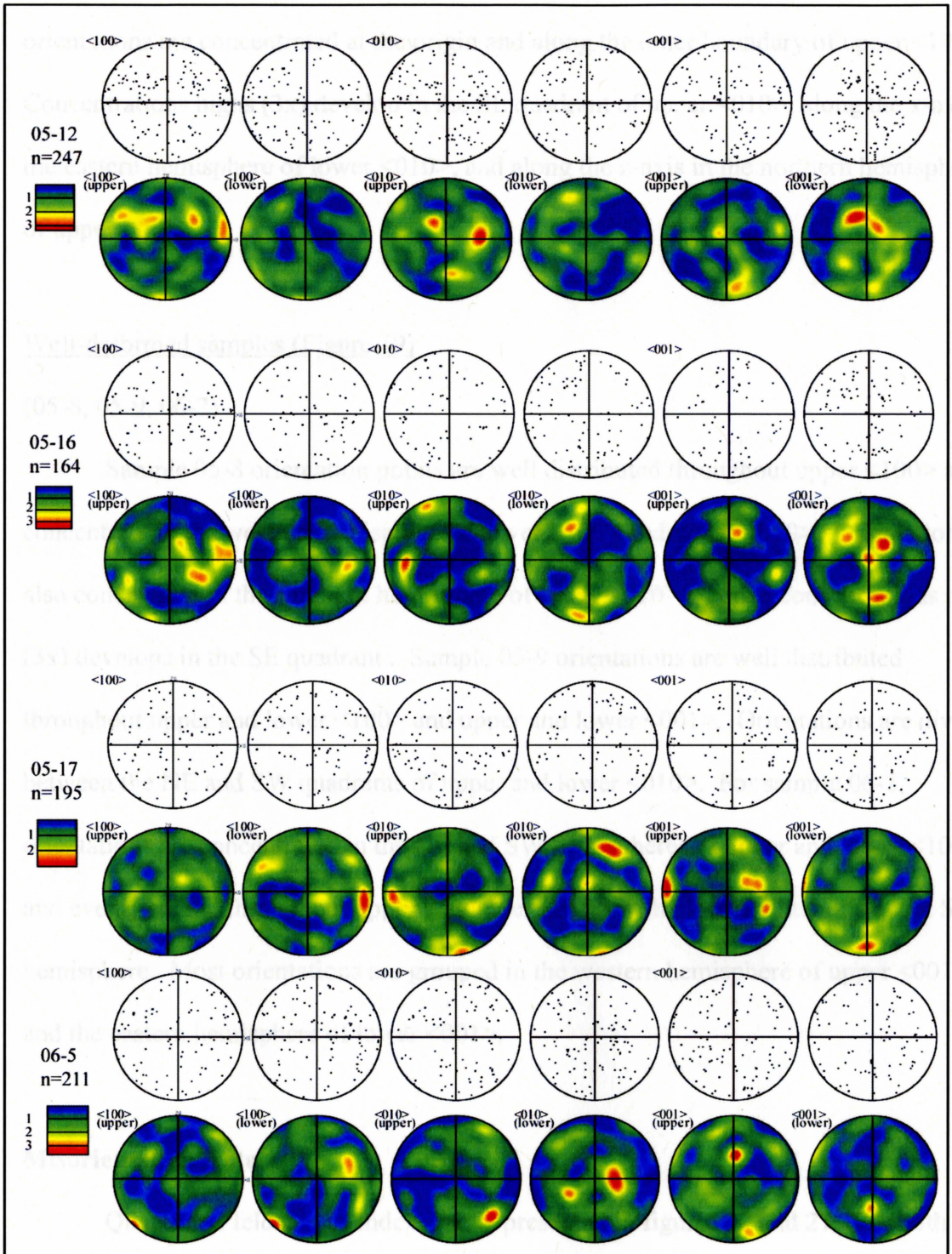

Figure 18: Moderately deformed feldspar LPO data. Contours to the right, n= number of data pts.

orientations are concentrated at the origin and along the outer boundary of upper <100>. Concentrations highs (3x) develop in the SE quadrant of upper <010>, along the x-axis in the eastern hemisphere of lower <010>, and along the z-axis in the northern hemisphere of upper <001>.

Well-deformed samples (Figure 19)

(05-8, 05-9, 06-2)

Sample 05-8 orientation points are well distributed throughout upper <100> and concentrate in the western hemisphere of lower <100> and upper <010>. Orientations also concentrate in the southern hemisphere of lower <010> where a concentrations peak (3x) develops in the SE quadrant . Sample 05-9 orientations are well distributed throughout upper and lower <100> and upper and lower <001>. Orientations are divided between the NE and SW quadrants of upper and lower <010>. For sample 06-2, orientations are concentrated in the NE and SW hemispheres of upper and lower <100> and evenly spread throughout upper and lower <010> with more orientations in the SE hemisphere. Most orientations are grouped in the western hemisphere of upper <001> and the eastern hemisphere of lower <001>.

Misorientation Data

Quartz and feldspar m-index data is presented in figures 20 and 21. For both quartz and feldspar grains, m-indices reveal a very low degree of deformation. Quartz m-indices range from 0.032 (05-16) to 0.077 (05-9), with no statistical significant difference between undeformed, moderately deformed, and well deformed samples. Feldspar m-indices reveal similar data, ranging from 0.0249 (05-8) to 0.0516 (05-15) with no

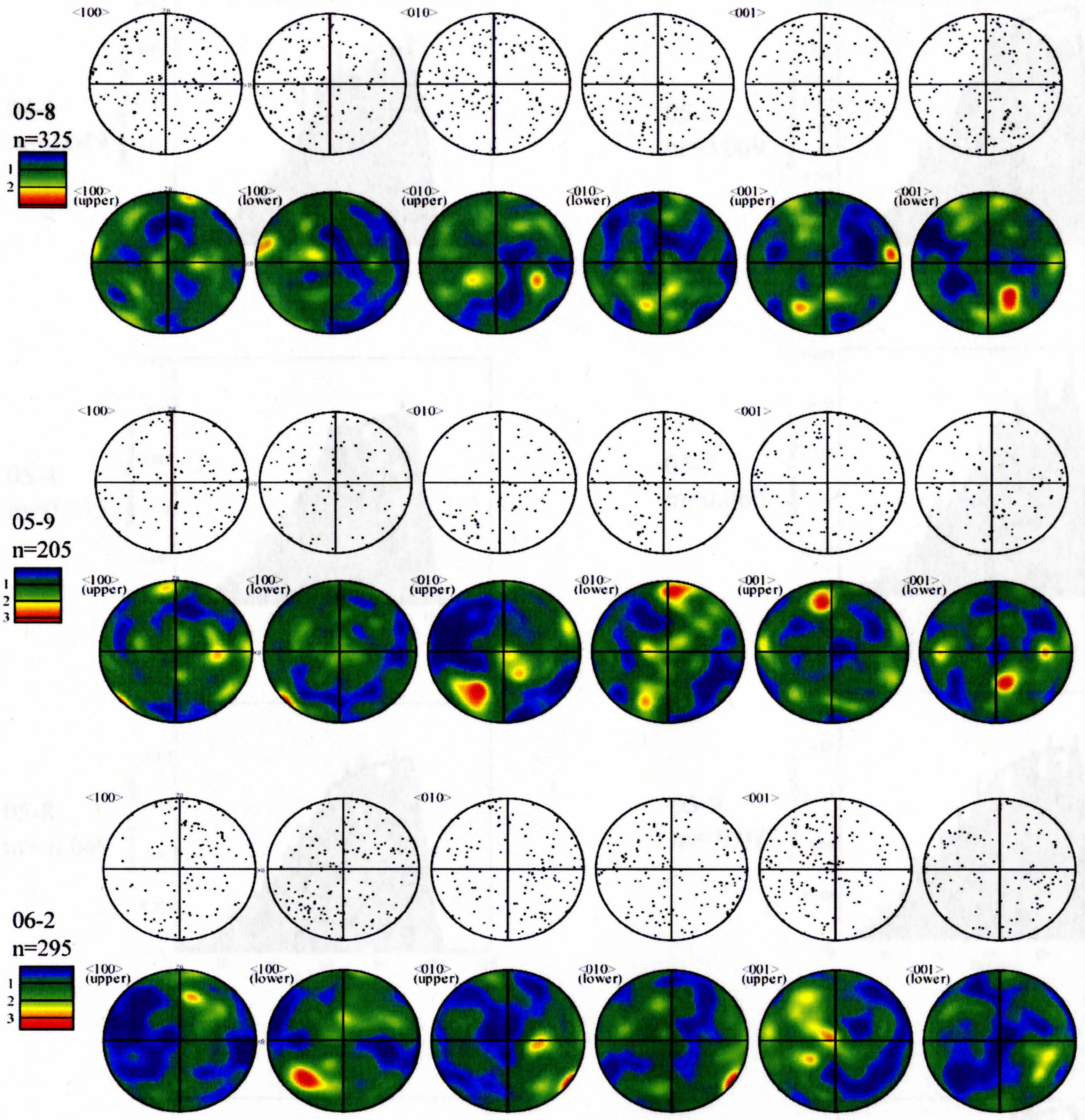

Figure 19: Well deformed feldspar LPO data. Contours to the right, n= number of data pts.

04-1
m=0.049

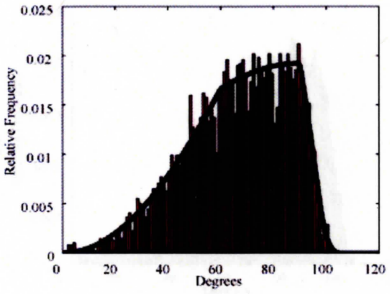

05-3
m=0.069

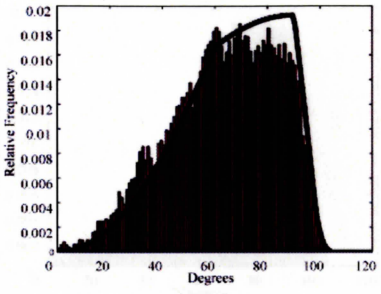

05-4
m=0.035

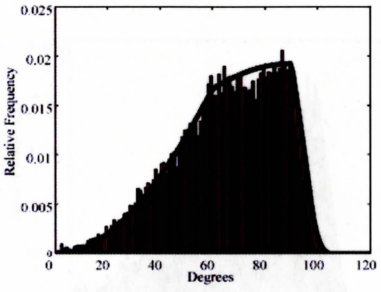

05-5
m=0.060

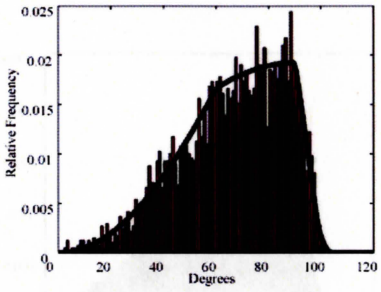

05-8
m= 0.049

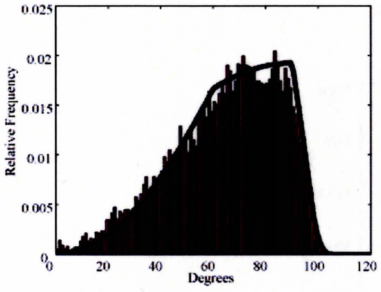

05-9
m= 0.077

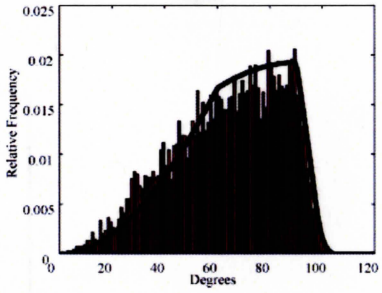

05-12
m=0.045

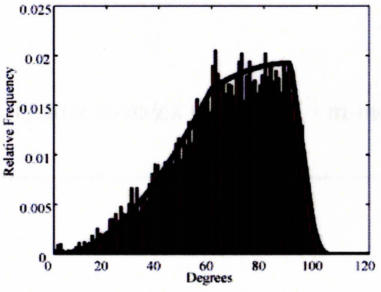

05-14
m= 0.045

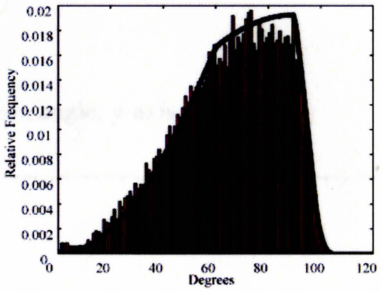

Figure continued

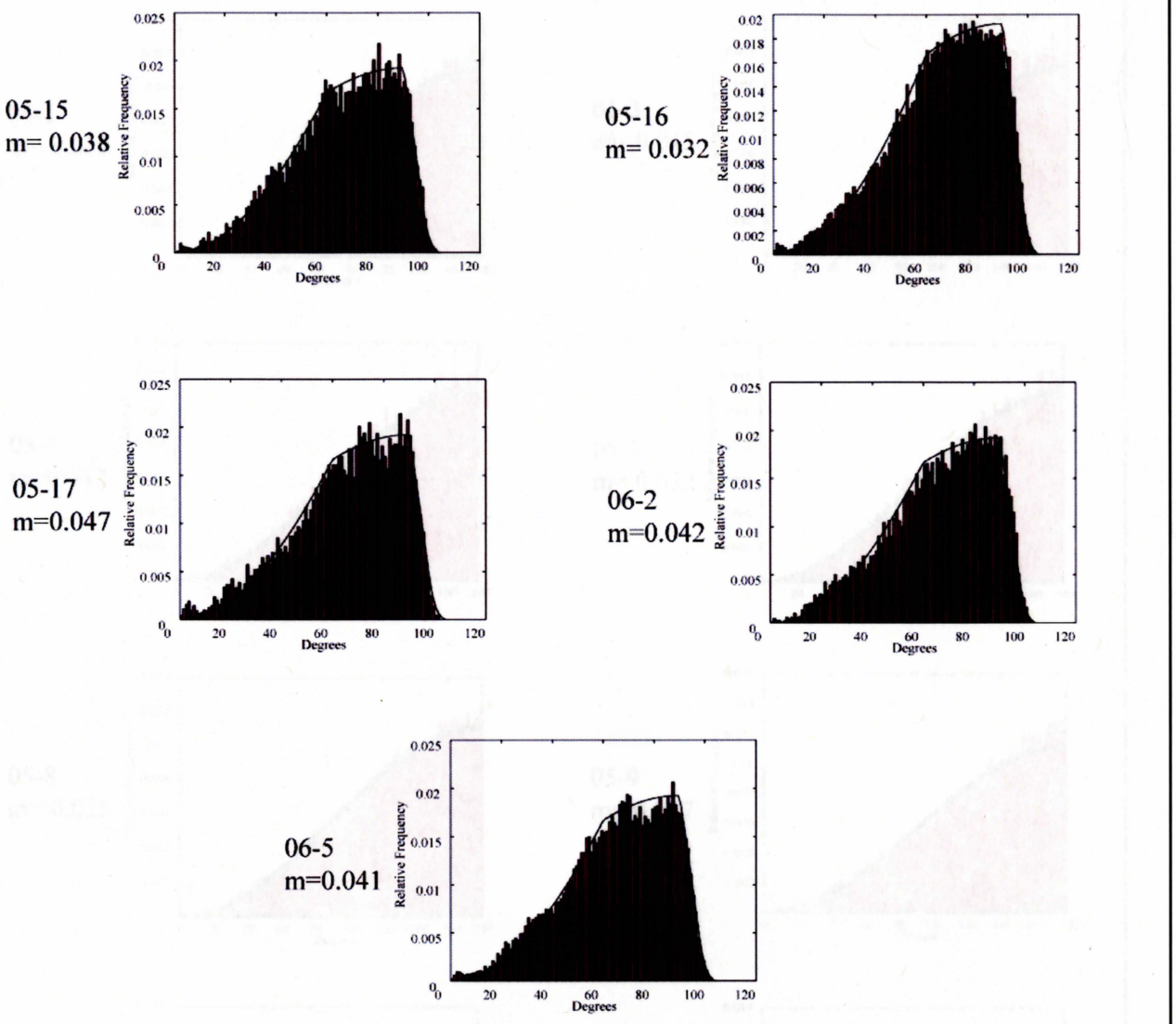

Figure 20: Quartz m-index results. M= m-index. X-axis is misorientation angle, y-axis is frequency distribution.

04-1
m= 0.030

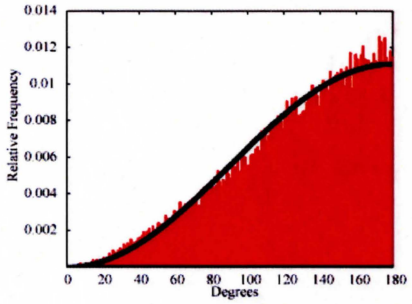

05-3
m= 0.045

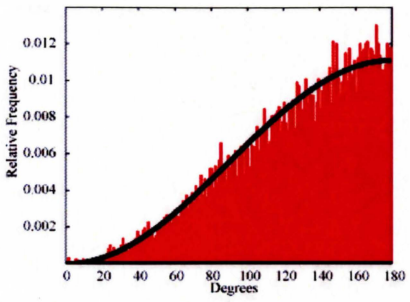

05-4
m=0.042

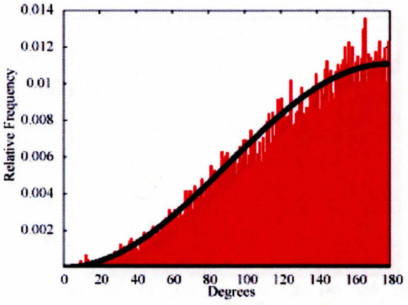

05-5
m= 0.032

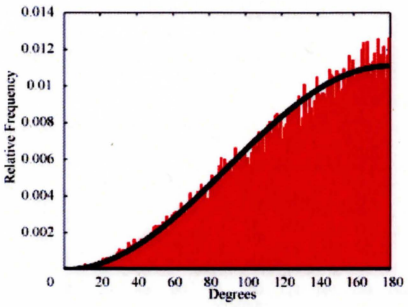

05-8
m= 0.025

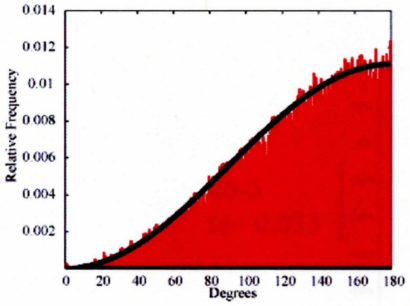

05-9
m= 0.047

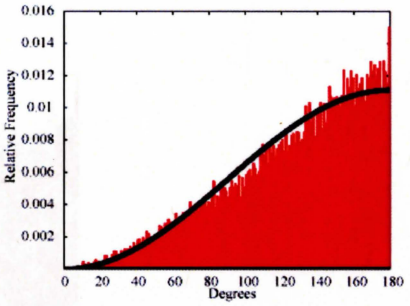

05-12
m= 0.039

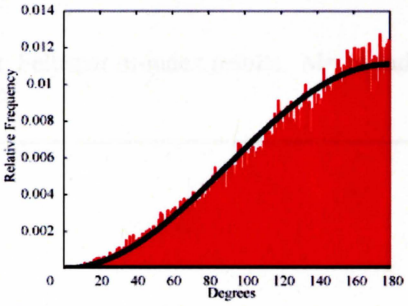

05-14
m= 0.036

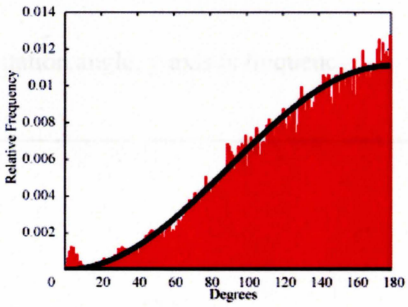

Figure continued

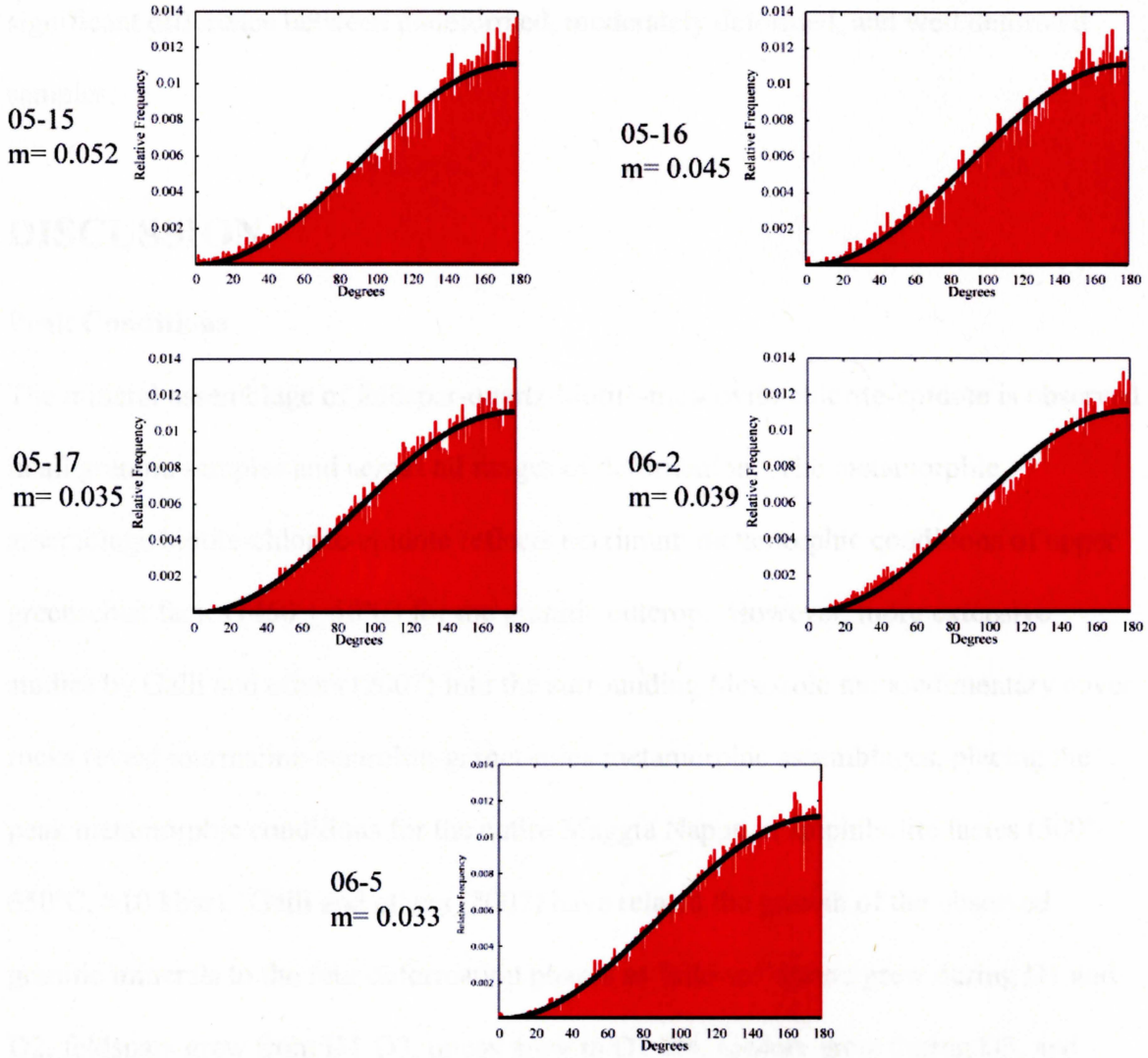

Figure 21: Feldspar m-index results. M= m-index, x-axis is misorientation angle, y-axis is frequency distribution.

significant difference between undeformed, moderately deformed, and well deformed samples.

DISCUSSION

Peak Conditions

The mineral assemblage of feldspar-quartz-biotite-muscovite-chlorite-epidote is observed in all granitic samples and across all ranges of deformation. The metamorphic assemblage biotite-chlorite-epidote reflects maximum metamorphic conditions of upper greenschist facies (450 $\pm$ 50°C) for the granitic outcrop. However, more extensive studies by Galli and others (2007) into the surrounding Mesozoic metasedimentary cover rocks reveal tourmaline-staurolite-garnet-mica metamorphic assemblages, placing the peak metamorphic conditions for the entire Maggia Nappe in amphibolite facies (500°-650°C, >10 kbar). Galli and others (2007) have related the growth of the observed granitic minerals to the four deformation phases as follows: quartz grew during D1 and D2, feldspars grew from D1-D3, micas grew in D1-D4, epidote grew during D3, and chlorite developed last during D4. The time relationship of epidote and chlorite growth is reflected in this dataset by the deformation of epidote porphyroblasts and the undeformed nature of chlorite grains.

Microstructures

A series of four microstructures and grain characteristics define the evolution of rock characteristics with increasing deformation:

Ribbon microstructures

Grain aggregate shape

Grain size and shape

Undulose extinction patterns

Ribbon Microstructures

Ribbon microstructures act as important tectonic deformation indicators throughout the outcrop and are effective in identifying highly strained samples based on their width and sinuosity. The development of ribbon microstructures is first evident in poorly deformed samples as crudely defined, poorly sorted elliptical VCG aggregates. No such deformed features are evident in undeformed sample 04-1. With increasing deformation, VCG quartzo-feldspathic aggregates deform into better-defined elliptical features in the xz-plane with their long axis subparallel to the x-axis such that they are stretching in the direction of maximum extension (S_1). After further deformation, the elliptical VCG aggregates thin and develop into long, consistent, narrow ribbons oriented parallel to extension in the xz-plane. The initiation of ribbon development can be observed in some samples in which narrow ribbons emerge like fingers from unstrained VCG aggregates extending parallel to extension. Ribbon thinning leads to progressive sorting until they are well sorted in the most deformed samples. Likewise, under more extensive deformation, the thinned ribbon microstructures become straighter and longer.

Ribbons do not appear in xy-plane oriented thin sections. Instead, only randomly shaped VCG and coarse grained aggregates are observed; thus, ribbon microstructures define another foliation plane in addition to strained biotite clots. Coarse grain ribbons that are only observed in the most extensively deformed samples define another foliation

plane based on grain size banding. A slight degree of deflection of ribbon microstructures is observed as ribbons migrate from a subparallel orientation to the extension direction in shear zone boundaries to parallel orientation with the extension direction in the centers of shear zones.

Grain Aggregate Shapes

As noted above, VCG quartzo-feldspathic aggregates along with coarse grain aggregates in the most deformed samples deform into oriented ribbon microstructures. As ribbons develop, VCG shape evolves from highly variable, anhedral through euhedral, and erratic to a more consistent blocky subhedral and gently lobate-anhedral shape. Likewise, only square or rectangular grains without point contacts define coarse grain ribbons.

Coarse-medium grain aggregates evolve from a poorly sorted, poorly defined amoeboid/highly interlobate fabric to a more homogenous medium-grained equigranular-interlobate fabric in which coarse grains are secluded to ribbon microstructures. With increasing deformation, grain size within aggregates becomes more homogenous until a granoblastic texture is developed.

Grain Size and Shape

With increasing deformation, the ratio of very coarse grains to coarse-medium grains decreases, representing a trend of grain size reduction. Medium-coarse grains become less anhedral and develop a more rounded or polygonal appearance, reflecting grain boundary area reduction (GBAR) and progressive reduction of the internal free

energy of the rock. The net decrease in grain size is caused by subgrain generation commonly observed in VCG aggregates or as bulges between adjacent grains. Grains in VCG aggregates and ribbons become more blocky and polygonal and demonstrate fewer bulging or subgrain relationships after further deformation.

Undulose Extinction Characteristics

Feldspars demonstrate a higher frequency of undulose extinction reflecting a greater degree of internal deformation than quartz grains. The radiating patterns of sweeping undulatory extinction are due to point contacts between grains where stress is focused on a single point instead of an entire plane. Deformation bands in quartz and feldspar grains reflect dislocation migration and the generation of subgrains. The absence of deformation bands in ribbon microstructures in higher deformation regimes suggest strain hardening of grains such that they are unable to recrystallize into subgrains. Likewise, grains within ribbons have polygonal contacts, reducing the total internal free energy of grains.

LPO Data and M-Index

The most striking characteristic of both quartz and plagioclase LPO data is the distinct lack of fabric despite the observed mylonitic texture of shear zones($\gamma \leq 14$). While no apparent fabric is observed in poorly and moderately deformed samples, EBSD reveals a weak fabric in the three well-deformed samples 05-8, 05-9, and 06-2. Samples 05-9 and 06-2 develop similar single-girdle c-axis pattern parallel to the y-axis. The high concentration of c-axis orientations of 05-9 are clustered above the origin along the z-

axis; however, this may be due to an error by cutting the thin section oblique to the xz-plane of the rock. If the thin section is rotated about the x-axis, a girdle develops along the y-axis as in sample 06-2. Development of a single girdle along the y-axis reflects principle prism <a> slip at medium grade temperatures (400°-500° C). The a-axes distributions of sample 06-2 into three cleft girdles at the boundary of the stereonet also reflect medium temperature, prism <a> slip. The cleft girdle in sample 05-8 with a concentration high near the origin reflects a transition between prism <a> slip and <c> slip at higher-grade temperatures (500°-650° C). While these three samples appear to have a weak fabric and other samples may demonstrate weak, random fabrics, m-index values are very low and suggest that observed fabrics are very weak, if at all present. The weakness of feldspar fabrics and equally low m-index values reinforces that lack of defined lattice-preferred orientations in all samples.

Magmatic Fabric

Previous research (e.g., Ramsay & Allison 1979, Simpson 1993, Galli et al. 2007) and field observations have identified a pervasive lineation in the granitic outcrop defined by both biotite blades and quartzo-feldspathic aggregates demonstrating shape-preferred orientations. Microstructural observations suggest little deformation in undeformed samples revealed by the lack of oriented or strained VCG quartzo-feldspathic or biotite aggregates. Rf/ϕ data has also demonstrated a mild shape-preferred orientation ($\gamma > 2$) to undeformed mafic enclaves which have mineral lineations parallel to lineations in surrounding granitic wall rock. The presence of a lineation without strong evidence for tectonic deformation suggests that the lineation is a magmatic fabric related to intrusion.

Paterson and others (1989) have demonstrated that lineations of minerals that do not have a shape-preferred orientation, such as quartz and feldspar, in the absence of tectonic deformation is a key attribute for identifying magmatic fabrics.

Deformation Mechanisms

Evidence for Dislocation Creep

Dislocation creep is often identified by evidence of dynamic recrystallization, recovery processes, and development of a strong LPO (e.g., Hirth & Tullis 1992, Wrightman et al. 2005). Dynamic recrystallization is evident through many of the microstructure and grain relationships. Progressive grain size reduction and grain boundary area reduction with increasing deformation suggest development of small (<100-250 μm) subgrains through grain boundary migration. Also, bulging grain boundaries at medium to high grade metamorphism suggest grain boundary migration.

Grain recovery is evident in the progression of extinction characteristics. Sweeping undulatory extinction in grains reflects a random distribution of dislocations within a grain or subgrain. Deformation bands, evident in quartz and feldspar grains, develop as dislocations preferentially migrate into concentrated regions, resulting in a kinked grain with zones separated by kinks exhibiting different extinction angles. Lastly, as dislocations migrate further into discrete lines, a subgrain, as described above, is formed. The new subgrain is typically initially unstrained, evident in medium grain quartz void of undulose extinction, but can become strained later and broken down further into smaller subgrains. The presence of undulatory extinction is also important in identifying that the observed deformation is tectonic and not magmatic.

The observation of grain boundary area reduction (GBAR) acts as strong evidence for grain boundary migration recrystallization. GBAR is a special type of grain boundary migration that results in grain growth and straightening of grain boundaries by the decrease in total surface area of a grain, reducing the total internal free energy (Passchier & Trouw 2005). Also, the presence of a bimodal grain size distribution suggests partial recrystallization of the outcrop through dislocation creep instead of complete recrystallization.

While microstructures suggest dislocation creep, LPO data does not. Hirth and Tullis (1992) and Bestman and Prior (2003) among others have demonstrated that dislocation creep leads to strong crystallographic fabrics and lattice-preferred orientations, traits noticeably absent from this dataset. If a weak fabric exists in samples 05-8, 05-9, and 06-2, it suggests deformation by dislocation creep-accommodated dynamic recrystallization. However, experimental and field data demonstrates that rocks deformed by dislocation creep alone develop very strong fabrics and have high frequencies of low misorientation angles (<40°), characteristics not observed by 05-8, 05-9, or 06-2.

Evidence for Diffusion Creep and Grain-Boundary Sliding (GBS)

The absence of strong LPOs in highly strained rocks ($\gamma > 4$) is often attributed to diffusion creep (e.g. Wrightman et al. 2005, Bestmann & Prior 2003). However, diffusion creep is a strongly grain sensitive mechanism. While the observed grain size reduction during dislocation creep may lead to onset of diffusion creep, observed grain sizes in the studied rocks are too large at the given deformation conditions (450°-650° C,

3-10 kbar, Galli et al. 2007) for diffusion creep to dominate. With a minimum grain size of 100 μm, which does not encompass the majority of samples, and a tectonic strain rate of 10^{-13} s^{-1}, the dominant deformation mechanism would be on the boundary between diffusion and dislocation creep. Increasing grain size would suggest dislocation creep is the dominant deformation mechanism.

In situations where diffusion creep is the predicted deformation mechanism but grain size is too large, diffusion creep-accommodated GBS has been proposed as a system that can effectively increase the range of conditions in which diffusion creep takes place (e.g. Wrightman et al. 2005). While diffusion creep microstructures are rare in experimental and field data, GBS is strongly evident in this dataset's microstructures. With increasing deformation, grain boundaries flatten through dislocation creep-induced GBAR, providing sliding plains for mobile grains. Monomineralic aggregates also become less common and medium grain aggregates are more thoroughly mixed with increasing deformation, suggesting GBS-induced mixing of feldspar and quartz grains (e.g. Tullis et al. 1990, Fliervoet et al. 1997, Brodie 1998b).

Evidence for Static Recrystallization and Grain Growth

Post deformational recrystallization and grain growth may also have taken place after diffusion processes ended at much smaller grain sizes than those observed. Static recrystallization was commonly believed to weaken developed LPOs; however, over geologic timescales the LPO weakening effects of static recrystallization are not strong enough to significantly weaken LPOs, let alone destroy a strong dislocation creep-induced LPO (Heilbronner & Tullis 2002, Otani & Wallis 2006).

Grain growth has also been shown to neither destroy nor enhance crystallographic fabrics (Tullis & Yund 1982, Gapais & Barbarin 1986). Tullis and Yund (1982) calculate that at 600°C and 3 kbar, 100 μm grains can grow to a size of 2.3 mm over 10 million years. Grain growth also demonstrates a logarithmic increase in rate with decreasing size (Tullis & Yund 1982); thus, original grain sizes of 10-20 μm certainly could have grown since the middle Tertiary to the observed grain sizes.

Static recrystallization and grain growth may explain why undulose extinction is observed in many medium-grain aggregates. If a short period of dislocation creep deformation proceeded diffusion creep, the weak developed fabric would have been destroyed by dynamic recrystallization. If dislocation creep did not follow diffusion creep, grain growth may have been syn-tectonic where low differential stresses were sufficient to internally deform grains.

It is important to point out that evidence for grain growth and static recrystallization is not fully conclusive. These processes are only used here in an attempt to explain discrepancies between the assumption that diffusion creep destroyed well-developed LPOs and the observation that grain size is generally too large for diffusion creep to act as the dominant deformation mechanism given the deformation conditions.

CONCLUSIONS

Structural development of the Maggia Nappe was accommodated by crystal-plastic deformation in discrete, highly deformed shear zones ($\gamma \leq 14$) cutting both granitic intrusive rocks and metamorphosed cover sediments at P/T conditions of 450°-650° C and 3-10 kbar (Galli et al. 2007). Microstructural and crystallographic fabric observations on

sheared and unsheared samples reflect evidence of conflicting dominant deformation mechanisms. The following progression of deformation mechanisms in the Maggia Nappe is proposed in order to account for conflicting deformation mechanisms. Development of a lineated magmatic fabric during Matorello intrusion (300 Ma) as evidenced by lineations of minerals without shape-preferred orientations and initial preferred orientations of elliptical mafic enclaves

1. Initiation of shear zones during D1 phase deformation accommodated by dislocation creep through prism <a> and <c> slip at temperatures of 450°-570°$\pm$ 50° C. Development of a strong LPO and high frequency of low (<40°) misorientation angles through dislocation creep-accommodated dynamic recrystallization. Grain size reduction and GBAR by subgrain development through grain boundary migration with increasing temperature and pressure into D2 phase deformation.
2. Onset of diffusion creep-accommodated GBS after sufficient grain size reduction and increased temperature in D2, D3, and D4 phases of deformation and subsequent destruction of LPO.
3. Mixing of mineralogies in grain aggregates by progressive GBS and strain hardening in coarse grain ribbon microstructures.
4. Syn- and post-deformational static recrystallization and/or grain growth of fine grain quartz and feldspar, resulting in slightly deformed medium-coarse grain aggregates.

Similar conclusions have been reached by Wrightman and others (2006) in the Southern Alps regarding post deformational grain growth and destruction of LPOs

through GBS and Bestmann and Prior (2003) in the laboratory with regard to destruction of LPOs by diffusion creep-accommodated GBS.

ACKNOWLEDGEMENTS

I would like to acknowledge the Washington & Lee University Geology department for funding through the Kozack, McGuire, Spencer, Scwab Research Grant, for ample office space, and a friendly, quiet place to work. Also, I acknowledge the Keck Geology Consortium, Mark Brandon, and John Garver for their help in the field and hospitality at Yale University and Smith College. I thank Yale University, their lab, and Zhenting Jiang for aid in acquiring LPO and misorientation data. A great amount of gratitude is owed to Kat Compton for her help in the field and comments made on some of my thesis material. Very much thanks is also owed to Lisa Greer for her many hours of calming and distracting conversation, from the early afternoon until the late night.

Most of all, I would like to acknowledge and thank Jeff Rahl for his guidance, patience, dancing abilities, and perpetually enthusiastic attitude throughout this process. Without his help, I would still be sitting on a rock in Switzerland scratching my head.

REFERENCES

Bestmann, M., Prior, D. J. (2003) Intragranular dynamic recrystallization in naturally deformed calcite marble: diffusion accommodated grain boundary sliding as a result of subgrain rotation recrystallization. *J Stuct Geol.* 25: 1597-1613.

Brandon, M. T. (1996) CONVAXES PROGRAM v. 1.1. Unpublished program. Yale University.

Brodie, K. H. (1989b) Retrogressive mylonitic metabasic fault rocks. In: Snoke A., Tullis J., Todd V. R. (eds) Fault related rocks- a photographic atlas. Princeton University Press, New Jersey, 402-403.

Davis, G. H., Reynolds, S. J. (1996) Structural Geology of Rocks and Regions. 2nd Edition Text. John Wiley and Sons Inc.

Dunlap, W. J., Hirth, G., Teyssier C. (1997) Thermomechanical evolution of a ductile complex. *Tectonics.* 16: 983-1000.

Etheridge, M. A., Wilkie, J. C. (1979) Grainsize reduction, grain boundary sliding, and the flow strength of mylonites. *Tectonophysics.* 58: 159-178.

Favre, P., Stampfli, G. M. (1992) From rifting to passive margin: the examples of the Red Sea, Central Atlantic and Alpine Tethys. *Tectonophysics.* 215: 69-97.

Fliervoet, T. F., White, S.H., Drury M. R. (1997) Evidence for dominant grain-boundary sliding deformation in greenschist- and amphibolite-grade polymineralic ultramylonites from the Redbank Deformed Zone, Central Australia. *J Struct Geol.* 19: 1495-1520.

Fliervoet, T. F., Drury, M. R., Chopra, P. N. (1999) Crystallographic preferred orientations and misorientations in some olivine rocks deformed by diffusion or dislocation creep. *Tectonophysics.* 303: 1-27.

Galli, A., Mancktelow, N., Reusser, E., Caddick, M. (2007) Structural geology and petrography of the Naret region (northern Valle Maggia, N. Ticino, Switzerland). *Swiss Journal of Geosciences.* 100: 53-70.

Gifkins, R. C. (1976) Grain boundary sliding and its accommodation during creep and superplasticity. *Metall Trans A.* 7A: 1225-1232. As reported in Passchier & Trouw (2005) *Microtectonics.*

Grujic, D., Mancktelow, N. (1996) Structures of the northern Maggia and Ledendun Nappes, Central Alps, Switzerland. *Eclogae geol. Helvetica.* 89: 461-504.

Heilbronner, R., Tullis, J. (2002) The effect of static annealing on microstructures and crystallographic preferred orientations of quartzites experimentally deformed in axial compression and shear. In: De Meer, S., Drury, M. D., de Bresser, J. H. P. (eds) Deformation mechanisms, rheology, and tectonics: current status and future perspectives. Special Publication 200, *GSL.* 191-218.

Hirth, G., Tullis, J. (1992) Dislocation creep regimes in quartz aggregates. *J Struct Geol.* 14:145-149.

Ji, S., Wirth, R., Rybacki, E., Jiang, Z. (2000) High temperature plastic deformation of quartz-plagioclase multilayers by layer-normal compression. *Journal of Geophysical Research.* 105: 16,651-16,664.

Knipe, R. J. (1989) Deformation mechanisms- recognition from natural tectonites. *J Struct Geol.* 11: 127-146.

Langdon, T. (1995) The characteristics of super-plastic flow in ceramics. *as reported in* Passchier & Trouw 2005.

Langdon, T. G. and Vastava, R. B. (1982) An evaluation of deformation models for grain boundary sliding. In *Mechanical Testing for Deformation Model Development,* eds R. W. Rohde and J. C. Swearengen, pp. 435-451. American Society for Testing materials, Philadelphia.

Law, R. D. (1990) Crystallographic fabrics: a selective review of their applications to research in structural geology. In: Knipe, R.J., Rutter, E. H. (eds) Deformation mechanisms, rheology, and tectonics. *Geol. Soc. Spec. Publ.* 54: 335-352.

Manatschal, G., Bernoulli, D. (1998) Rifting and early evolution of ancient ocean basins: the record of the Mesozoic Tehtys and of the Galicia-Newfoundland margins. *Marine Geophysical Researchers.* 20: 371-381.

Maxelon, M., Mancktelow, N. S. (2005) Three-dimensional geometry and tectonostratigraphy of the Pennine zone, Central Alps, Switzerland and Northern Italy. *Earth Science Reviews.* 71: 171-227.

Milnes, A. 1974b: Structure of the Pennine Zone (Central Alps): a new working hypothesis. *Bulletin of the Geological Society of America.* 85: 1727–1732.

Mohanty, S., Ramsay, J. G. (1994) Strain partitioning in ductile shear zones: an example from a Lower Pennine nappe of Switzerland. *J Struct Geol.* 16: 663-676.

Moore, A. C. (1970) Descriptive terminology for the tectures of rocks in granulite facies terrains. *Lithos.* 3: 123-127.

Nishikawa O., Takeshita, T. (1999) Dynamic analysis and two types of kink bands in quartz veins deformed under subgreenschist conditions. *Tectonophysics.* 301: 21-34.

Otani, M., Wallis S. (2006) Quartz lattice preferred orientation patterns and static recrystallization: Natural examples from the Ryoke belt, Japan. *Geology.* 34: 561-564.

Passchier, C. W., Trouw, R. A. J. (2005) Microtectonics. 2nd Edition Text. Springer.

Patterson, S. R., Vernon, R. H., Tobisch, O. T. (1989) A review of criteria for the identification of magmatic and tectonic foliations in graintoids. *J Struc Geol.* 11: 349-363.

Poirier, J.P. (1985) Creep of crystals: high-temperature deformation processes in metals, ceramics, and minerals. Cambridge Univ Press, Cambridge.

Prior, D. J., Boyle, A. P., Brenker, F., Cheadle, M. C., Day, A., Lopez, G., Peruzzo, L., Potts, G. J., Reddy, S., Spiess, R., Timms, N. E., Trimby, P., Wheeler, J., Zetterson, L. (1999) The application of electron backscatter diffraction and orientation contrast imaging in the SEM to textural problems in rocks. *American Mineralogist.* 1741-1759.

Prior, D. J., Wheeler, J. (1999) Feldspar fabrics in a greenschist facies albite-rich mylonite from electron backscatter diffraction. *Tectonophysics.* 303: 29-49.

Ramsay, J. G., Allison, I. (1979) Structural analysis of shear zones in an alpinised Hercyian granite. *Schweiz. Miner. Petrog. Mitt.* 59: 251-279.

Rutter, E. H. (1983) Pressure solution in nature, theory and experiment. *Journal Geol Soc London.* 140: 725-740.

Rutter, E. H., Casey, M., Burlini, L. (1994) Preferred crystallographic orienation development during the plastic and superplastic flow of calcite rocks. *J Struct Geol.* 16: 1431-1446.

Schmid, S. M. (1994) Textures of geological materials: computer model predictions versus empirical interpretations based on rock deformation experiments and field studies. In: Textures of geological materials. DGM Inofrmationsges, Oberursel, pp 279-301. As reported in Passchier & Trouw (2005) *Microtectonics.*

Schmidt, S. M., Fugenschuh, B., Kissling, E., Schuster, R. (2004) Tectonic map and overall architecture of the Alpine orogen. *Eclogae geol. Helv.* 97: 93-117.

Simpson, C. (1980) Oblique girdle orientation patterns of quartz C-axes from a shear zone in the basement core of the Maggia Nappe Ticini, Switerland. *J Struct Geol.* 2: 243-247.

Simpson, C. (1983) Strain and shape-fabric variations associated with ductile shear zones. *J Struct Geol.* 5: 61-72.

Skemer, P. (2005) Mindex. Unpublished program. Yale University.

Skemer, P., Katayama, I., Jiang, Z., Karato, S. (2005) The misorientation index: Development of a new method for calculating the strength of lattice-preferred orientation. *Tectonophysics.* 411: 157-167.

Stampfli, G. M., Borel, G. D., Marchant, R., Mosar, J. (2002) Western Alps geological constraints on western Tethyan reconstructions. *Jour. Of the Virtual Explorer.* 8: 77-106.

Steinmann, M.C. 1994: Die nordpenninischen Bündnerschiefer der Zentralalpen Graubündens: Tektonik, Stratigraphie und Beckenentwicklung. Ph.D Thesis, ETH, Zürich. *as reported in* Galli et al. 2007.

Stipp, M., Stunitz, H., Heilbronner, R., Schmid, S. M. (2002) The eastern Tonale fault zone: a "natural laboratory" for crystal plastic deformation of quartz over a termperature range from 250 to 700° C. *J Struct Geol.* 24: 1861-1884.

Tullis, J., Yund, R. A. (1982) Grain growth kinetics of quartz and calcite aggregates. *J of Geol.* 90: 301-318.

Tullis, J., Dell'Angelo, L., Yund, R. A. (1990) Ductile shear zones from brittle precursors in feldspathic rocks: the role of dynamic recrystallization. In : Hobbs, B. E., Heard, H. C. (eds) Mineral and rock deformation: laboratory studies. *AGU, Geophys Monogr.* 56:67-81.

Twiss, R. J., Moores, E. M. (1992) Structural geology. Freeman, New York. *as reported in* Passchier & Trouw 2005.

Wightman, R. H., Prior, D. J., Little, T. A. (2006) Quartz veins deformed by diffusion creep-accomodated grain boundary sliding during a transient, high strain-rate event in the Southern Alps, New Zealand. *J Struct Geol.* 28: 902-918.

APPENDIX A

Photomicrograph Catalog

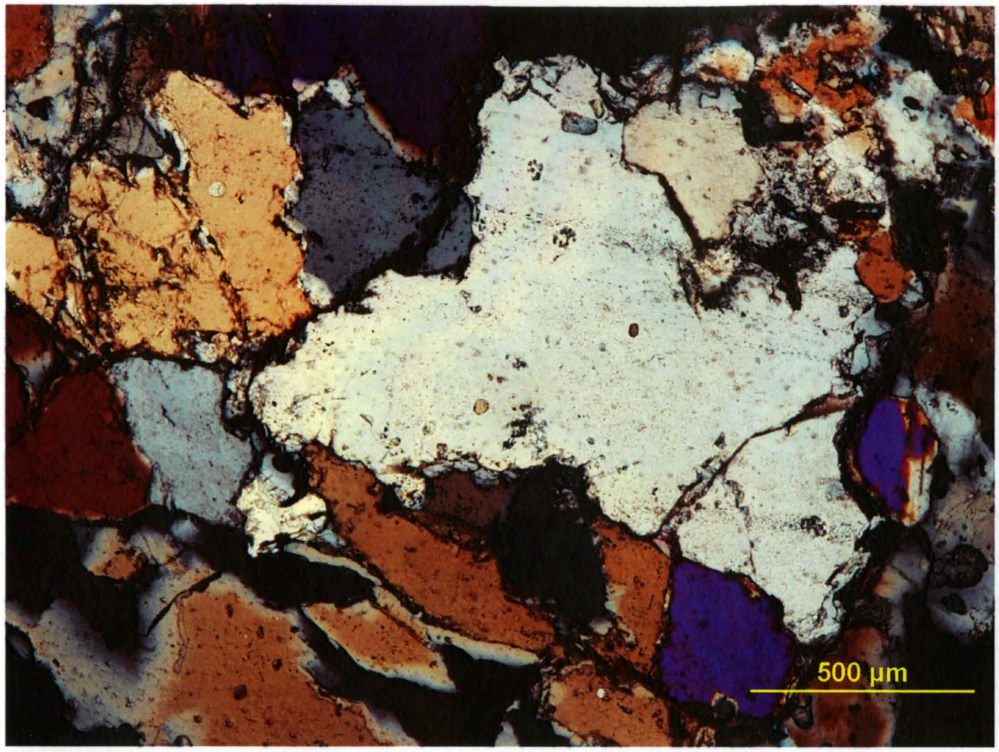

Figure 1: VCG aggregate. Sample 04-1 xa, 4x. Scale 500 µm.

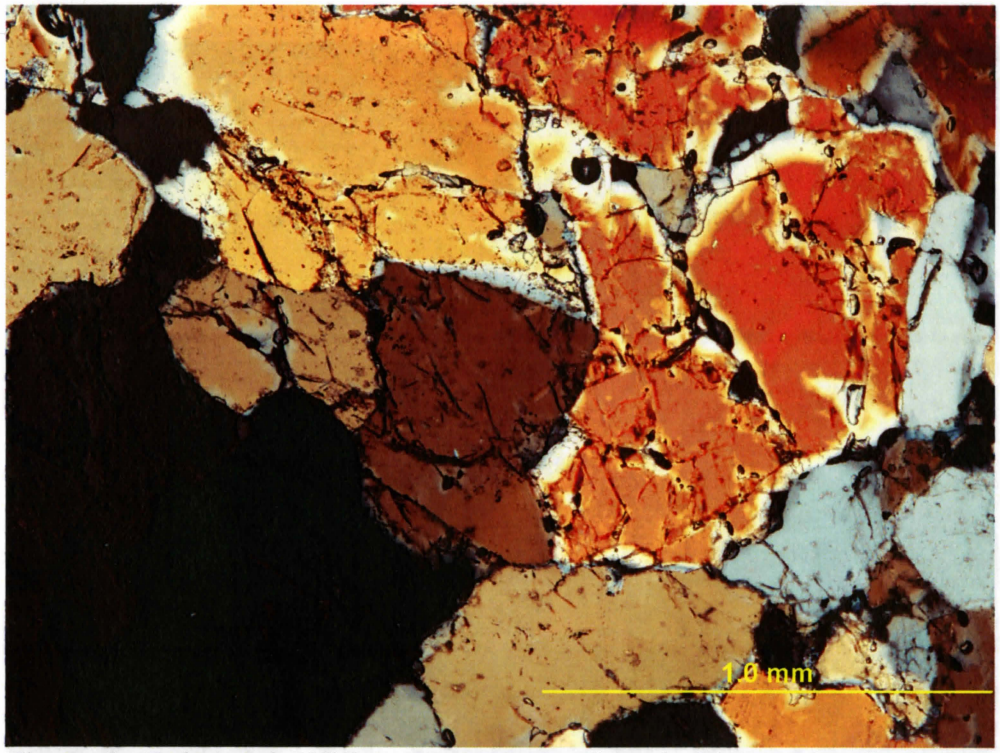

Figure 2: Polygonal, VCG quartz contacts. Sample 04-1 xa, 4x. Scale 1 mm.

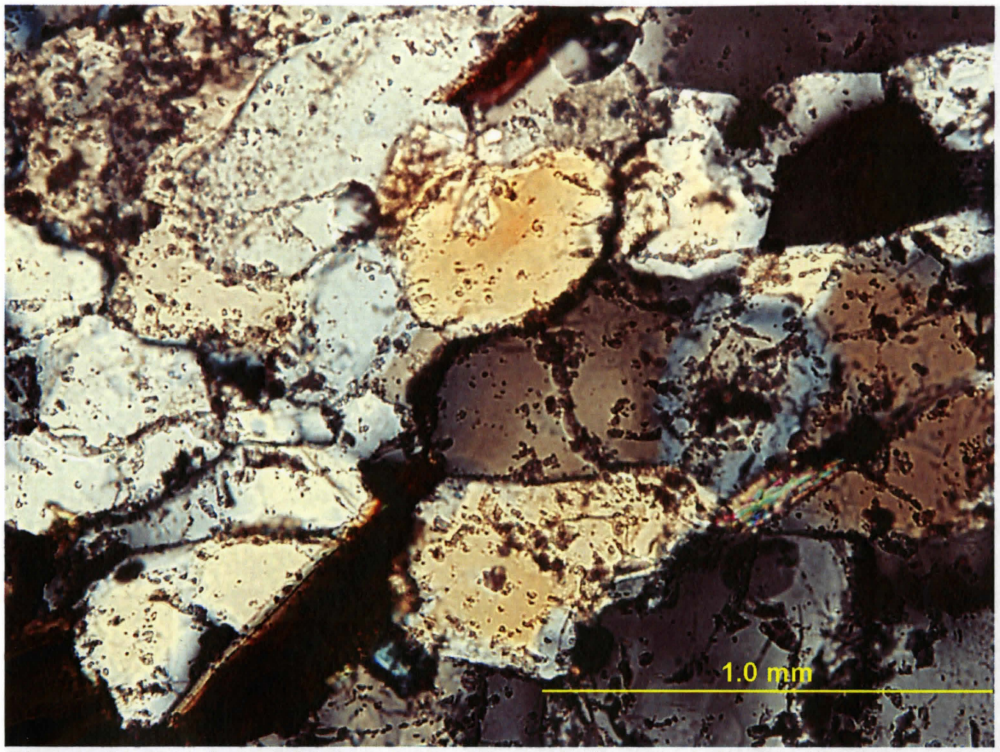

Figure 3: Bulging and lobate quartz boundaries. Sample 05-14 xz, 4x. Scale 1 mm.

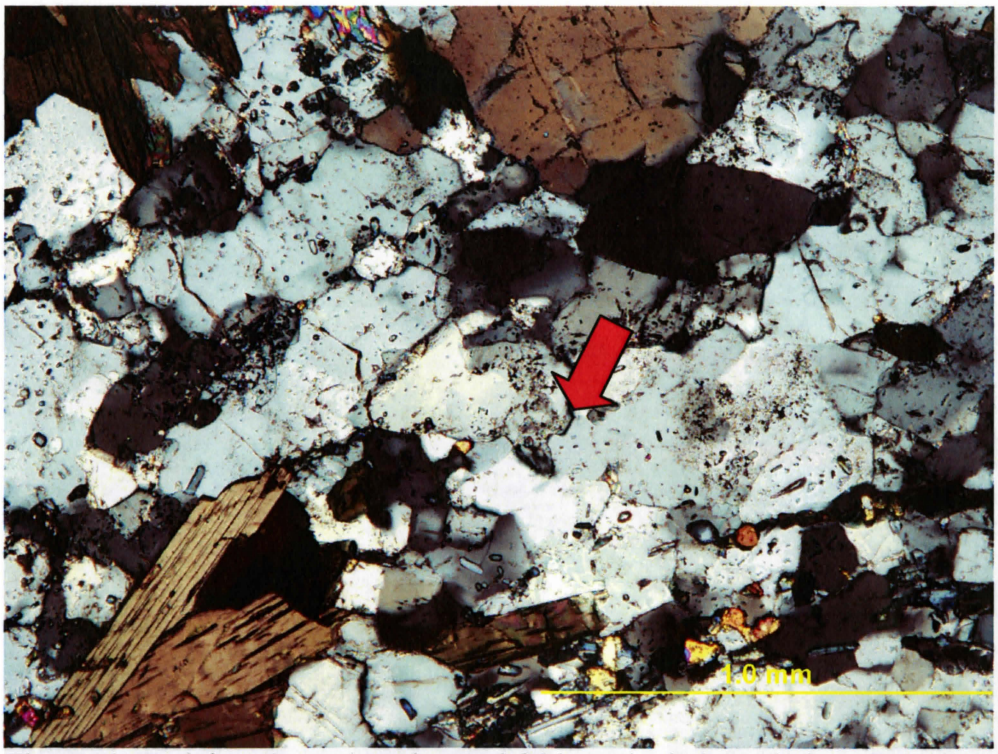

Figure 4: Bulging (arrow), polygonal feldspar grain boundaries. Sample 05-14xz, 4x. Scale 1 mm.

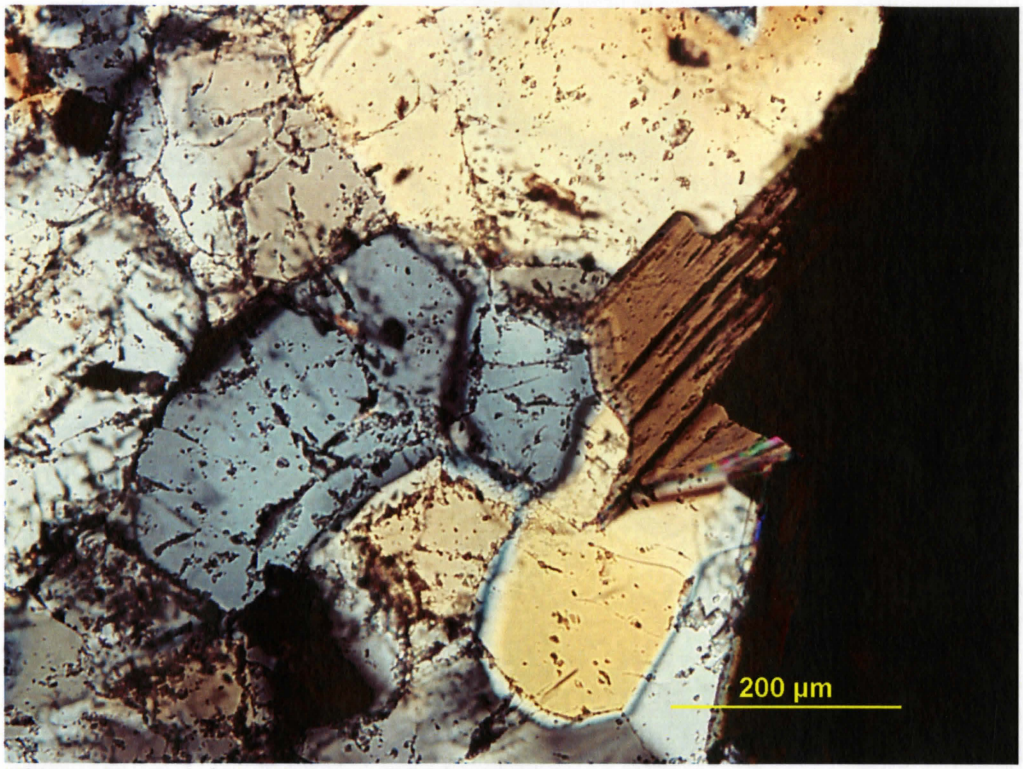

Figure 5: Bulging quartz and feldspar grain boundaries. Sample 05-14 xz, 10x. Scale 200 µm

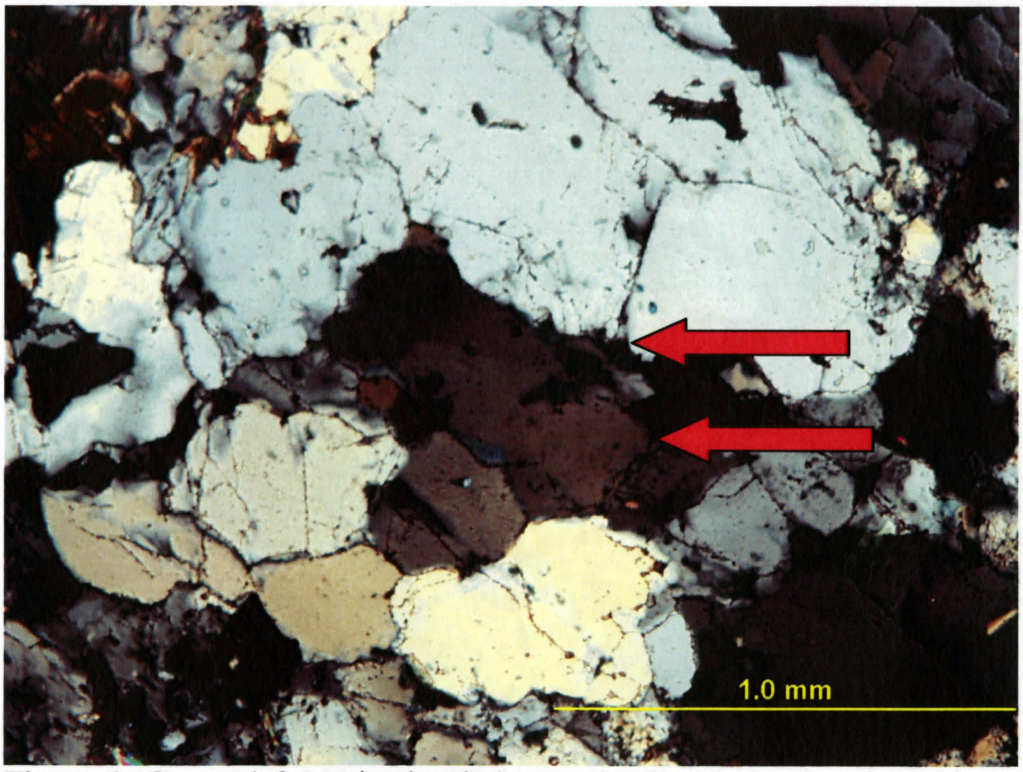

Figure 6: Quartz deformation bands (arrowed). Sample 04-1 xa, 4x. Scale 1 mm.

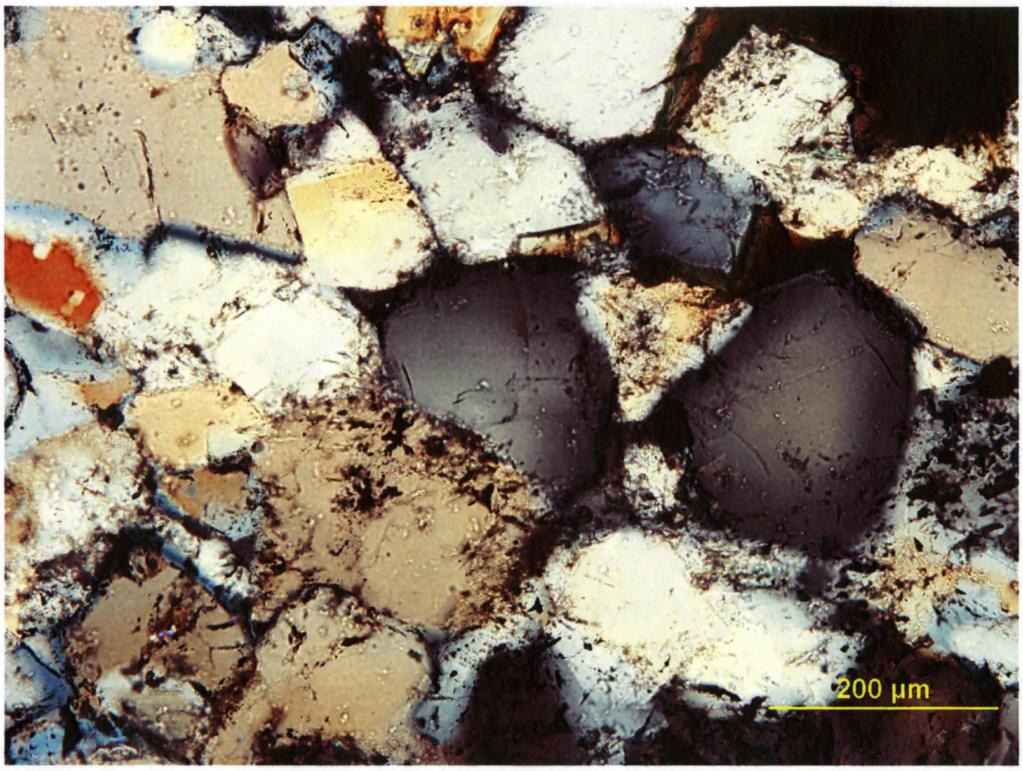

Figure 7: Undulatory extinction in feldspar grains. Sample 04-1 xa, 10x. Scale 200 µm.

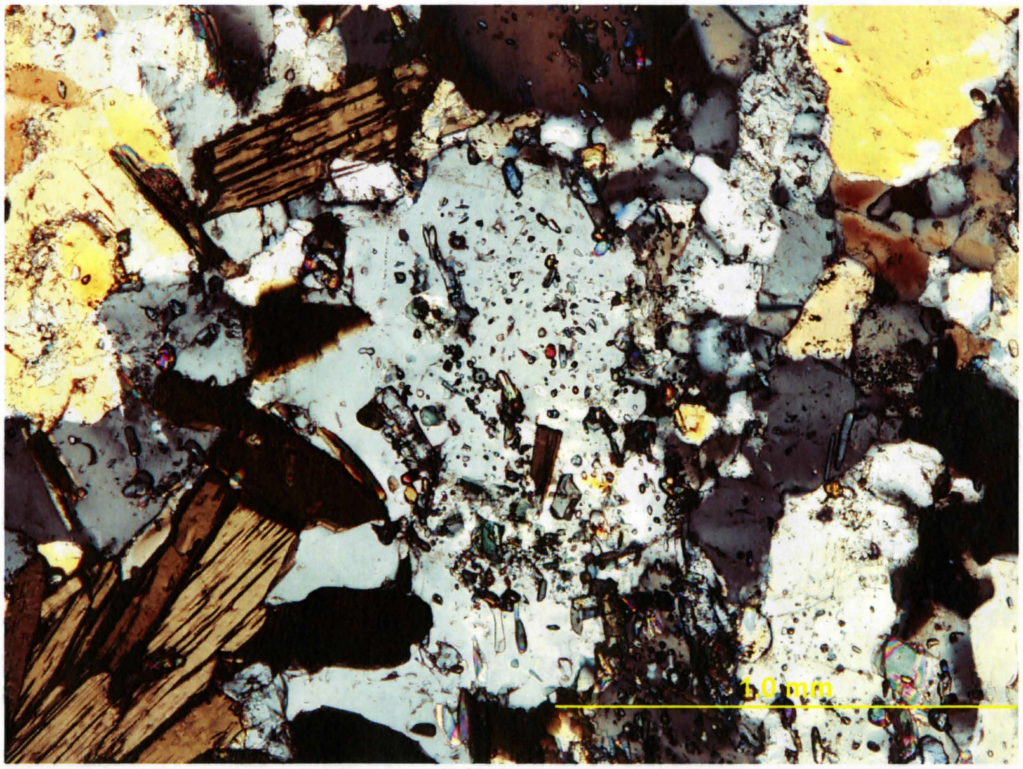

Figure 8: Unstrained feldspar poikiloblast. Sample 04-1 xa, 4x. Scale 1mm.

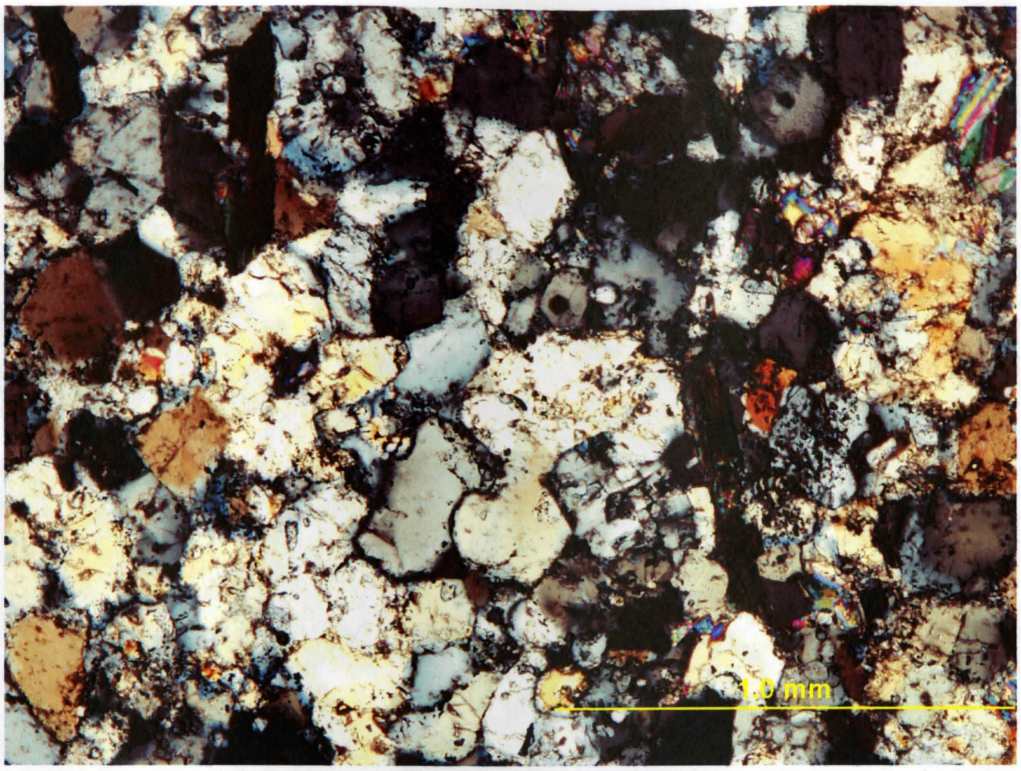

Figure 9: Coarse/Medium grain aggregate with bulging and lobate grain boundaries. Sample 04-1 xa, 4x. Scale 1 mm.

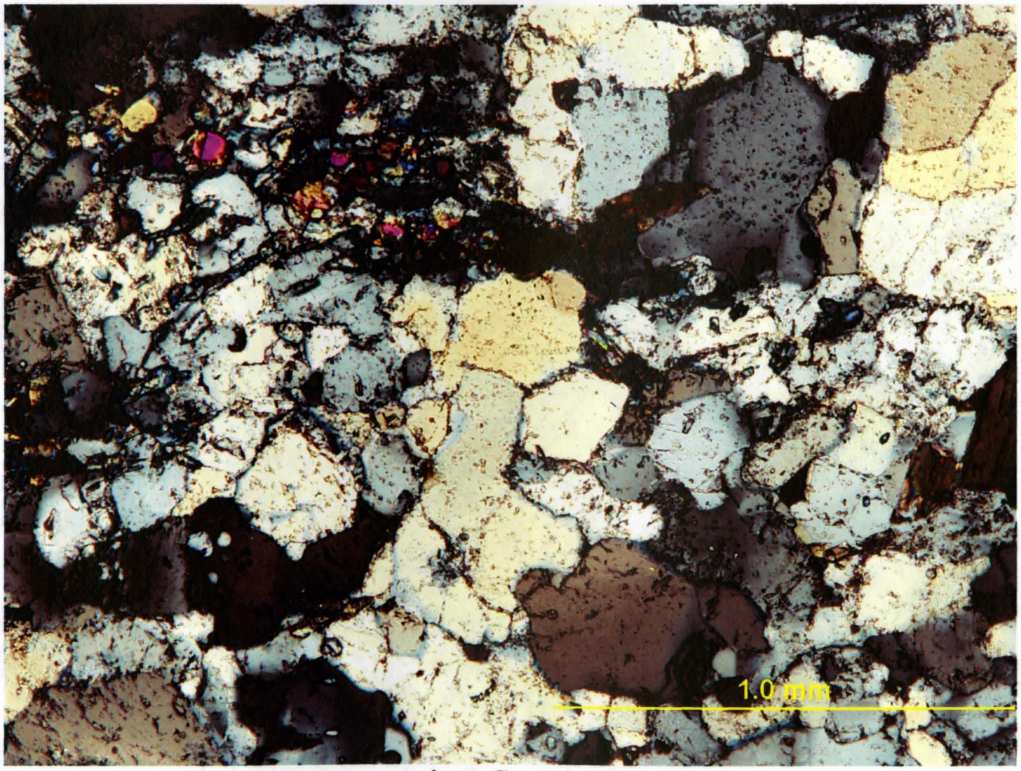

Figure 10: Polygonal quartz grains. Sample 05-14 xz, 4x. Scale 1 mm.

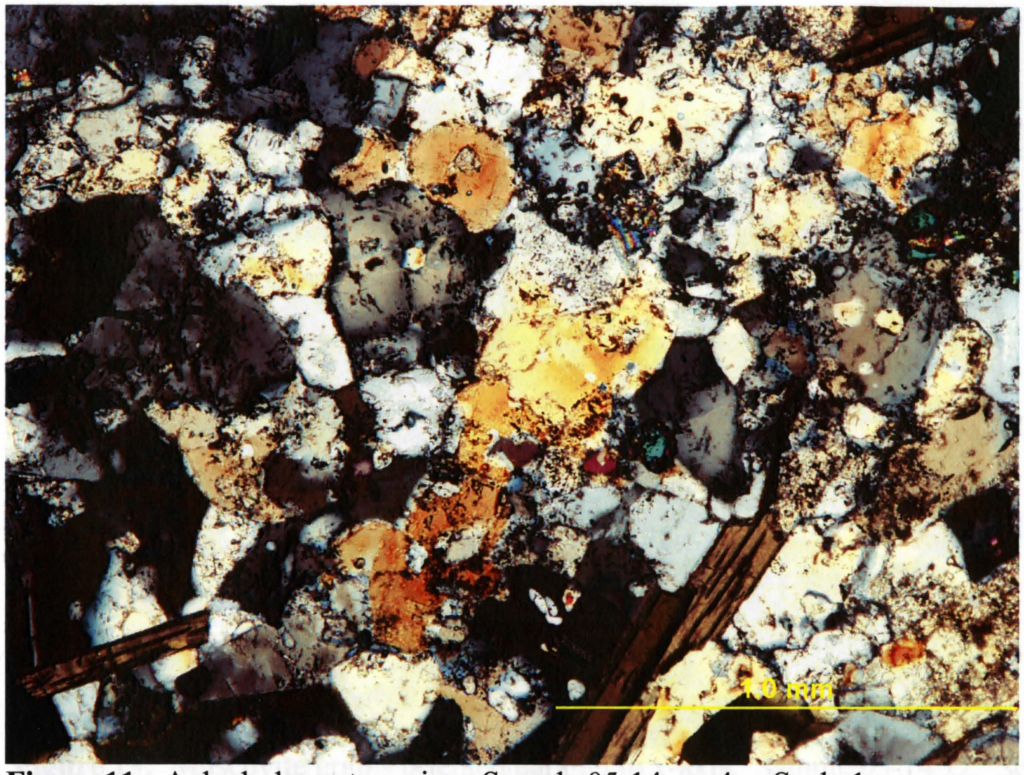

Figure 11: Anhedral quartz grains. Sample 05-14 xz, 4x. Scale 1 mm.

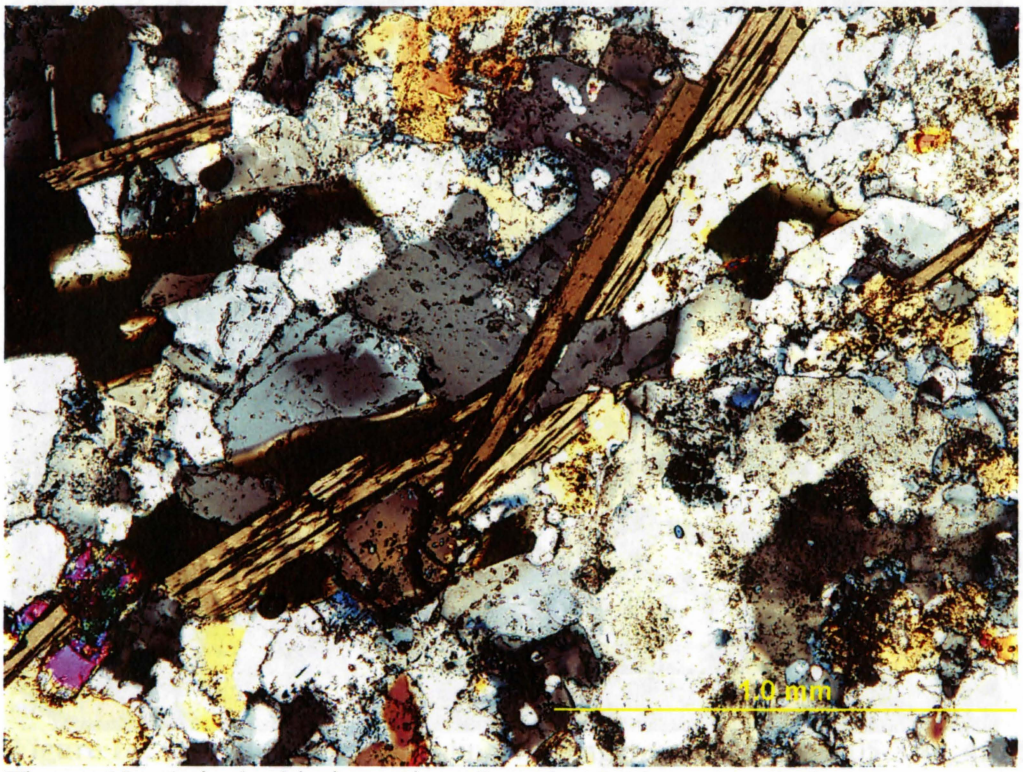

Figure 12: Acicular biotite grains. Sample 05-12 xz, 4x. Scale 1 mm.

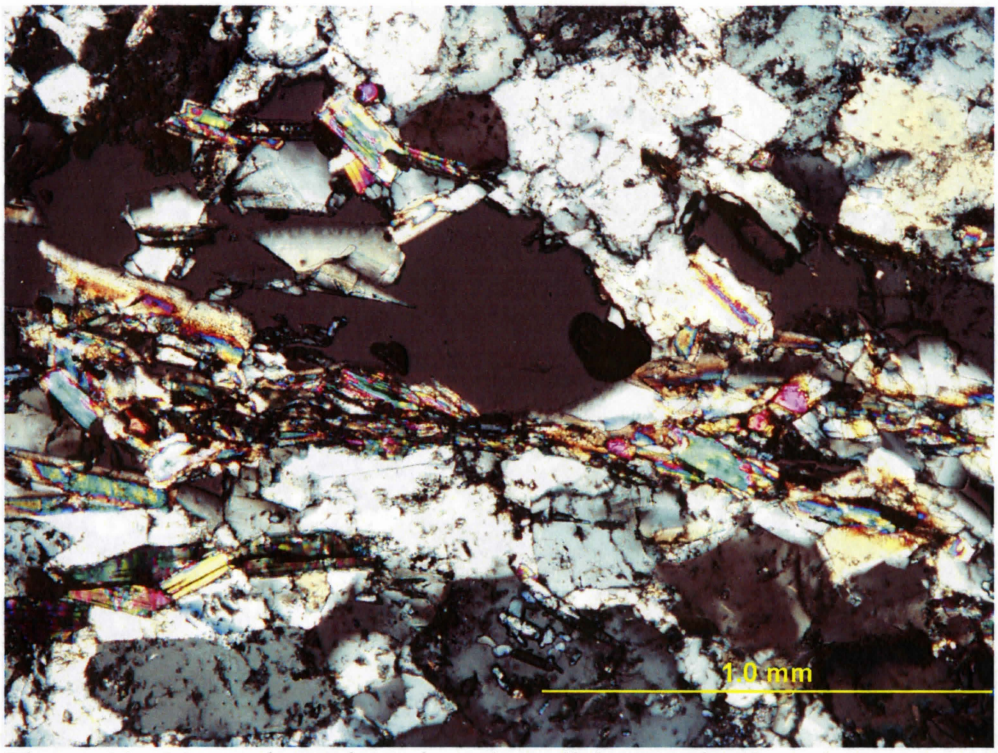

Figure 13: Muscovite grains oriented parallel to x-axis. Sample 05-14 xz. Scale 1 mm.

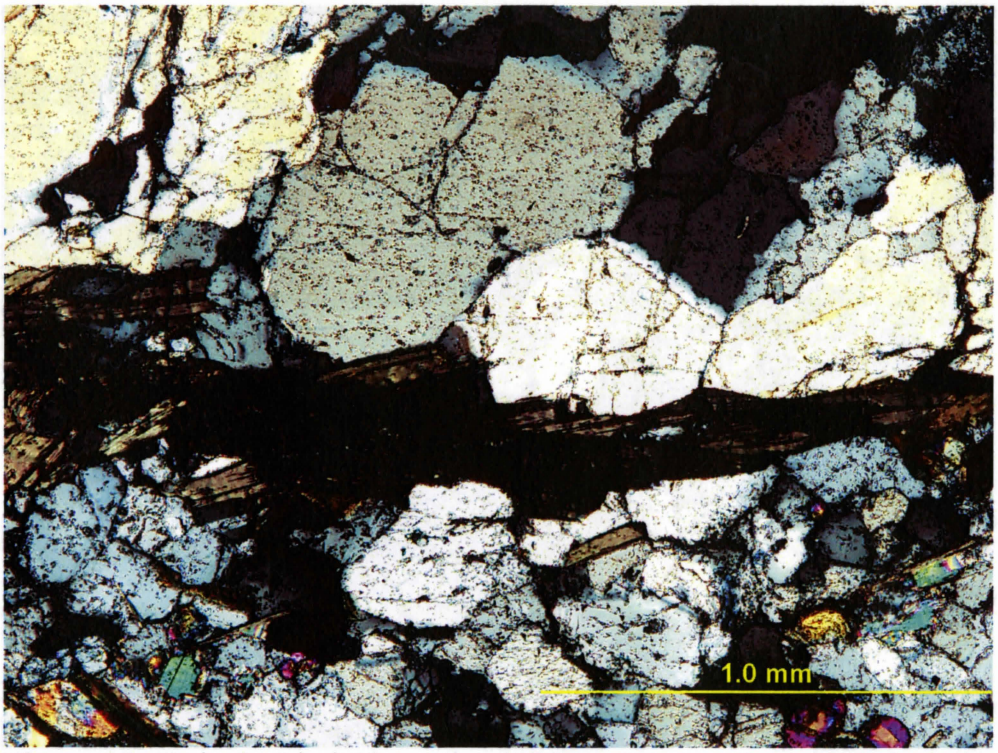

Figure 14: Acicular biotite bounding VCG aggregates. Sample 05-3 xz, 4x. Scale 1 mm.

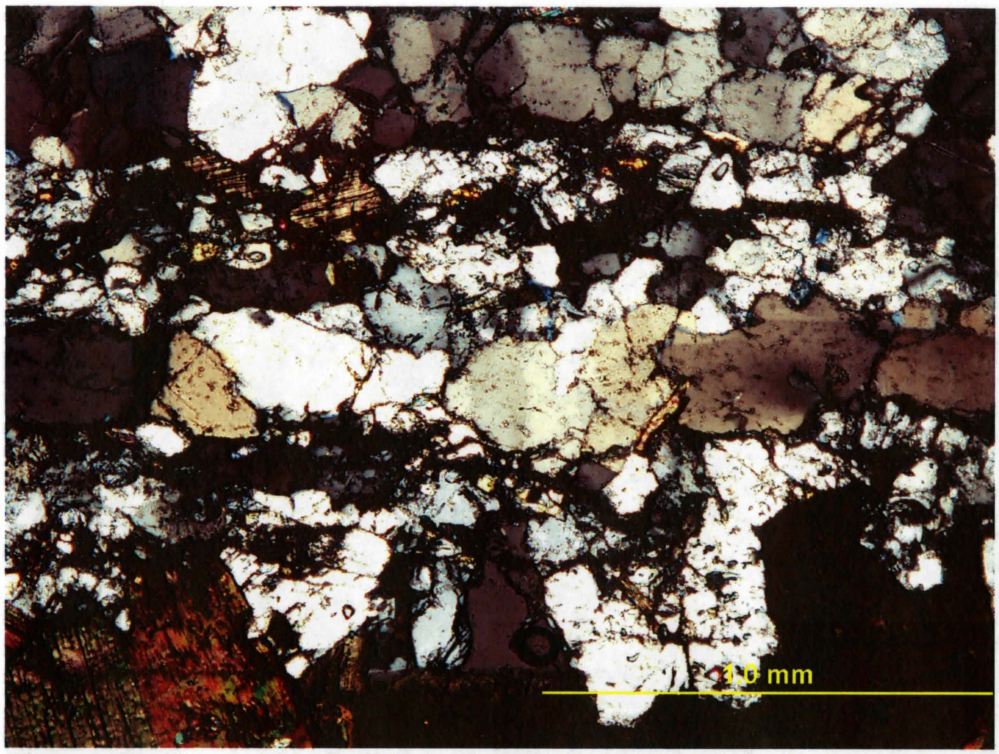

Figure 15: Narrow, VCG ribbon aligned parallel to x-axis. Sample 05-9 xz, 4x. Scale 1 mm.

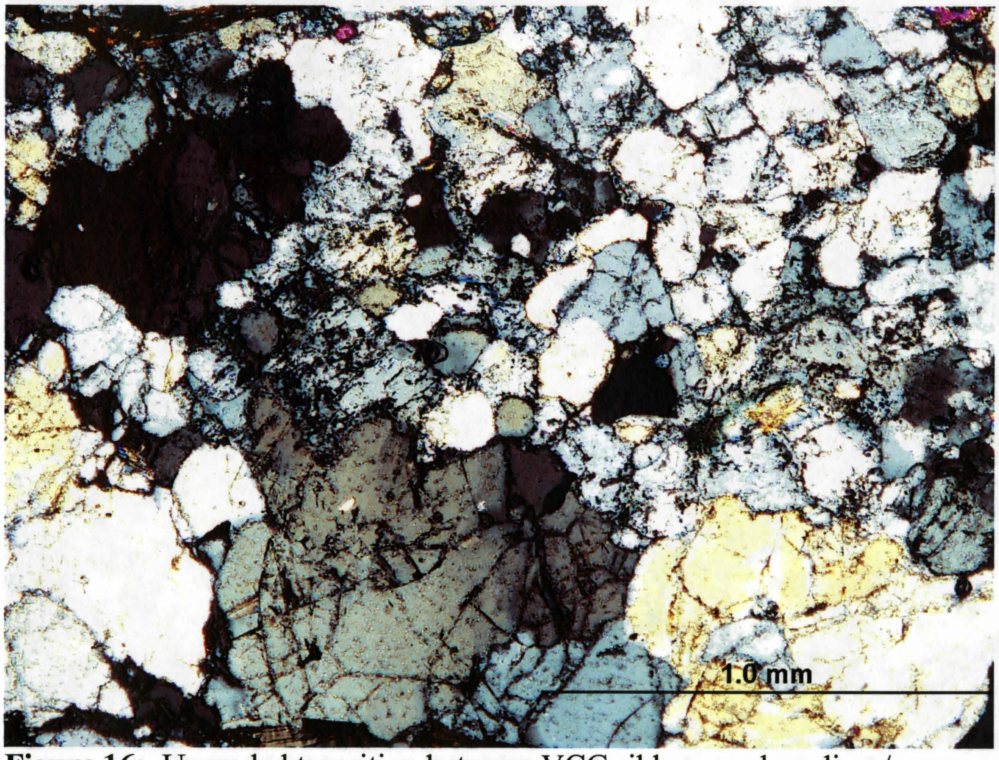

Figure 16: Ungraded transition between VCG ribbons and medium/coarse grain aggregates. Sample 05-5 xz. Scale 1 mm.

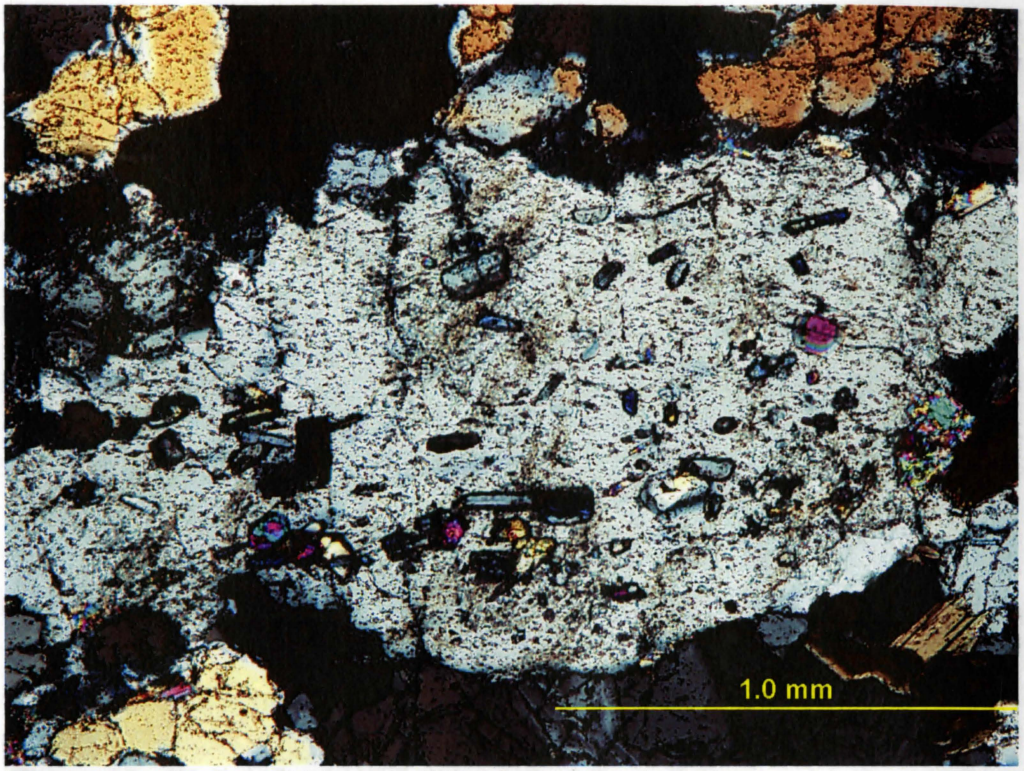

Figure 17: Strained feldspar poikiloblast with oriented muscovite inclusions. Sample 05-3 xz, 4x. Scale 1 mm.

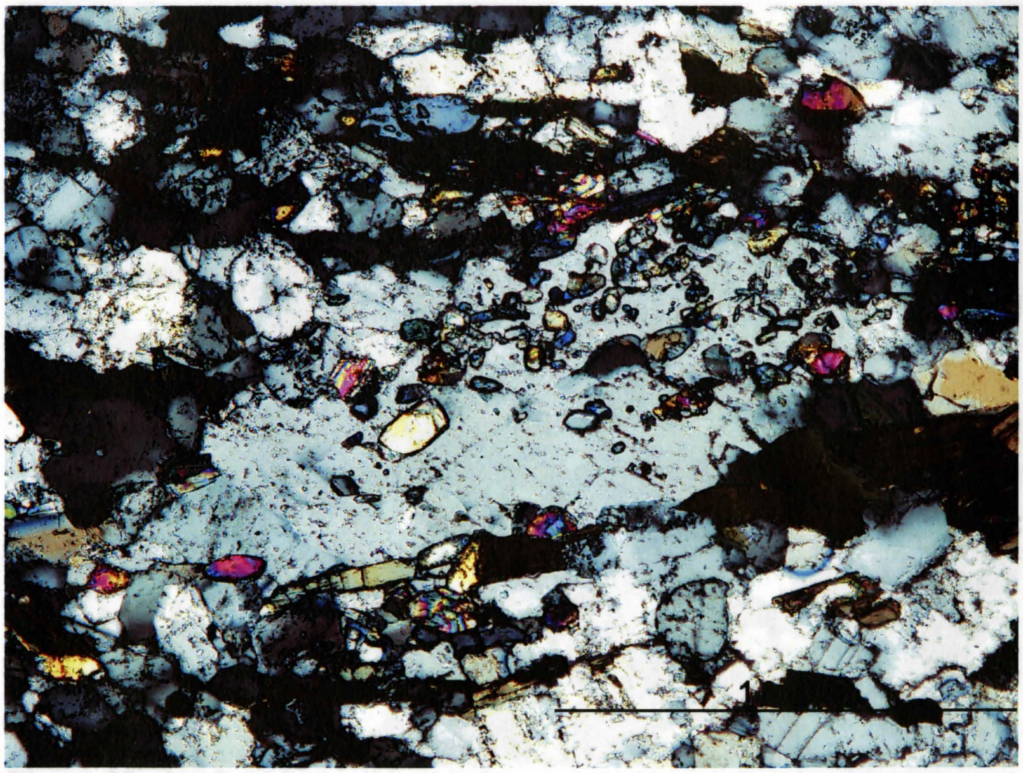

Figure 18: Strained feldspar poikiloblast with rounded, unoriented quartz and muscovite inclusions. Sample 05-3 xz, 4x. Scale 1 mm.

Figure 19: Well defined VCG ribbon aligned parallel to x-axis. Sample 05-9 xz, 4x. Scale 1 mm.

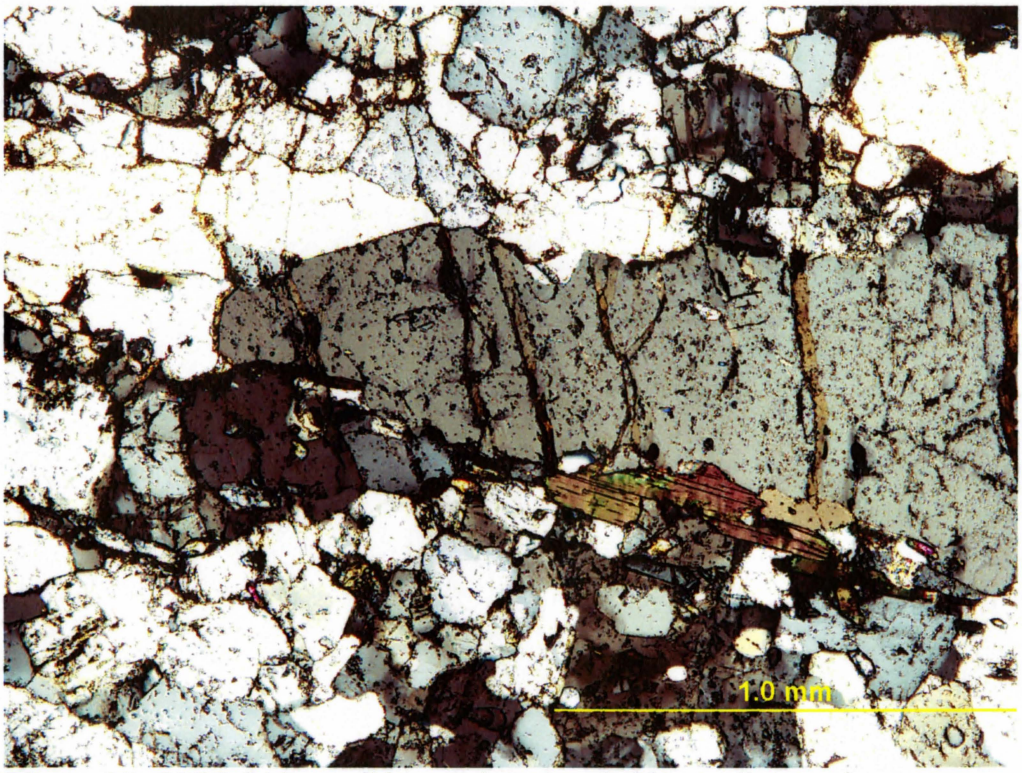

Figure 20: VCG feldspar ribbon end surrounded by medium grain aggregates. Sample 06-2 xz, 4x. Scale 1 mm.

Figure 21: Granoblastic medium grain texture.